Active Control of High Amplitude
Acoustic Waves in a Confined Geometry

by

Pai-Tsung (Paul) Huang

B.S.M.E., Rutgers University (1993)

Submitted to the Department of Mechanical Engineering in Partial
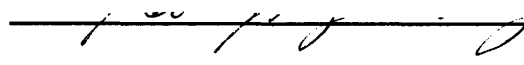Fulfillment of the Requirements for the Degree of

Masters of Science

at the
Massachusetts Institute of Technology
Cambridge, MA 02139, U.S.A.

February, 1996.

Author _____
Department of Mechanical Engineering
December 21, 1995

Certified by _____
John G. Brisson
Professor, Department of Mechanical Engineering
Thesis Supervisor

Accepted by _____
Ain A. Sonin
Chairman, Departmental Graduate Committee

Eng.

1

To my grandfather.

Active Control of High Amplitude Acoustic Waves in a Confined Geometry

by

Pai-Tsung (Paul) Huang

Abstract

An active control approach was developed to observe and control nonlinear distortions in high amplitude acoustic waves in a rigid-walled, two-radii harmonic resonator. The medium was air at ambient pressure and temperature. The resonator was first driven with a single-frequency waveform near the fundamental resonant frequency in generating standing waves with characteristic pressure amplitudes of 1400 Pa. The nonlinearly excited harmonics due to quadratic and cubic nonlinear coupling effects were then quenched by introducing additional driving frequencies. A semi-empirical computational model was developed using effective quadratic and cubic nonlinear coupling coefficients and an perturbation solution approach to predict the amplitudes of the first three pressure harmonics when the resonator is driven at the fundamental resonance. The active control approach allowed selective suppression and enhancement of specific mode(s) in the resonator while the effects on the other nonlinearly driven modes were observed. Both the model and experimental setup demonstrated that by quenching the first few nonlinearly excited harmonics, all subsequent higher harmonics were also quenched. The active control approach was also used to experimentally measure the quadratic and cubic nonlinear coupling coefficients, which were found to be fairly constant with the driving force.

Thesis Supervisor: Dr. John G. Brisson

Title: Professor of Mechanical Engineering

Acknowledgments

I would like to thank my thesis supervisor, John Brisson, for his enormous contributions to my education at MIT through his time and energy. Without his continuous support, encouragement, guidance, and patience, I would not have progressed this far. I would also like to acknowledge the support and friendship of my fellow colleagues in the mechanical engineering department, especially Ashok Patel, Steve Tang, and Hua Lang. I have thoroughly enjoyed the at times conflicting but always interesting conversations on school matters, personal aspirations, the type of food to buy at the food trucks that day, and which LSC movies were really worth seeing. The menu item 'General Gau Chicken' will be dearly missed, as will the free sneak previews.

I would like to acknowledge the support and confidence given by generous friends Chih-Hsin Tsai, Emily Luk, Carrollynn Chang, Yi-Chun Chao, and many others whose constant words of encouragement and advice helped me through some of the bumpier roads of life over the years. I would also like to thank my ESL teachers back in the first Reagan administration: Mrs. Zeldin, and Mrs. Kaminester. Without their daily lessons in the alphabet and the life that became of the letters, I would not be writing this today.

Last, but not least, I would like to express my most sincere gratitude to my family for their continuous support in my decisions on life. The sacrifices they have made will not be in vain.

Biographical Note

My parents, like many others, wanted a better life for my sister and I, so we left Formosa, or the beautiful island of Taiwan in 1982 to where else but New York. After thirteen years of being in the United States, I have adopted it as my permanent home. I attended Rutgers University from 1990 to 1993 where I received my bachelors of science in mechanical engineering with highest honors. For high school, I attended North Hunterdon Regional from 1986 to 1990. In the summer of 1989, I started my first of four internships with Exxon Research and Engineering Company in Clinton, New Jersey. The experiences at Exxon and MIT have taught me how to work alone and in groups. With an entrepreneurial frame of mind, I am now ready to tackle the world.

Table of Contents

List of Figures

7

9

List of Tables

Chapter 1 Introduction

R enewed interest in finite amplitude acoustic waves in confined geometries has been stimulated by recent developments in acoustic compressors and thermoacoustic refrigerators. These devices use resonant cavities to store energy in an acoustic standing wave. When the standing wave is driven to high amplitudes near the cavity's *fundamental* resonant frequency, the working fluid's acoustic nonlinearities couple energy from the driven mode to other (higher harmonic) modes which ultimately results in the formation of shock waves. Dissipation of energy by the shock waves diminishes the potential pressure amplitude obtainable within the cavity. Consequently, this curbs increases in power density within the cavity and limits the performance of the devices. Suppression of nonlinear effects is critical in improving directly the efficiency of the acoustic compressor, and less directly the efficiency of the thermoacoustic refrigerator.

Studies by Gaitan and Atchley[1], and Coppens and Sanders[2] have shown that nonlinear effects can be suppressed by the use of a detuned, or an *anharmonic*, cavity. An anharmonic cavity has resonant frequencies which are not integral multiples of the fundamental, a condition induced by the geometric design of the cavity. This *passive* control approach is currently used by both the acoustic compressors and thermoacoustic devices to suppress nonlinear distortion and to prevent shock wave formation. The approach has been shown to be effective, but it has its limits. For instance, the geometry design cannot be made too complicated (to avoid harmonic resonances) because

---

[1] D. F. Gaitan and A. A. Atchley, J. Acoust. Soc. Am. **93**, 2489-2495 (1993).

[2] A. B. Coppens and J. V. Sanders, J. Acoust. Soc. Am. **58**, 1133-1140 (1975).

turbulence losses will limit the attainable acoustic pressure amplitudes. Other problems with the passive approach are associated with the geometry design, which cannot be changed once a cavity is built.

Another possible approach for suppressing nonlinear effects is presented in this thesis. This new approach, which has received no attention in the past, is based on *actively* controlling the *magnitudes* of the nonlinearly generated harmonics. Instead of altering the geometry of a given cavity, this approach will modify the forcing function. The cavity will be driven at *multiple* frequencies to selectively drive a mode (or modes) and extract power from the other (unwanted) modes. This method actively "dissipates" certain modes which are necessary in initiating nonlinear effects. The active control approach can be used with the passive approach to further enhance the performance of the acoustic devices mentioned earlier. Furthermore, this approach allows for direct probing of the nonlinear acoustic coupling between the modes of a cavity. This thesis will document how an active control approach was successfully modeled and tested.

1.1 Finite Amplitude Acoustic Waves

Finite amplitude acoustic waves can be best described by first defining infinitesimal, or linear, acoustic waves. The characteristic shape of a dissipationless linear acoustic wave *does not* change as the wave travels through a medium. The amplitude of the wave may increase or decrease with distance and time, but the overall shape remains the same. The waves are of the form $Af(x \pm c_0 t)$, where A is the amplitude, f is the wave function shape (e.g. sine), x is the position, c_0 is a constant sound speed, and t is time. Such waves are solutions to the linear dissipationless wave equation which is derived using the linearized mass, momentum, and state equations.

A finite amplitude acoustic wave *does* change in shape as it propagates. The wave function f is no longer independent of A, x, and t. Finite amplitude waves are solutions to the nonlinear wave equation which is derived using higher-order approximations of the mass, momentum, and state equations. In 1808 Poisson developed an equation which showed that propagating sound waves will change in form and consequently generate additional frequencies.[3] Fay later showed that due to the nonlinear

---

[3] A. L. Thuras, R. T. Jenkins, and H.T. O'Neil, J. Acoust. Soc. Am. **6**, 173-180 (1935).

relation between pressure and specific volume there is found to be a gradual transfer of energy from components of lower frequency to those of higher frequency.[4]

The production of the second and higher harmonics as a wave progresses, due to the nonlinear character of the acoustic wave equation (leading to the formation of a shock in the inviscid case) is counterbalanced at the higher frequencies by sound absorption (dissipation).[5] When the two processes balance, an almost stable wave is the result. This thesis presents a method to control the wave in a confined geometry.

1.2 Finite Amplitude Acoustic Waves in Confined Geometries

When acoustic waves are confined to propagate in a rigid-walled cavity like a tube or a rectangular box, standing waves are set-up. Standing waves are formed by the phase interference between the incident and reflected waves at the cavity walls. If the wavelength of the waves is larger than the transverse (i.e. the radius of a tube) dimension(s) of the cavity, then the acoustic motion is essentially planar and the acoustic waves can be referred to as *plane standing waves*. Physically, standing waves maintain a pressure (or velocity) field such that it appears stationary in the sense that at any point x, the field simply fluctuates harmonically in time. In Fig. 1.1 the velocity field inside a rigidly closed tube oscillates with time but at a point x_0 where the velocity is zero, it will remain zero for all times.
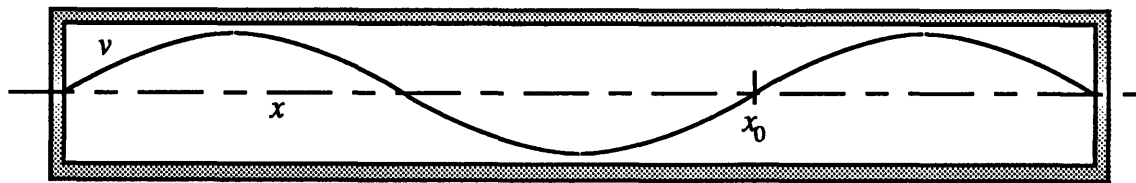
Figure 1.1 Velocity field (third mode) in a closed tube.

Nonlinear effects of finite amplitude standing waves in cavities have been studied by many researchers, most recently by Gaitan and Atchley of the Naval Postgraduate School. Their predecessors, Coppens and Sanders, conducted pioneering work in the 1960's and 1970's on solving the nonlinear wave equations and verifying the results experimentally. In 1968, Coppens and Sanders extended Keck-Beyer perturbation

---

[4] R. D. Fay, J. Acoust. Soc. Am. 3, 222-241 (1931).
[5] R. T. Beyer, *Nonlinear Acoustics*, 11 (1974).

solution approach and resulted in the ability to describe and predict amplitudes and phases of the nonlinearly generated harmonics.[6] They showed that finite amplitude effects are enhanced when the forcing frequencies are nearly equal to the characteristic mode frequencies of a cavity. To demonstrate, they used straight tubes with *harmonic* characteristic modes which allowed for efficient coupling of energy between the fundamental and the nonlinearly generated harmonics. Gaitan and Atchley then focused on *anharmonic* (where the characteristic modes are *not* harmonics of the fundamental) tubes and succeeded in suppressing nonlinear effects. For this reason, most current applications of finite amplitude standing waves utilize anharmonic cavities to avoid nonlinear losses.

1.3 Practical Applications of Finite Amplitude Acoustic waves

Two important applications of finite amplitude acoustic waves have emerged as a result of recent environmental concerns and technical advances. The ban on the use of chlorofluorocarbons (CFCs) as refrigerants has prompted research into alternative refrigerants and improved or novel refrigeration techniques. In just the past few years, major projects by research and corporate institutions have shown that thermoacoustic refrigerators may be practical alternatives to conventional refrigerators.[7] Current refrigerators and air conditioners remove heat to an evaporating liquid, the refrigerant. This process bases the heat transfer on phase changes of the refrigerant as it circulates through the refrigeration unit. A major constraint, therefore, in designing conventional refrigerators, is the type of refrigerant used. Thermoacoustic refrigerators do not use CFCs nor the newer hydrofluorcarbons (HFCs) as refrigerants. In fact, the heat transfer mechanism is not based on any refrigerant, but rather on the unusual relationship between temperature and sound.[8]

"[In a thermoacoustic refrigerator], to capture coldness, a plastic coil is placed inside a thermoacoustic device's tube so that gases pass freely through the coil as they are pushed from one end of the unit to the other by a high-intensity sound wave. The gases warm up as they move toward the high-pressure portion of the wave, transferring heat to one side of the coil, and cool off as they oscillate back toward the low-pressure region,

---

[6] A. B. Coppens and J. V. Sanders, J. Acoust. Soc. Am. **43**, 516-529 (1968).
[7] G. Swift, Physics Today **48**(7), 22-28 (1995).
[8] S. Garfinkel, Technology Review, October 18, 17-19 (1994).

transferring cold to the other side. Coolness is then conducted to the desired location."[9] In Fig. 1.2, the comparison between the conventional and the thermoacoustic refrigeration cycle shows the latter to be much simpler in design. The low number of components and moving parts contribute to higher reliability and lower cost.
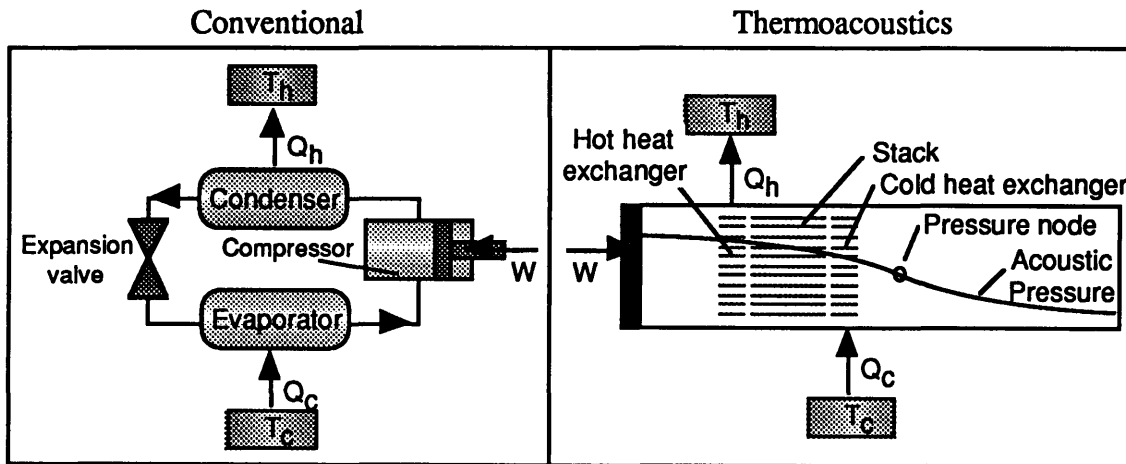
Figure 1.2 Conventional and thermoacoustic heat transfer process.

Several factors now exist that limit the efficiency of thermoacoustic refrigerators, from inherent losses (heat transfer to and from the gas across the stack) to viscous losses incurred as the gas oscillates in the cavity. To improve the efficiency, higher power densities are needed, thus the need to increase the acoustic pressure amplitudes. However, increasing the pressure amplitudes to large magnitudes means generating nonlinear effects that eventually result in shock formation and significant losses. As mentioned, the current approach to suppress the nonlinear effects is to use an anharmonic cavity, this thesis shall present another approach, based on a harmonic cavity.

Another device that has benefited from using an anharmonic cavity is the sonic compressor. In this compressor, a standing wave is driven to high pressure amplitudes which compresses the refrigerant (Fig. 1.3). The refrigerant moves in and out of the cavity through check valves mounted on the end of the cavity. In conventional compressors, pistons and rotors are used to compress the refrigerant. To help maintain smooth motion, lubricants (oils) must be added to the refrigerants. A problem with using the new refrigerants is that compatible lubricants have not yet been developed

---

[9] Ibid.

successfully.[10] Sonic compressors require no lubrication and is ideal for high purity gas compression.   Furthermore, one company working on sonic compressors projects improvements in energy efficiency of 30 to 40 percent over existing compressors.[11]
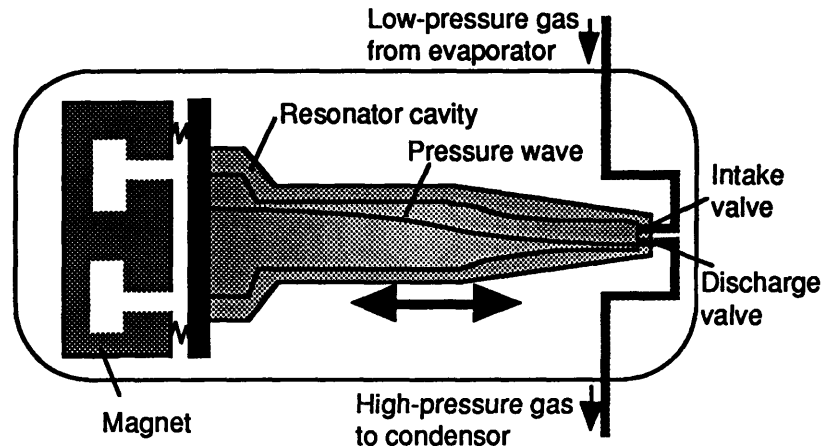
Figure 1.3 Sonic compressor.

The pressure amplitudes in sonic compressors are large and without altering a cavity to an anharmonic design, shock waves are formed, wasting power and limiting compression. Although the anharmonic design is effective in suppressing nonlinear effects, it may be improved further with the active approach.

1.4 Active Control Of Finite Amplitude Acoustic Waves

A cavity driven at its fundamental resonance will result in the generation of higher harmonics. The active approach proposes to suppress these higher harmonics by introducing *additional* forcing tones with appropriate amplitudes and phases. In Fig. 1.4, a harmonic cavity is driven at one end by a piston at the fundamental resonant frequency (of the cavity), $F_{dr} = F_1 \sin(\omega_{dr} t)$. The pressure waveform $p(t)$ is recorded by a pressure gauge at the fixed-end of the cavity. If only one harmonic, the second, is generated through nonlinear effects, then the total pressure has two terms as shown. To suppress the second harmonic, $p_{2L} \sin(2\omega_{dr} t + \theta_2)$, a second forcing tone, $F_2 \sin(2\omega_{dr} t + \phi_2)$, is imposed so that the response to this tone is equal in amplitude to p_2, but out of phase by 180° (Fig. 1.5). F_2 and ϕ_2 are determined by filtering the pressure response for the

---

[10] P. Yam, Scientific American, November, 120-121 (1992).
[11] Ibid.

second harmonic component.

$$p_L(t) = p_{1L}\sin(\omega_{dr}t + \theta_1) + p_{2L}\sin(2\omega_{dr}t + \theta_2)$$
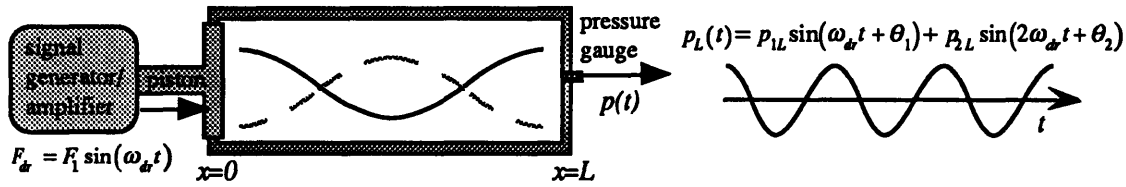
Figure 1.4 Pressure response to single-tone drive at the fundamental resonance.
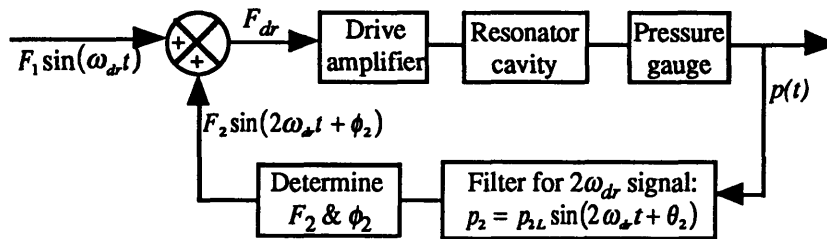
Figure 1.5 Active control loop to eliminate the second harmonic.

An assumption used in this approach is that the responses to individual driving tones can be superimposed for the total response. In the loop considered above, two forcing functions are assumed to generate two separate sets of responses: $F_1\sin(\omega_{dr}t)$ generates a ω_{dr} and a $2\omega_{dr}$ term (nonlinear effect), $F_2\sin(2\omega_{dr}t + \phi_2)$ generates a $2\omega_{dr}$ term. When the three terms are summed, the two $2\omega_{dr}$ terms cancel and only the ω_{dr} term remain (Table 1.1).

Forcing term	*Response*
$F_1\sin(\omega_{dr}t)$	$p_{1L}\sin(\omega_{dr}t + \theta_1) + p_{2L}\sin(2\omega_{dr}t + \theta_2)$
$F_2\sin(2\omega_{dr}t + \phi_2)$	$-p_{2L}\sin(2\omega_{dr}t + \theta_2)$
Total	$p_{1L}\sin(\omega_{dr}t + \theta_1)$

Table 1.1 Superposition of individual responses.

In reality, nonlinear effects generate *all* harmonics of the fundamental, not just the second. Furthermore, the nonlinear nature of the responses precludes the use of superposition principles. Nonetheless, as this thesis will show, some assumptions such as superposition of responses and the generation of a *finite* number of harmonics can be successfully used to demonstrate the approach's effectiveness.

1.5 Contributions of this thesis

This thesis makes three significant contributions to the study of finite amplitude acoustic waves in confined geometries. The first is proof of principle of the active approach in suppressing nonlinear effects. An active feedback system was designed and developed that allowed selective driving or damping of the modes within a resonator cavity. This approach presents a new tool which can be used to suppress nonlinear effect losses in high amplitude acoustic waves.

The second contribution is the ability to experimentally probe for the nonlinear coupling between the modes of the cavity. In relation to this, the active approach also allows direct measurement of the second and higher-order nonlinear coupling terms between the modes of the cavity. The term *order* used here refers to the order of the nonlinear wave equation. Although most of the thesis discusses the response of the second-order (quadratic) nonlinear wave equation, third order (cubic) coupling effects are also discussed. Knowing how the modes couple and how much coupling is present will be useful in understanding how energy is transferred and how it can be stopped from "leaking" to higher harmonics.

The third contribution is the development of a simple computational model that calculates the resonator response using a perturbation solution approach. Theoretical development of the perturbation solutions show that the nonlinearly generated harmonics originate from the fundamental mode. For example, in the quadratic coupling case, a forcing drive at frequency ω_{dr} will result in a dominant response at frequency ω_{dr} but also will generate a second harmonic at frequency $2\omega_{dr}$. Higher frequency modes are then excited by the interaction of these two terms. The model is limited to just the first few harmonics. The simple model rapidly calculates the response due to a given driving function, and predicts numerical values for the drive variables F_2 and ϕ_2 needed to suppress the harmonic response of the cavity.

1.6 Thesis organization

This thesis is divided into five major sections beginning with Chapter 1, the Introduction. Chapter 2 presents a more in-depth discussion of nonlinear acoustic waves in confined geometries. The quadratic nonlinear wave equation (QNE) used by Coppens

and others will be stated and its solutions briefly discussed. Another quadratic nonlinear equation will then be introduced which uses an *effective quadratic nonlinear coupling coefficient* ε_{quad}. This effective quadratic nonlinear wave equation (EQNE), is the basis for the theoretical and computational models in this thesis. A perturbation solution is presented that clearly shows how harmonic modes are excited in the second-order EQNE. The perturbation solution approach is then extended using an effective cubic (third-order) nonlinear equation (ECNE) that includes both quadratic and cubic nonlinear effects.

The active control approach is discussed in Chapter 3. The three sections to this chapter are: the basic concept - multiple frequency input forcing function, the concept applied to a specific resonator design, and the experimental setup. Although the active approach is applicable to both harmonic and anharmonic cavities, this chapter will discuss why a harmonic cavity was chosen and how it was designed.

Chapter 4 presents the experimental and computational results. The results are presented in two sections: responses to a single-tone drive, and response to a multi-tone drive. The main purpose of the first section is to confirm the validity of the computational model in predicting amplitudes of the harmonic responses. The second section then applies the active control approach in suppressing nonlinear effects and probing nonlinear coupling coefficients. An interesting application of the active control approach will also be presented: acoustic mixing.

Chapter 5 presents a summary of the thesis and suggestions for future work.

Chapter 2 Nonlinear Acoustic Waves in Confined Geometries

I n order to employ an active control approach on suppressing nonlinear effects in acoustic waves within confined geometries, the nonlinear effects must first be understood, the most crucial aspect of which is how the first few harmonics are generated. Once the mechanism for the generation of harmonics is understood, a technique to suppress these harmonics can then be devised. This chapter will focus on the generation of harmonic modes via a theoretical model using *effective nonlinear coupling coefficients*. Before this model is presented, results from past research efforts will be discussed. As the discussion will show, many assumptions and approximations used previously are still applicable to current research and will thus be retained to simplify the theory.

2.1 Classical quadratic nonlinear wave equation, QNE

For their acoustic work in confined geometries, Coppens and Sanders[1] used a nonlinear equation of the form:

$$\left(c_0^2 \nabla^2 - \frac{\partial^2}{\partial t^2} + \frac{\partial}{\partial t} \Im \right) \frac{p}{\rho_0 c_0^2} = -\frac{\partial^2}{\partial t^2} \left[\left(\frac{u}{c_0} \right)^2 + \frac{\gamma - 1}{2} \left(\frac{p}{\rho_0 c_0^2} \right)^2 \right],$$ (2.1)

where u and p are the total acoustic velocity and pressure, ρ_0 and c_0 are the gas density and sound speed at ambient conditions, γ is the ratio of specific heats for the gas, and $\Im$ is a

---

[1] A. B. Coppens and J. V. Sanders, J. Acoust. Soc. Am. 58, 1133-1140 (1975).

linear operator that leads to dissipation and dispersion. The left-hand side of the equation is the classical, linear wave equation with dissipation. The right-hand side is the effective forcing function leading to harmonic generation. Although the focus of this chapter is not to re-derive Eq. 2.1, the underlying assumptions and developmental processes will be discussed. The reader is referred to works by Coppens and Sanders[1,2] for a full discussion on the derivations.

The nonlinear wave equation is arrived at with the same procedure as that for the linear wave equation, the difference being the order of the terms retained. In the linear case, for example, the continuity equation, an essential piece in deriving the wave equation, only hold the first-order acoustic quantities (i.e. pressure and density). In the nonlinear case, all higher terms of the continuity equation are carried through until the end when a set of approximations and assumptions is imposed. One assumption is that the peak Mach number of the driven fundamental acoustic wave must be small, $M \ll 1$, where $M = U_0/c_0$, U_0 is the maximum particle velocity and c_0 is the sound speed. Another assumption is that the dissipative process is weak, $\alpha/k \ll 1$, where α is the infinitesimal-amplitude attenuation constant, and k is the wave number.

Next, the dominate source of dissipation is assumed to arise from the viscosity of the fluid at the tube walls and the thermal conductivity of the walls. This assumption must be met with the condition[3] that the thickness of the boundary layer be smaller than the wavelength of the highest acoustic frequency of interest. The boundary layer thickness is approximated[4] by $l \approx 5(v/\omega)^{\frac{1}{2}}$, where v is the kinematic shear viscosity of the fluid and ω the (angular) frequency. Finally, to use Eq. 2.1 for *plane* standing waves in tubes, several important restrictions must be imposed. Geometrically, the length of the tube must be much greater than the radial dimension. In relation to this, there must be no excitation of any transverse mode of the system, so that the amplitude of the wavefront is essentially constant outside the boundary layer[3].

With the assumptions listed above, Eq. 2.1 is then derived using the constitutive equations (continuity, force equations, etc.), neglecting terms of orders higher than M^2, $M(\alpha/k)$, and $(\alpha/k)^2$. Now, if the perturbation solution approach is used, harmonic

[2] A. B. Coppens and J. V. Sanders, J. Acoust. Soc. Am. 43, 516-529 (1968).
[3] A. B. Coppens, J. Acoust. Soc. Am. 49(1), 306-318 (1971).
[4] E.E. Weston, Proc. Phys. Soc. (London) B66, 695-709 (1953).

generation can be easily demonstrated. First, the pressure p and velocity u are written as perturbation series:

$$p = p^{(1)} + p^{(2)} + p^{(3)} + p^{(4)} + ... \tag{2.2a}$$

and

$$u = u^{(1)} + u^{(2)} + u^{(3)} + u^{(4)} + ..., \tag{2.2b}$$

where the superscripted numbers denote the *orders* of the perturbation terms. Now, by applying an externally imposed forcing term F_{dr}, Eq. 2.1 becomes the following:

$$\left(c_0^2 \nabla^2 - \frac{\partial^2}{\partial t^2} + \frac{\partial}{\partial t}\Im \right) \frac{p}{\rho_0 c_0^2} = -F_{dr} - \frac{\partial^2}{\partial t^2}\left[\left(\frac{u}{c_0}\right)^2 + \frac{\gamma-1}{2}\left(\frac{p}{\rho_0 c_0^2}\right)^2 \right]. \tag{2.3}$$

Substituting second-order perturbation solution terms $p = p^{(1)} + p^{(2)}$ and $u = u^{(1)} + u^{(2)}$ into Eq. 2.3 and equating terms of equal order up to second order, results in two equations, Eq. 2.4a and 2.4b. In the forcing function for Eq. 2.4b, terms of order $p^{(1)}p^{(2)}$, $\left(p^{(2)}\right)^2$, $u^{(1)}u^{(2)}$, and $\left(u^{(2)}\right)^2$ have been neglected on the ground that $\left(p^{(1)}\right)^2$ and $\left(u^{(1)}\right)^2$ are much larger.

$$\left(c_0^2 \nabla^2 - \frac{\partial^2}{\partial t^2} + \frac{\partial}{\partial t}\Im \right) \frac{p^{(1)}}{\rho_0 c_0^2} = -F_{dr}, \tag{2.4a}$$

$$\left(c_0^2 \nabla^2 - \frac{\partial^2}{\partial t^2} + \frac{\partial}{\partial t}\Im \right) \frac{p^{(2)}}{\rho_0 c_0^2} = -\frac{\partial^2}{\partial t^2}\left[\left(\frac{u^{(1)}}{c_0}\right)^2 + \frac{\gamma-1}{2}\left(\frac{p^{(1)}}{\rho_0 c_0^2}\right)^2 \right]. \tag{2.4b}$$

Eq. 2.4b shows that the second-order perturbation term $p^{(2)}$ is the result of nonlinear self interactions of the first-order solution. If the number of perturbation terms is increased, then the higher-order solutions are dependent on the interaction of both classical and other nonlinearly generated terms. For example, if p is composed of three terms $p = p^{(1)} + p^{(2)} + p^{(3)}$, then $p^{(2)}$ depends on self-interactions of $p^{(1)}$, and $p^{(3)}$ depends on interactions between $p^{(1)}$ and $p^{(2)}$. Thus, if the acoustic waves are driven at a frequency ω_{dr}, then from the perturbation solution approach, the effective forcing function in Eq. 2.1 will generate all integer multiples $n\omega_{dr}$ of the driving frequency and the full solution must contain *all* harmonics of the input frequency[1]. In Eq. 2.4, if $p^{(1)}$ is sinusoidal in time, say $p^{(1)} = A\sin(\omega_{dr}t)$, where A is a spatial function, then $p^{(2)}$ is seen to depend on

$\left(p^{(1)}\right)^2 = A^2 \sin^2(\omega_{dr}t)$, which by the trigonometric identity $\sin^2(\omega_{dr}t) = \frac{1}{2}\left[1 - \cos(2\omega_{dr}t)\right]$, can be resolved into two terms at 0 and $2\omega_{dr}$ frequencies. The 0 (DC) frequency term does not contribute to the acoustic pressure since it is a constant with time, $\dfrac{\partial^2}{\partial t^2}(\text{Constant}) = 0$ in the right-hand side of Eq. 2.4b. After dropping the DC term, $p^{(2)}$ has just the $2\omega_{dr}$ term. Extension of the analysis to higher perturbation terms will clearly demonstrate how the other harmonics are generated.

When any of these (driven) frequency terms are near the resonant frequency of a standing wave of the cavity, the response may be very strong. The intensity of the response depends on the quality factor Q of the particular resonance and how well the resonant frequency ω_n coincides with the frequency term $n\omega_{dr}$. When the acoustic waves are driven near resonances, Eq. 2.3 can be simplified to a semi-empirical form. The major simplification is performed on the dissipation operator $\mathfrak{S}$ and will be discussed next.

2.1.1 QNE near resonant frequencies of the standing wave

When a (generated) forcing function does not have its frequency $n\omega_{dr}$ close to the ω_n, the standing wave is not excited strongly and the dissipation term in the quadratic nonlinear wave equation (QNE, Eq. 2.3) can be ignored. However, when $n\omega_{dr} \sim \omega_n$, the amplitude of the standing wave depends strongly on the quality factor Q_n of the resonance and the dissipation term must be retained. The Q_n is an empirical quantity measuring the *sharpness* of a resonance and can be written as

$$Q_n = \frac{\omega_n}{\omega_{n2} - \omega_{n1}}, \qquad (2.5)$$

where ω_n is the nth resonant frequency and ω_{n1} and ω_{n2} the lower and upper half-power points. The quality factor can also be defined as an ratio of the energy within the system (the standing wave) to the average energy lost per radian when the system is at a resonant frequency[5]. Clearly, a higher Q signifies a less dissipative system. In the case of a forced standing wave inside a cavity, a higher Q_n will result in a higher amplitude wave, especially near a resonant frequency. The values of Q_n and ω_n can be determined experimentally, in

---

[5] A. D. Pierce. *Acoustics. An Introduction to Its Physical Principles and Applications*, 122 (1989).

the infinitesimal-amplitude acoustics regime. Coppens and Sanders[1] showed that at near resonance conditions, the classical wave equation operator (left-hand side of Eq. 2.3) can be written as

$$c_0^2 \nabla^2 - \frac{\partial^2}{\partial t^2} + \frac{\partial}{\partial t} \Im \doteq c_n^2 \nabla^2 - \frac{\partial^2}{\partial t^2} - \frac{n\omega_{dr}}{Q_n}\frac{\partial}{\partial t},$$ (2.6)

where c_n is the phase speed for the nth resonance. Since only resonant standing waves contribute significantly when driven near a resonance, the acoustic pressure p can be expressed as a sum of frequency terms $p_1, p_2, \dots p_n$:

$$p = p_1 + p_2 + p_3 + \dots p_n.$$ (2.7)

where the subscript refers to the nth harmonic mode of the forcing frequency ω_{dr}: p_n is of frequency $n\omega_{dr}$.

Combination of Eqs. 2.3, 2.6, and 2.7 results in a semi-empirical QNE, valid when the system is driven near a resonant frequency.

$$\sum_n \left(c_n^2 \nabla^2 - \frac{\partial^2}{\partial t^2} - \frac{n\omega_{dr}}{Q_n}\frac{\partial}{\partial t} \right)\frac{p_n}{\rho_0 c_0^2} = -F_{dr} - \frac{\partial^2}{\partial t^2}\left[\left(\frac{u}{c_0}\right)^2 + \frac{\gamma-1}{2}\left(\frac{p}{\rho_0 c_0^2}\right)^2 \right].$$ (2.8)

Eq. 2.8 will be the starting point for developing a model using effective nonlinear coupling coefficients. Before discussing this model, the following section will investigate applications of Eq. 2.8 in previous projects to determine the practicality of the equation when compared to experimental results.

2.1.2 Experimental results using the QNE

Initial development of the QNE by Coppens and Sanders utilized purely theoretical absorption and dispersion terms. Further research[6] showed that the observed dispersion was not in total agreement with their theoretical model. To compensate, the QNE was modified to include experimentally determined Q_n and ω_n, as seen in Eq. 2.8. With the corrections, the solutions to the semi-empirical model were in excellent agreement with experimental results. In one of their earliest experiments[2], high-amplitude standing waves

---

[6] A. B. Coppens and C. Lane, J. Acoust. Soc. Am. 54, 336 (L) (1973).

were generated in a 6-ft long, 2.5-in diameter rigid-walled tube, with one end sealed and the other end fitted with a piston – the vibration generator. For forcing frequencies near the fundamental or the second resonance, the theory-predicted amplitudes of the nonlinearly excited second and third harmonics matched well with experimental results.

The semi-empirical QNE (Eq. 2.8) was used with similar success in a later[1] experiment using rectangular cavities. In both instances, the authors stressed that finite-amplitude effects are most prominent when the acoustic waves are driven at a frequency for which a normal mode (resonance) of the system is strongly excited. Since nonlinear effects generate *integral* harmonics of frequencies $n\omega_d$, if the normal modes ω_n are not integral multiples of the fundamental (i.e. $\omega_2 \neq 2\omega_1$), then the nonlinear effects cannot attain significant amplitudes. This theory was tested successfully by Gaitan and Atchley (1993)[7] with anharmonic tubes.
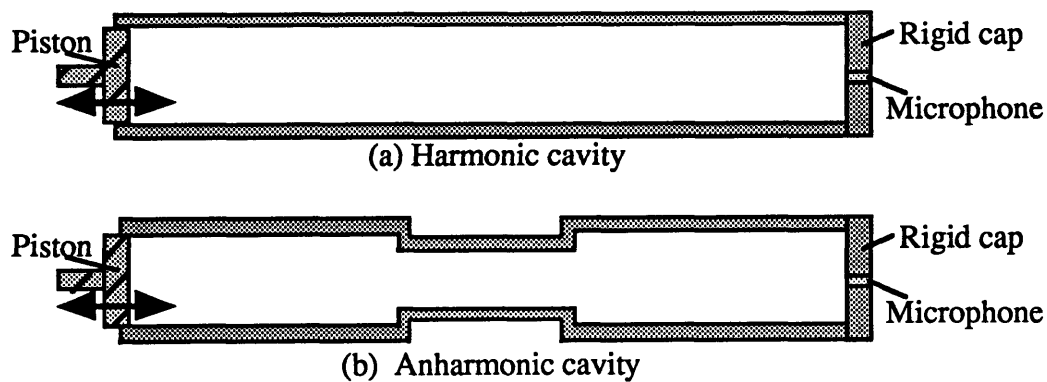
Figure 2.1 Examples of a harmonic cavity and an anharmonic cavity.

By manipulating the geometry of a cavity to one like in Fig. 2.1b, the normal modes of the cavity were detuned, leading to smaller nonlinear effects. Their predictions were also in excellent agreement with experimental results, but only for the lower harmonics and relatively weak forcing functions. One reason for the limitations is due to the order of the nonlinear equation used. Gaitan and Atchley used the second order QNE which neglected third-order (cubic) effects. The third-order effects are initially negligible with weak forcing amplitudes, but become more significant with stronger forcing amplitudes. They may have been able to better their predictions if they had included third-order nonlinear effects in their theory. However, they still would not have been able to

---

[7] D. F. Gaitan and A. A. Atchley, J. Acoust. Soc. Am. 93, 2489-2495 (1993).

measure third-order effects directly, because experimentally, the response measured includes *both* second and third-order effects. Although the main objective of this thesis is not to predict amplitudes of harmonics but rather to suppress the harmonics, the active control approach can be used to directly probe the cubic coupling effects by suppressing the quadratic coupling effects. The following section will introduce a set of nonlinear wave equations using effective nonlinear coupling coefficients. These equations are simpler to work with and will demonstrate the generation of nonlinear effects more clearly.

2.2 Nonlinear wave equations with effective coupling coefficients

The semi-empirical QNE (Eq. 2.8) related the mode-dependent dissipation terms to the second-order, quadratic, nonlinear operator:

$$\sum_n \left(c_n^2 \nabla^2 - \frac{\partial^2}{\partial t^2} - \frac{n\omega_{dr}}{Q_n}\frac{\partial}{\partial t} \right)\frac{p_n}{\rho_0 c_0^2} = -F_{dr} - \frac{\partial^2}{\partial t^2}\left[\left(\frac{u}{c_0}\right)^2 + \frac{\gamma-1}{2}\left(\frac{p}{\rho_0 c_0^2}\right)^2 \right], \qquad (2.8)$$

where p_n is the nth harmonic, u and p are the total acoustic velocity and pressure: $u = \sum_n u_n$ and $p = \sum_n p_n$. In the following analysis, the quadratic nonlinear operator (the second term on the right-hand-side of Eq. 2.8) is replaced with $\varepsilon_{quad}p^2$, where p is the total acoustic pressure and ε_{quad} is assumed to be a real, positive constant. Eq. 2.8 is then of the following form:

$$\sum_n \left(c_n^2 \nabla^2 - \frac{\partial^2}{\partial t^2} - \frac{n\omega_{dr}}{Q_n}\frac{\partial}{\partial t} \right)\frac{p_n}{c_0^2} = -F_{dr} - \varepsilon_{quad}p^2. \qquad (2.9)$$

ε_{quad}, the *effective quadratic* nonlinear coupling coefficient is strictly speaking, not a constant, it is mode-dependent. In the original quadratic nonlinear operator, the time derivative $\partial^2/\partial t^2$ on the u^2 and p^2 produces mode-dependent terms which are clearly not constant. However, in the interest of simplicity, ε_{quad} has been assumed constant since only a few modes are investigated. The value of ε_{quad} is found by measuring the coupling between the fundamental harmonic and the second harmonic.

For higher acoustic pressure amplitudes, cubic coupling is modeled by the addition of a third term to the overall forcing function in Eq. 2.9 The equation with both quadratic and cubic nonlinear coupling can then be written:

$$\sum_n \left(c_n^2 \nabla^2 - \frac{\partial^2}{\partial t^2} - \frac{n\omega_{dr}}{Q_n} \frac{\partial}{\partial t} \right) \frac{p_n}{c_0^2} = -F_{dr} - \varepsilon_{quad} p^2 - \varepsilon_{cubic} p^3 \,, \qquad (2.10)$$

where ε_{cubic} is another constant to be found experimentally.

As indicated in the previous section, the acoustic pressure p can be expressed by two different series, Eqs. 2.2a and 2.7. The first series is arranged by the perturbation orders $p^{(i)}$ while the second series is by the frequency components p_n. Although the final solution to compare with the experiments will be in terms of p_n, the subsequent analysis will initially utilize the perturbation approach because the solutions better demonstrate harmonic generation. To use the perturbation approach, however, Eqs. 2.9 and 2.10 must first be rewritten without the frequency series notation. Focusing first on Eq. 2.9, rewrite the linear equation portion (left-hand side) so that the total acoustic pressure p is again present. The following equation will be referred to as the effective quadratic nonlinear wave equation, EQNE:

$$\left(c_0^2 \nabla^2 - \frac{\partial^2}{\partial t^2} + \frac{\partial}{\partial t} \Im \right) \frac{p}{c_0^2} = -F_{dr} - \varepsilon_{quad} p^2 \,. \qquad (2.11)$$

The operator $\Im$ that leads to dissipation and dispersion was shown in the previous section to be significant only when the driving frequency is near a resonant frequency. Furthermore, Eq. 2.6 shows that the operator is frequency and not time-dependent and in the summation form of Eq. 2.8, each dissipation term corresponded to a particular resonant frequency. If Eq. 2.11 is Fourier transformed with respect to *time*, then the following is the result:

$$\left(\frac{\partial^2}{\partial x^2} + \frac{\omega^2}{c_0^2} + i\eta \frac{\omega}{c_0^2} \right) |p\rangle = -|F_{dr}\rangle - \varepsilon_{quad} \lambda |p^2\rangle \,. \qquad (2.12)$$

$|p\rangle$ is the Fourier transform of p, $|p^2\rangle$ is the Fourier transform of p^2, $|F_{dr}\rangle$ is the Fourier transform of F_{dr}, i is $\sqrt{-1}$, η is the mode-dependent dissipation operator $\eta = \omega/Q$, and λ is an expansion parameter which will be used later in the perturbation expansion. Ultimately, λ will be set to a value of 1. η is understood to hold the dissipation terms associated with all frequency terms ω present in p. These frequencies are the drive frequencies determined by the input (e.g. piston) forcing function F_{dr}, and the nonlinearly

generated frequencies in $\varepsilon_{quad} p^2$. For example, if the forcing function F_{dr} has a single frequency ω_A (near the fundamental resonance ω_1) and the nonlinear term is neglected, then by Eq. 2.6, $\eta = -\omega_A / Q_1$, $\omega = \omega_A$, and Eq. 2.12 becomes the following:

$$\left(\frac{\partial^2}{\partial x^2} + \frac{\omega_A^2}{c_0^2} - i \frac{\omega_A}{Q_1} \frac{\omega_A}{c_0^2} \right) |p\rangle = -|F_{dr}\rangle . \qquad (2.13)$$

Since the objective does include nonlinear effects, η and ω are expected to consist of many mode-dependent terms. By including all frequency terms in η and ω, Eq. 2.12 is essentially the same as Eq. 2.8 (in Fourier space) with two assumptions. The first assumption is that Eq. 2.12 is only applied to a one-dimensional system ($\nabla^2 = \partial^2/\partial x^2$). This assumption focuses the study on plane waves (in the x-direction) and restricts other types of acoustic waves (e.g. radial) from being generated. The second assumption is that the phase speed c_n be constant and equal to c_0 for all resonances. Utilizing c_n is one way to account for dispersion effects. However, dispersion effects can be maintained, in this analysis, by replacing the calculated resonant frequencies $\omega_{n,calc}$ with those experimentally measured ω_n. The solutions to Eq. 2.12 is found by first replacing $|p\rangle$ with its perturbation terms,

$$|p\rangle = |p^{(1)}\rangle + \lambda |p^{(2)}\rangle + \lambda^2 |p^{(3)}\rangle + \lambda^3 |p^{(4)}\rangle + ..., \qquad (2.14)$$

where λ is the same expansion parameter used in Eq. 2.12.

Eq. 2.12 can be made more compact with the following definitions.

$$|f\rangle = \int_{-\infty}^{+\infty} f(t)e^{-i\omega t} dt , \quad f * g = \frac{1}{2\pi} \int_{-\infty}^{+\infty} f(s)g(s - \omega)ds , \quad \hat{k}^2 = \frac{\omega^2}{c_0^2} + i\eta \frac{\omega}{c_0^2} . \qquad (2.15)$$

The first two definitions are the Fourier transform of f and the convolution integral of f and g, respectively. $\hat{k}^2$, a function of driving frequencies and dissipation, measures the *nearness* of the drive frequency to a resonance. Using these definitions, Eq. 2.12 is rewritten as

$$\left(\frac{\partial^2}{\partial x^2} + \hat{k}^2 \right) |p\rangle = -|F_{dr}\rangle - \varepsilon_{quad}\lambda |p\rangle * |p\rangle . \qquad (2.16)$$

Substituting Eq. 2.14 into Eq. 2.16, and equating coefficients of like powers of λ, the first few terms of $|p\rangle$ are found.

$$\lambda^0: \qquad \left(\frac{\partial^2}{\partial x^2}+\hat{k}^2\right)\left|p^{(1)}\right\rangle=-\left|F_{dr}\right\rangle, \tag{2.17}$$

$$\lambda^1: \qquad \left(\frac{\partial^2}{\partial x^2}+\hat{k}^2\right)\left|p^{(2)}\right\rangle=-\varepsilon_{quad}\left|p^{(1)}\right\rangle*\left|p^{(1)}\right\rangle, \tag{2.18}$$

$$\lambda^2: \qquad \left(\frac{\partial^2}{\partial x^2}+\hat{k}^2\right)\left|p^{(3)}\right\rangle=-2\varepsilon_{quad}\left|p^{(1)}\right\rangle*\left|p^{(2)}\right\rangle, \tag{2.19}$$

$$\lambda^3: \qquad \left(\frac{\partial^2}{\partial x^2}+\hat{k}^2\right)\left|p^{(4)}\right\rangle=-\varepsilon_{quad}\left(2\left|p^{(1)}\right\rangle*\left|p^{(3)}\right\rangle+\left|p^{(2)}\right\rangle*\left|p^{(2)}\right\rangle\right). \tag{2.20}$$

The first-order (linear) response, $\left|p^{(1)}\right\rangle$, depends strictly on the input driving function F_{dr}. The second order response, $\left|p^{(2)}\right\rangle$, depends on the interaction between the linear response with itself. Higher-order responses depend on increasingly complex interactions among lower-order responses. To write an explicit solution for $\left|p^{(1)}\right\rangle$, an orthonormal set of eigenfunctions $|m\rangle$ is assumed to exist for a resonator. $|m\rangle$ is a set of functions that is strictly dependent on x, not t or ω. Noting that $\frac{\partial^2}{\partial x^2}|m\rangle=-k_m^2|m\rangle$ where k_m is the wave number ω_m/c_0 associated with the mth mode (ω_m is the mth resonant frequency), then with some algebra, $\left|p^{(1)}\right\rangle$ is

$$\left|p^{(1)}\right\rangle=-\sum_{m=1}^{\infty}\frac{\langle m|F_{dr}\rangle}{\left(\hat{k}^2-k_m^2\right)}|m\rangle. \tag{2.21}$$

Dirac notation $\langle m|F_{dr}\rangle$ was used here for the integral over the *volume* of the resonator of the product of the functions $|m\rangle$ and $|F_{dr}\rangle$. The resonator will have a sizable response only if $\langle m|F_{dr}\rangle$ is non-zero at a frequency which makes $\hat{k}$ approximately equal to one of the k_m's. The solutions for the higher-order responses have the same form as in Eq. 2.21, with the appropriate drive terms substituted for $|F_{dr}\rangle$.

$$\left|p^{(2)}\right\rangle=-\sum_{m=1}^{\infty}\frac{\langle m|F_{dr2}\rangle}{\left(\hat{k}^2-k_m^2\right)}|m\rangle; \quad \left|F_{dr2}\right\rangle=\varepsilon_{quad}\left|p^{(1)}\right\rangle*\left|p^{(1)}\right\rangle, \tag{2.22}$$

$$\left|p^{(3)}\right\rangle = -\sum_{m=1}^{\infty}\frac{\left\langle m\left|F_{dr3}\right\rangle\right.}{\left(\hat{k}^2 - k_m^2\right)}\left|m\right\rangle; \quad \left|F_{dr3}\right\rangle = 2\varepsilon_{quad}\left|p^{(1)}\right\rangle *\left|p^{(2)}\right\rangle,$$

(2.23)

$$\left|p^{(4)}\right\rangle = -\sum_{m=1}^{\infty}\frac{\left\langle m\left|F_{dr4}\right\rangle\right.}{\left(\hat{k}^2 - k_m^2\right)}\left|m\right\rangle; \quad \left|F_{dr4}\right\rangle = \varepsilon_{quad}\left(2\left|p^{(1)}\right\rangle *\left|p^{(3)}\right\rangle + \left|p^{(2)}\right\rangle *\left|p^{(2)}\right\rangle\right).$$

(2.24)

2.2.1 Harmonics generation using the EQNE

To show harmonic generation, assume a forcing function of amplitude F is driving standing waves at a frequency ω_{dr} near the fundamental resonant frequency of the resonator ω_1, $F_{dr}(t) = F\sin(\omega_{dr}t)$. Although the forcing function can be *spatially-* dependent, only the *time* -dependent term will be retained for the current discussions, since the Fourier transform with respect to time of the complete forcing function, $F_{dr}(x,t) = F_{dr}(x)\cdot F_{dr}(t)$, does not affect the spatial component $F_{dr}(x)$. Thus for the discussions to follow, the volume integral $\left\langle m\left|F_{dr}(x,t)\right\rangle\right.$ is

$$\left\langle m\left|F_{dr}(x,t)\right\rangle\right. = \left[\int\left|m\right\rangle F_{dr}(x)dV\right]\cdot\left|F_{dr}(t)\right\rangle,$$

(2.25)

where only the time-dependent component of the forcing function is in Fourier space. Until the discussion on the modeling of the forcing function is presented in Section 3.2.2, the term *forcing function* F_{dr} will be written as just the time-dependent component $F_{dr}(t)$: $F_{dr}=F_{dr}(t)$. The spatial component $F_{dr}(x)$ is understood to have been incorporated into the volume integral as shown above. Now, the Fourier transform of $F_{dr} = F\sin(\omega_{dr}t)$ is the sum of two Dirac delta functions, $\left|F_{dr}\right\rangle = \beta\left[\delta(\omega + \omega_{dr}) - \delta(\omega - \omega_{dr})\right]$ where β is a constant. In Eq. 2.20, the volume integral $\left\langle m\left|F_{dr}\right\rangle\right.$ does not affect the frequency functions in $\left|F_{dr}\right\rangle$ so $\left|p^{(1)}\right\rangle$ can be written as follows:

$$\left|p^{(1)}\right\rangle = -\sum_{m=1}^{\infty}\frac{\beta\left[\delta(\omega + \omega_{dr}) - \delta(\omega - \omega_{dr})\right]}{\left(\hat{k}^2 - k_m^2\right)}g_m(x),$$

(2.26)

where $g_m(x)$ is the spatial function describing the product of the volume integral and the mth eigenfunction:

$$g_m(x) = \left[\int |m\rangle F_{dr}(x) dV\right] \cdot |m\rangle. \tag{2.27}$$

Since only one driving frequency is present, $\hat{k}^2$ has but one value, associated with

ω_{dr}: $\hat{k}^2 = \dfrac{\omega_{dr}^2}{c_0^2} + i\eta \dfrac{\omega_{dr}}{c_0^2}$, where η is given by $\eta = -\dfrac{\omega_{dr}}{Q_1}$. When the drive frequency

$\omega_{dr} \approx \omega_1$, then $\hat{k}^2 - k_m^2$ is clearly the smallest when $m=1$, at the first resonance. The other eigenmodes are not excited appreciably and can be neglected from the sum, leaving $p^{(1)}$ with just one term at frequency ω_{dr}:

$$p^{(1)} = A \sin(\omega_{dr} t + \theta_{11}) g_1(x), \tag{2.28}$$

where A and θ_{11} are constants to be determined, and $g_1(x) = \left[\int |1\rangle F_{dr}(x) dV\right] \cdot |1\rangle$.

For the second-order solution, Eq. 2.22, the forcing function is the convolution of the first-order solution with itself: $|F_{dr2}\rangle = \varepsilon_{quad} |p^{(1)}\rangle * |p^{(1)}\rangle$. Using the definition of the convolution integral given in Eq. 2.15, $|p^{(1)}\rangle * |p^{(1)}\rangle$ is:

$$|p^{(1)}(\omega)\rangle * |p^{(1)}(\omega)\rangle = \frac{1}{2\pi} \int_{-\infty}^{+\infty} |p^{(1)}(s)\rangle \cdot |p^{(1)}(s-\omega)\rangle ds. \tag{2.29}$$

The integrand consists of four terms,

$$|p^{(1)}(s)\rangle \cdot |p^{(1)}(s-\omega)\rangle = \beta_1 \delta(s - \omega_{dr}) \delta(\omega - s - \omega_{dr}) + \beta_2 \delta(s - \omega_{dr}) \delta(\omega - s + \omega_{dr})$$
$$+ \beta_3 \delta(s + \omega_{dr}) \delta(\omega - s - \omega_{dr}) + \beta_4 \delta(s + \omega_{dr}) \delta(\omega - s + \omega_{dr}),$$

where β_1, β_2, β_3, and β_4 are appropriate coefficients that include spatial-dependent terms from $p^{(1)}$. Integrating these terms with respect to s as shown in Eq. 2.29 results in the following form for the forcing function on $|p^{(2)}\rangle$,

$$|F_{dr2}\rangle = \beta_1' \delta(\omega - 2\omega_{dr}) + \beta_2' \delta(\omega) + \beta_3' \delta(\omega) + \beta_4' \delta(\omega + 2\omega_{dr}). \tag{2.30}$$

where β_1', β_2', β_3', and β_4' are appropriate coefficients. Again, the volume integral in Eq. 2.22 does not affect these frequency terms, so that $|p^{(2)}\rangle$ is of the form:

$$|p^{(2)}\rangle = -\sum_{m=1}^{\infty} \frac{\langle m| \beta_1' \delta(\omega - 2\omega_{dr}) + \beta_2' \delta(\omega) + \beta_3' \delta(\omega) + \beta_4' \delta(\omega + 2\omega_{dr})\rangle}{\left(\hat{k}^2 - k_m^2\right)} |m\rangle. \tag{2.31}$$

The resultant frequency terms generated for $p^{(2)}$ are recognized to be the *sum* and *difference* of the frequency terms in $p^{(1)}$. In this instance, $p^{(1)}$ had just one frequency term ω_{dr}, thus the frequency terms in $p^{(2)}$ are 0 and $2\omega_{dr}$. Recalling that a DC term does not contribute to the response, the second and third term in the forcing function above are dropped. Then, by Eq. 2.22, if $2\omega_{dr} \approx \omega_2$, then $\hat{k}^2 - k_m^2$ will be smallest at $m=2$ and $p^{(2)}$ will oscillate at $2\omega_{dr}$ with one dominant spatial dependence corresponding to the second eigenmode $|2\rangle$:

$$p^{(2)} = B\sin(2\omega_{dr}t + \theta_{22})g_2(x). \tag{2.32}$$

The constants to be found, B and θ_{22} depend on $\hat{k}^2 - k_m^2$ where $k_m^2 = \dfrac{\omega_2^2}{c_0^2}$,

$\hat{k}^2 = \dfrac{(2\omega_{dr})^2}{c_0^2} + i\eta\dfrac{2\omega_{dr}}{c_0^2}$, and $\eta = -\dfrac{2\omega_{dr}}{Q_2}$. $g_2(x)$ is the spatial function that combines the volume integral with the second eigenmode in Eq. 2.31. Clearly, $p^{(2)}$ will oscillate at the $2\omega_{dr}$ frequency, but its magnitude B depends strongly on how close this frequency matches that of the second resonant frequency ω_2.

When the analysis is extended to solve for the third-order solution $p^{(3)}$, two frequency terms will be generated, ω_{dr} and $3\omega_{dr}$, written here so the values of $\hat{k}^2$ can be discussed:

$$|p^{(3)}\rangle = -\sum_{m=1}^{\infty}\frac{\langle m|\gamma_1\delta(\omega-\omega_{dr})+\gamma_2\delta(\omega+\omega_{dr})+\gamma_3\delta(\omega-3\omega_{dr})+\gamma_4\delta(\omega+3\omega_{dr})\rangle}{\left(\hat{k}^2-k_m^2\right)}|m\rangle, \tag{2.33}$$

where γ_1', γ_2', γ_3', and γ_4' are appropriate coefficients. The two values of $\hat{k}^2$ that result in the largest terms of the summation series, now with appropriate subscripts that correspond to the two generated harmonic frequencies, are

For frequency $\omega_{dr} \approx \omega_1$, $\qquad \hat{k}_1^2 = \dfrac{\omega_{dr}^2}{c_0^2} + i\eta_1\dfrac{\omega_{dr}}{c_0^2}$, $\qquad \eta_1 = -\dfrac{\omega_{dr}}{Q_1}$, $\qquad$ (2.34)

For frequency $3\omega_{dr} \approx \omega_3$, $\qquad \hat{k}_3^2 = \dfrac{(3\omega_{dr})^2}{c_0^2} + i\eta_3\dfrac{3\omega_{dr}}{c_0^2}$, $\qquad \eta_3 = -\dfrac{3\omega_{dr}}{Q_3}$. $\qquad$ (2.35)

With Eqs. 2.34 and 2.35, the two frequency terms in Eq. 2.33 can be separated, resulting in the following:

$$p^{(3)} = \sum_{m=1}^{\infty} \frac{C_1' \sin(\omega_{dr} t + \theta_{31}')}{\left(\hat{k}_1^2 - k_m^2\right)} g_m(x) + \sum_{m=1}^{\infty} \frac{C_3' \sin(3\omega_{dr} t + \theta_{33}')}{\left(\hat{k}_3^2 - k_m^2\right)} g_m(x), \qquad (2.36)$$

where C_1', C_3', θ_{31}', and θ_{33}' are constants to be determined. The two sums can be replaced with their dominant terms which correspond to $m=1$ and $m=3$, respectively. Thus the third-order response will have two frequency terms that have maximum amplitudes when the appropriate eigenmodes are excited:

$$p^{(3)} = \frac{C_1' \sin(\omega_{dr} t + \theta_{31}')}{\left(\hat{k}_1^2 - k_1^2\right)} g_1(x) + \frac{C_3' \sin(3\omega_{dr} t + \theta_{33}')}{\left(\hat{k}_3^2 - k_3^2\right)} g_3(x),$$

$$p^{(3)} = C_1 \sin(\omega_{dr} t + \theta_{31}) g_1(x) + C_3 \sin(3\omega_{dr} t + \theta_{33}) g_3(x), \qquad (2.37)$$

where C_1, C_3, θ_{31}, and θ_{33} are constants to be determined. Following the same procedure, $p^{(4)}$ can be seen to be composed of two frequency terms, $2\omega_{dr}$ and $4\omega_{dr}$:

$$p^{(4)} = D_2 \sin(2\omega_{dr} t + \theta_{42}) g_2(x) + D_4 \sin(4\omega_{dr} t + \theta_{44}) g_4(x), \qquad (2.38)$$

where D_2, D_4, θ_{42}, and θ_{44} are constants to be determined.

The preceding analysis was for the EQNE, Eq. 2.11, when the nonlinear coupling was assumed quadratic. If cubic nonlinear coupling effects are introduced, then more harmonic frequency terms will be generated. This will be the subject of discussion in the following section.

2.2.2 Harmonics generation using the ECNE

Cubic coupling effects are introduced into the nonlinear wave equations when quadratic effects alone do not adequately describe the physical phenomenon of nonlinear coupling. Thus for the following analysis, the effective cubic nonlinear wave equation (ECNE) will include both quadratic and cubic coupling effects. The ECNE is simply Eq. 2.11 with an additional term:

$$\left(c_0^2 \nabla^2 - \frac{\partial^2}{\partial t^2} + \frac{\partial}{\partial t}\Im\right)\frac{p}{c_0^2} = -F_{dr} - \varepsilon_{quad}p^2 - \varepsilon_{cubic}p^3 .$$ (2.39)

Assuming the cubic coupling effects is an order lower than the quadratic coupling effects, then, when the expansion parameter λ is introduced as before in Eq. 2.12, the following is the result.

$$\left(\frac{\partial^2}{\partial x^2} + \frac{\omega^2}{c_0^2} + i\eta\frac{\omega}{c_0^2}\right)|p\rangle = -|F_{dr}\rangle - \varepsilon_{quad}\lambda|p^2\rangle - \varepsilon_{cubic}\lambda^2|p^3\rangle .$$ (2.40)

Following the identical procedure used in finding the responses to the EQNE, the solutions to the ECNE, to the first four orders are as follows.

$$|p^{(1)}\rangle = -\sum_{m=1}^{\infty}\frac{\langle m|F_{dr}\rangle}{\left(\hat{k}^2 - k_m^2\right)}|m\rangle ,$$ (2.41)

$$|p^{(2)}\rangle = -\sum_{m=1}^{\infty}\frac{\langle m|F_{dr2}\rangle}{\left(\hat{k}^2 - k_m^2\right)}|m\rangle ; \qquad |F_{dr2}\rangle = \varepsilon_{quad}|p^{(1)}\rangle * |p^{(1)}\rangle ,$$ (2.42)

$$|p^{(3)}\rangle = -\sum_{m=1}^{\infty}\frac{\langle m|F_{dr3}\rangle}{\left(\hat{k}^2 - k_m^2\right)}|m\rangle ; \qquad \begin{aligned}|F_{dr3}\rangle &= 2\varepsilon_{quad}|p^{(1)}\rangle * |p^{(2)}\rangle \\ &+ \varepsilon_{cubic}|p^{(1)}\rangle * |p^{(1)}\rangle * |p^{(1)}\rangle\end{aligned} ,$$ (2.43)

$$|p^{(4)}\rangle = -\sum_{m=1}^{\infty}\frac{\langle m|F_{dr4}\rangle}{\left(\hat{k}^2 - k_m^2\right)}|m\rangle ; \qquad \begin{aligned}|F_{dr4}\rangle &= \varepsilon_{quad}\left(2|p^{(1)}\rangle * |p^{(3)}\rangle + |p^{(2)}\rangle * |p^{(2)}\rangle\right) \\ &+ 3\varepsilon_{cubic}|p^{(1)}\rangle * |p^{(1)}\rangle * |p^{(2)}\rangle\end{aligned} .$$ (2.44)

The first and second-order solutions are, as expected, the same as the first and second-order solutions to the EQNE. The third-order solution $|p^{(3)}\rangle$, however, has an extra cubic coupling term that also generates two harmonics. Suppose as before, the input forcing function F_{dr} is of frequency ω_{dr} (near the first resonant frequency ω_1 of the resonator), then the drive term F_{dr3} will generate a total of two harmonics. The first component of F_{dr3} generates a ω_{dr} and a $3\omega_{dr}$ harmonic through the interaction between $|p^{(2)}\rangle$ and $|p^{(1)}\rangle$. The second component of F_{dr3} also generates a ω_{dr} and a $3\omega_{dr}$ harmonic, however, the interaction is between $|p^{(1)}\rangle$ and *itself*. Thus, pure cubic coupling will generate a third harmonic $3\omega_{dr}$ without the presence of a second harmonic $2\omega_{dr}$. The

frequency convolution integrals in Eq. 2.44 show that quadratic and cubic coupling effects will both generate the same harmonic frequencies, $2\omega_{dr}$ and $4\omega_{dr}$. Table 2.1 shows the frequency terms generated for up to the fourth-order solutions for the EQNE and ECNE when the input drive frequency is ω_{dr}.

Perturbation order	EQNE (Eq. 2.11)	ECNE (Eq. 2.39)
$p^{(1)}$	ω_{dr}	ω_{dr}
$p^{(2)}$	$2\omega_{dr}$	$(2\omega_{dr})_{quad}$
$p^{(3)}$	$\omega_{dr}, 3\omega_{dr}$	$(\omega_{dr}, 3\omega_{dr})_{quad}$, $(\omega_{dr}, 3\omega_{dr})_{cubic}$
$p^{(4)}$	$2\omega_{dr}, 4\omega_{dr}$	$(2\omega_{dr}, 4\omega_{dr})_{quad}$, $(2\omega_{dr}, 4\omega_{dr})_{cubic}$

Table 2.1 Frequencies present in quadratic and cubic responses, up to fourth-order.

When the nonlinear coupling is only of quadratic order, Table 2.1 shows that the first four perturbation order solutions correspond approximately to the first four frequency terms of p, $p^{(n)} \approx p_n$, $n = 1, 2, 3, 4$. This is true because the ω_{dr} term in $p^{(3)}$ is two orders smaller than the ω_{dr} term from $p^{(1)}$, and the $2\omega_{dr}$ term in $p^{(4)}$ is also two orders smaller than the $2\omega_{dr}$ term in $p^{(2)}$. However, with the additional cubic coupling effects present, more terms are generated in each perturbation order. The total effect of the additional terms is unclear and thus approximating the perturbation order solutions to the frequency terms of p is not appropriate. Fortunately, the objective is to *suppress* nonlinear effects, thus the goal is to control the larger quadratic coupling effects before cubic coupling effects are considered. How energy is transferred from one harmonic to another with quadratic coupling effects is discussed next.

2.2.3 Energy transfer path for quadratic coupling

The frequency convolution integral $|p^{(1)}\rangle * |p^{(1)}\rangle$ provided the mechanism for energy to leak from $p^{(1)}$ to $p^{(2)}$ in Eq. 2.22. Interactions between $p^{(2)}$ and $p^{(1)}$ then allow further energy from $p^{(1)}$ to leak into $p^{(3)}$ and so on. Graphically, the energy transfer path is illustrated in Fig. 2.2. In a), with a nonzero $p^{(2)}$, energy is leaked into higher-order responses. However, in b), if $p^{(2)}$ is somehow suppressed, then no energy can be leaked to the higher-order responses, as shown by the dashed lines and shaded boxes.
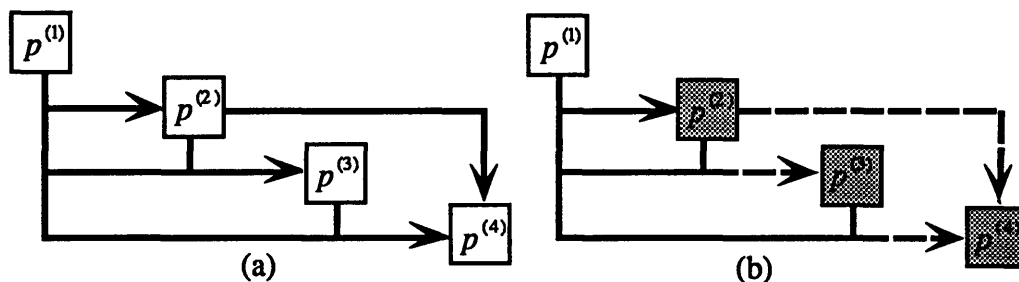
Figure 2.2 *Quadratic nonlinear response, up to fourth-order solutions.*
a) Energy leakage path with nonzero $p^{(2)}$, b) Energy leakage path with $p^{(2)} = 0$.

The question is: *how can $p^{(2)}$ be suppressed*? One method is to design an anharmonic resonator such that its resonant frequencies are not integral multiples of the fundamental, $\omega_n \neq n\omega_1$. When such a resonator is driven near its fundamental resonant frequency $\omega_{dr} \approx \omega_1$, the harmonic generated, with frequency $2\omega_{dr}$, will have a *non-resonant* response because $\left(\hat{k}_2^2 - k_2^2\right)$ is large in Eq. 2.22. Thus, with a small $p^{(2)}$, the higher-order responses will be small as well. As stated before, this method of suppressing energy leakage through nonlinear effects is currently used for both the thermoacoustic devices and sonic compressors. However, another possible approach is to add an additional (frequency) term to F_{dr} which generates a term that cancels with $p^{(2)}$. Since $p^{(2)}$ has only a $2\omega_{dr}$ component, clearly, the additional term to F_{dr} should also be of frequency $2\omega_{dr}$. This approach was discussed briefly in Chapter 1 and will be the main topic of Chapter 3.

Chapter 3 Active Control Approach

T he theory of nonlinear waves in confined geometries was presented in the last chapter, with the emphasis on a model based on effective nonlinear coupling coefficients. In the case of just quadratic coupling, the discussion on solutions to the quadratic EQNE showed that by suppressing the second-harmonic response, p_2, no other (higher) harmonics can be generated, thus disabling the nonlinear effects altogether. This chapter will discuss the method by which the suppression of p_2 can be accomplished by the active control approach. The basic concept is presented in the first section and basic equations established with arbitrary forcing functions and resonator design. In the second section of the chapter, the basic concept is applied theoretically to a specific resonator design. The decision to use a harmonic cavity, versus an anharmonic cavity, will be discussed, the actual forcing functions modeled, and the parameters needed in the computational model presented. Finally, the experimental setup of the active control approach will be discussed in the third section. The actual control loop will be presented, followed by descriptions of some equipment and their functions, as well as some problems encountered.

To clearly understand the objectives of the active control approach, and to establish the data analysis technique to be used later on, the notion of an *amplitude-spectrum* analysis is now discussed. Any waveform, whether periodic or not, can be expressed through a Fourier transform as the sum of many single-frequency terms. The amplitude-spectrum displays the *amplitude* of each of these terms as a function of *frequency*. A purely monotone signal, say $p = |p_1|\sin(\omega_a t + \theta_1)$, where $|p_1|$ is the magnitude of p, ω_a is the signal's oscillation frequency, and θ_1 is the phase, will have exactly one peak in the

amplitude-spectrum plot (Fig. 3.1). The spike has a magnitude of $|p_1|$ and resides on ω_a of the frequency axis.
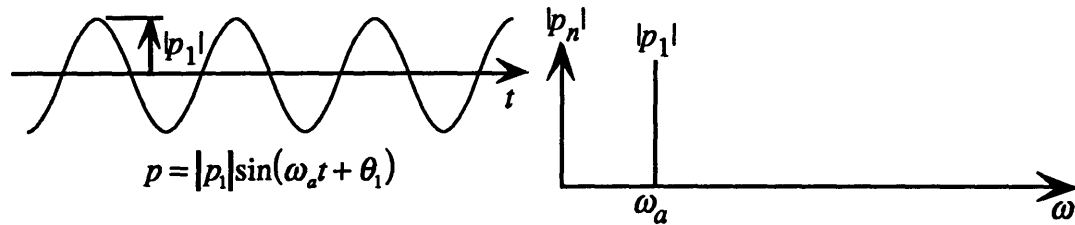
Figure 3.1 Monotone signal (left) and its amplitude spectrum (right).

When a nonlinear wave is analyzed, its frequency components are shown as a series of peaks in Fig. 3.2. The amplitudes of these components depend on the particular resonator design and the forcing function, and the nonlinearities of the acoustic medium.
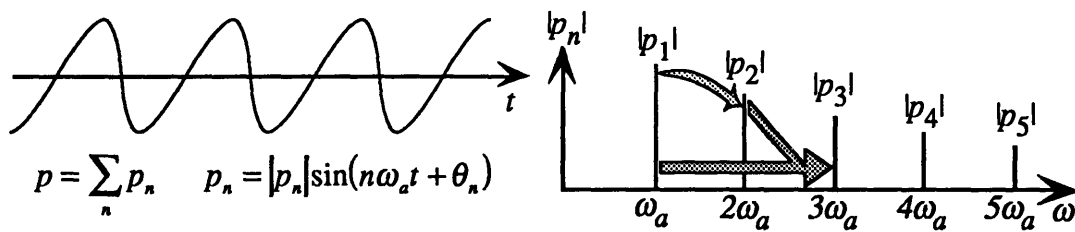
Figure 3.2 Multi-tone signal (left) and its amplitude spectrum (right).

In an acoustic compressor or a thermoacoustic refrigerator, the device is often designed to operate optimally at the fundamental frequency, therefore, the transfer of energy to higher harmonics represents a parasitic loss[1]. The path of energy transfer for the EQNE case starts from the fundamental to the second harmonic, then interaction between the fundamental and the second harmonic generates the third harmonic as discussed in Chapter 2 and shown schematically in Fig. 3.2, above.

---

[1] D. F. Gaitan and A. A. Atchley, J. Acoust. Soc. Am. **93**, 2489-2495 (1993).
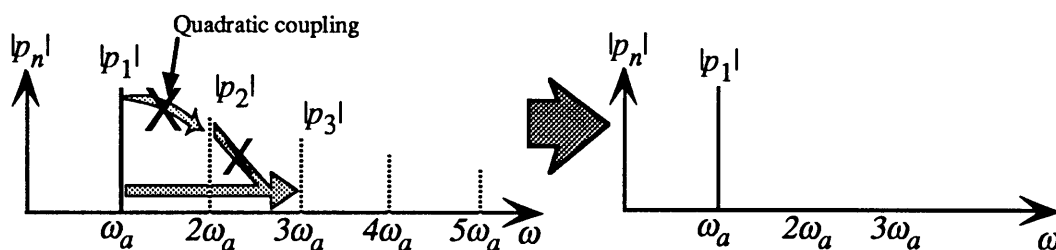
Figure 3.3 Preventing the second harmonic from being generated eliminates all higher harmonics.

If the generation of the second harmonic can be prevented (Fig. 3.3), then *no* subsequent harmonic can be generated. The preceding is only true when only quadratic nonlinear coupling exists. When cubic nonlinear coupling exists, in addition to the quadratic, solutions to the ECNE show that both the second *and* third harmonics must be eliminated to prevent leakage to higher harmonics (Fig. 3.4). The third harmonic (p_3) must also be curtailed because it is generated by just the fundamental component, not by the interaction between p_1 and p_2 in the EQNE case.
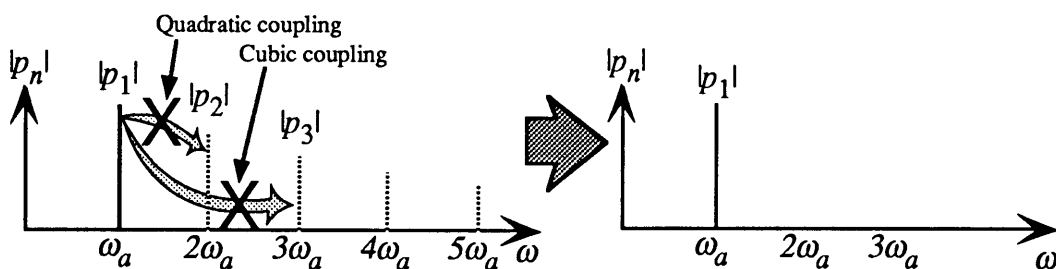
Figure 3.4 With an addition cubic coupling, both second and third harmonics need to be quenched.

The objectives for using the active control approach in both scenarios are the same: to eliminate the necessary harmonic(s) so that only the fundamental response remains. The basic concept is discussed next.

3.1 Basic Concept: Multiple-Frequency Input Forcing Function

The discussion in Chapter 2 showed how harmonics were generated due to a *single*-tone forcing function F_{dr}, at a frequency ω_{dr} near that of the fundamental resonance of the cavity ω_1. Although nonlinear effects generate all harmonics of the driving frequency, most harmonics can be prevented by quenching just the lowest harmonic(s). To eliminate the second harmonic, the active control approach introduces a *second* frequency term into F_{dr}. The second forcing component is to produce a response at the second

41

harmonic frequency $2\omega_{dr}$ so that the total second harmonic p_2 is reduced to a very small value. In effect, there are two components to the second harmonic p_2:

$p_2 = p_2$ (nonlinear response to first drive tone) $+ p_2$ (linear response to second drive tone).

Clearly, both components must be on the same order to result in a small total p_2. The second drive tone can thus be designated the same order as the p_2 (nonlinear response to first drive tone) by using the expansion parameter λ (the value will be eventually be set to 1): $F_{drII} = \lambda F_2 \sin(2\omega_{dr}t + \phi_2)$, where F_2 is the amplitude of the drive, $2\omega_{dr}$ is the frequency, and ϕ_2 is a phase difference relative to the first drive tone. The complete driving function can now be written as follows.

$$F_{dr} = \underbrace{F_1 \sin(\omega_{dr}t)}_{F_{drI}} + \underbrace{\lambda F_2 \sin(2\omega_{dr}t + \phi_2)}_{F_{drII}}. \tag{3.1}$$

To find the solution to the EQNE with the above forcing function, follow the exact same procedures as presented in Section 2.2. Eq. 2.16 thus becomes the following:

$$\left(\frac{\partial^2}{\partial x^2} + \hat{k}^2\right)|p\rangle = -|F_{drI}\rangle - \lambda\left(|F_{drII}\rangle + \varepsilon_{quad}|p\rangle * |p\rangle\right). \tag{3.2}$$

Now, substituting the perturbation series, Eq. 2.13, into Eq. 3.2, and equating coefficients of like powers of λ, the first three terms of $|p\rangle$ are found.

$$|p^{(1)}\rangle = -\sum_{m=1}^{\infty} \frac{\langle m|F_{drI}\rangle}{\left(\hat{k}^2 - k_m^2\right)}|m\rangle, \tag{3.3}$$

$$|p^{(2)}\rangle = -\sum_{m=1}^{\infty} \frac{\langle m|F_{dr2}\rangle}{\left(\hat{k}^2 - k_m^2\right)}|m\rangle; \quad |F_{dr2}\rangle = |F_{drII}\rangle + \varepsilon_{quad}|p^{(1)}\rangle * |p^{(1)}\rangle, \tag{3.4}$$

$$|p^{(3)}\rangle = -\sum_{m=1}^{\infty} \frac{\langle m|F_{dr3}\rangle}{\left(\hat{k}^2 - k_m^2\right)}|m\rangle; \quad |F_{dr3}\rangle = 2\varepsilon_{quad}|p^{(1)}\rangle * |p^{(2)}\rangle. \tag{3.5}$$

Eqs. 3.3 and 3.5 are the same as Eqs. 2.21 and 2.23, the only difference in the perturbation solutions is the extra forcing term $|F_{drII}\rangle$ in the equation for $|p^{(2)}\rangle$. If the cavity has harmonic resonances and if the input driving frequencies are near the

fundamental and second resonances, $\omega_{dr} \approx \omega_1$ and $2\omega_{dr} \approx \omega_2$, then following the steps in Section 2.2.1, the second perturbation solution, $p^{(2)}$, is written as follows.

$$p^{(2)} = p_2 = B\sin(2\omega_{dr}t + \theta_{22})g_2(x) + B'\sin(2\omega_{dr}t + \theta_{22}')g_2'(x). \tag{3.6}$$

The first term is as before (Eq. 2.32), the harmonic generated by the interaction between $p^{(1)}$ with itself. The second term is the response to the additional forcing function. The constants B' and θ_{22}', and the function $g_2'(x)$ are to be determined by the additional forcing tone. Since the first term of Eq. 3.6 is fixed by the first forcing tone, to quench $p^{(2)}$, adjust the parameters to the second forcing tone so the magnitudes of the two terms are equal and the phase difference 180° apart: $Bg_2(x) \approx B'g_2'(x)$, $\theta_{22}-\theta_{22}' \approx 180°$. The adjustable parameters are F_2 and ϕ_2 and can be determined given empirical values of p_1 and p_2 when only the first forcing function is applied. Section 3.2 will discuss in detail the determination of these parameters as well as the effective quadratic nonlinear coupling coefficient ε_{quad}.

Note that for the EQNE, $p^{(2)} = p_2$, since the only frequency dependence in Eq. 3.6 is $2\omega_{dr}$. Clearly, if the term $p^{(2)}$ is small, then by Eq. 3.5, $p^{(3)}$ will also be small. Consequently, all higher order perturbation terms (and therefore higher harmonics) will be negligible.

If cubic nonlinear coupling is included, then a *third* driving tone must be introduced to quench the third harmonic in addition to the second harmonic (Fig. 3.4). The complete driving function would be written as follows, where λ is the expansion parameter used previously.

$$F_{dr} = \underbrace{F_1 \sin(\omega_{dr}t)}_{F_{drI}} + \underbrace{\lambda F_2 \sin(2\omega_{dr}t + \phi_2)}_{F_{drII}} + \underbrace{\lambda^2 F_3 \sin(3\omega_{dr}t + \phi_3)}_{F_{drIII}}. \tag{3.7}$$

The first two orders of the perturbation solution are the same as before, Eqs. 3.3 and 3.4. The third order solution $|p^{(3)}\rangle$ now has the following forcing function:

$$|F_{dr3}\rangle = |F_{drIII}\rangle + 2\varepsilon_{quad}|p^{(1)}\rangle * |p^{(2)}\rangle + \varepsilon_{cubic}|p^{(1)}\rangle * |p^{(1)}\rangle * |p^{(1)}\rangle. \tag{3.8}$$

Of the two harmonic frequencies generated by the quadratic and cubic effects, ω_{dr} and $3\omega_{dr}$, if emphasis is first placed on the latter, then the solution to $p^{(3)}$ would be

$$p^{(3)}(3\omega_{dr}t) = p_3 = \underbrace{C' \sin(3\omega_{dr}t + \theta_{33}')g_3'(x)}_{Third\ forcing\ tone} +$$
$$\underbrace{C \sin(3\omega_{dr}t + \theta_{33})g_3(x)}_{Quadratic\ effects} + \underbrace{C'' \sin(3\omega_{dr}t + \theta_{33}'')g_3''(x)}_{Cubic\ effects}. \tag{3.9}$$

If the second harmonic has already been quenched by the second forcing tone, then in Eq. 3.9, the $3\omega_{dr}$ term created by quadratic effects can be neglected, leaving just two terms for $p^{(3)}$. To quench the component generated by cubic effects, adjust the variables in F_{drIII}: F_3 and ϕ_3.

$$p^{(3)}(3\omega_{dr}t) = p_3 = \underbrace{C' \sin(3\omega_{dr}t + \theta_{33}')g_3(x)}_{Third\ forcing\ tone} + \underbrace{C'' \sin(3\omega_{dr}t + \theta_{33}'')g_3''(x)}_{Cubic\ effects}. \tag{3.10}$$

If a third forcing tone had not been added, then the cubic effects can be observed directly. Thus, in addition to quenching nonlinear effects, active control allows for direct observation of individual coupling effects as well as other phenomena which could not be experimentally shown before.

3.2 Concept applied to specific resonator design

The previous section presented the basic concepts of the active control approach. The discussion assumed arbitrary resonator designs and forcing functions. To carry out the active control approach computationally, this section will discuss the choosing of a specific resonator design. After a design is chosen, the forcing functions will be modeled. Finally, specific variables to the computational model will be discussed and solved for explicitly. Some of these variables are: F_2, ϕ_2, and ε_{quad}, all are necessary in quenching quadratic nonlinear coupling effects. The Q's of resonances and the value of the resonant frequencies are determined empirically, as discussed in Section 3.3 where the experimental setup is presented.

3.2.1 Resonator Design

The concept of the active control approach can be better demonstrated with a harmonic resonator design. The reason is that a harmonic resonator will have more pronounced magnitudes of the generated harmonics p_2, p_3, p_4, etc. The quenching of these harmonics is clearly evident in an amplitude-spectrum plot. However, with an anharmonic

cavity, quenching of the harmonics is not as dramatic since the harmonics are already of small values.

Before choosing a harmonic resonator design, a question arises: will the quenching process be more difficult to execute in a harmonic than in an anharmonic resonator? This question comes about due to experimental concerns that the resonant frequencies may drift during the quenching process due to temperature fluctuations and other factors. Drifts in the resonant frequencies will affect the magnitudes of the harmonics more strongly in a harmonic resonator. Since the objective is to quench the harmonics, will the changing magnitudes of the harmonics require changes to the quenching forces (F_{drII}, F_{drIII}), to keep the harmonics quenched? If the answer is yes, then quenching harmonics in a harmonic cavity should be more difficult since the changes in the harmonics magnitudes are greater. To answer these questions, first recall that the magnitudes of the harmonics is a strong function of $\left(\hat{k}_n^2 - k_m^2\right)^{-1}$ (see Section 2.2.1), where k_m^2 is associated with the mth resonant frequency and $\hat{k}_n^2$ with the nth harmonic frequency as shown here.

$$k_m^2 = \frac{\omega_m^2}{c_0^2},$$
(3.11)

$$\eta_n = -\frac{n\omega_{dr}}{Q_m}, \qquad \hat{k}_n^2 = \frac{\left(n\omega_{dr}\right)^2}{c_0^2} + i\eta_n \frac{n\omega_{dr}}{c_0^2} = \frac{\left(n\omega_{dr}\right)^2}{c_0^2}\left[1 - \frac{i}{Q_m}\right].$$
(3.12)

Q_m is the quality factor of the mth resonance nearest to the nth harmonic: $\omega_m \sim n\omega_{dr}$. Given these definitions, the following is the result, where K is a function of $n\omega_{dr}$ and ω_m.

$$K\left(n\omega_{dr}, \omega_m\right) = \left(\hat{k}_n^2 - k_m^2\right)^{-1} = \left\{\frac{\left(n\omega_{dr}\right)^2}{c_0^2}\left[1 - \frac{i}{Q_m}\right] - \frac{\omega_m^2}{c_0^2}\right\}^{-1}.$$
(3.13)

Since the quality factors are typically several hundred in value, Eq. 3.13 shows that the magnitude of K will be largest when $n\omega_{dr} \approx \omega_m$. For harmonic resonators, $\omega_m = m\omega_1$, thus if $\omega_{dr} \approx \omega_1$, then $n\omega_{dr} \approx \omega_n$ and K will be large. For anharmonic resonators, $\omega_m \neq m\omega_1$, thus when $\omega_{dr} \approx \omega_1$, $n\omega_{dr} \neq \omega_n$ ($n \geq 2$) and K will be small.

In a harmonic resonator, because K is so sensitive to ω_{dr} and ω_m, if either value is even slightly changed, K will change dramatically. For example, if Q_2 is 200 and the second resonant frequency changes by 0.5% (corresponding to a temperature change of

about $1°$ F to $2°$ F): $(\omega_2)_{new}=1.005(\omega_2)_{old}$, then the magnitude of $K(2\omega_{dr},\omega_2)$ is reduced by 55%. The K change is not as dramatic in an anharmonic resonator. Does this change in the value of K affect the quenching process in the active control approach? In quenching the second harmonic p_2, the two terms in Eq. 3.6 are both dependent directly on $K(2\omega_{dr},\omega_2)=\left(\hat{k}_2^2 - k_2^2\right)^{-1}$. However, since the desired result requires the *sum* of the two terms to equal *zero*, the function K can be factored out of both terms. This can be shown explicitly by reverting Eq. 3.6 to Fourier space and using Eq. 3.4:

$$|p^{(2)}\rangle = -\frac{\langle 2|F_{drll}\rangle}{\left(\hat{k}_2^2 - k_2^2\right)}|2\rangle - \frac{\langle 2|\varepsilon_{quad}\left(p^{(1)}\right)^2\rangle}{\left(\hat{k}_2^2 - k_2^2\right)}|2\rangle. \quad (3.14)$$

When the sum is set to zero, noting that the functions K and $|2\rangle$ are common factors, the following is the result:

$$0=\langle 2|F_{drll}\rangle+\langle 2|\varepsilon_{quad}\left(p^{(1)}\right)^2\rangle, \quad (3.15)$$

where F_{drll} was defined as the second driving tone in Eq. 3.1, $F_{drll} = F_2\sin\left(2\omega_{dr}t+\phi_2\right)$. Eq. 3.15 will be used later to determine the values of F_2 and ϕ_2 for the second driving tone. The interesting result, however, is that slight changes to ω_{dr} or ω_m will <u>not</u> affect the quenching process. The *individual* terms of Eq. 3.14 will both change in magnitude with a change in K, but the sum remains zero. Thus quenching is *not* more difficult for a harmonic resonator than for an anharmonic resonator. The magnitude of the second driving tone depends only on the *initial* resonant frequency ω_2, and not the changes that may occur during the quenching process.

Of the many types of harmonic resonator designs, the simplest is the right circular cylinder. The following presents a discussion on this type of resonator and why it cannot be used for the planned experimental setup. Then the chosen design is presented and its eigenfunctions found.

3.2.1 (a) Straight Cylinder

Fig. 3.5 shows an example of earlier resonator setups used by past investigators[2]. The piston at the left-end excites the gas (air) inside the resonator, setting up an intense standing wave whose magnitude is measured at the right, closed-end.
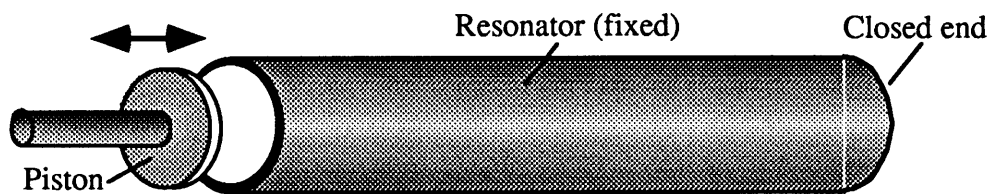
Figure 3.5 Previously used harmonic resonator setup.

To avoid problems of sliding or flexing seals present in a piston setup, both ends can be sealed and the *entire* resonator driven by a shaker, a device that supplies vibrational excitation to a test object. The shaker is an integral component of a vibration and shock test system which tests dynamic stability of items such as automobile parts like head lamps and clocks. The items are typically mounted directly to the shaker armature which vibrates with the designated force and frequency. Here, the mounting for the resonator could be secured with bolts, as shown in Fig. 3.6a. When the entire resonator is vibrated back and forth, the source of the forcing function on the gas inside can be envisaged as two pistons moving in tandem at the two ends (Fig. 3.6b).
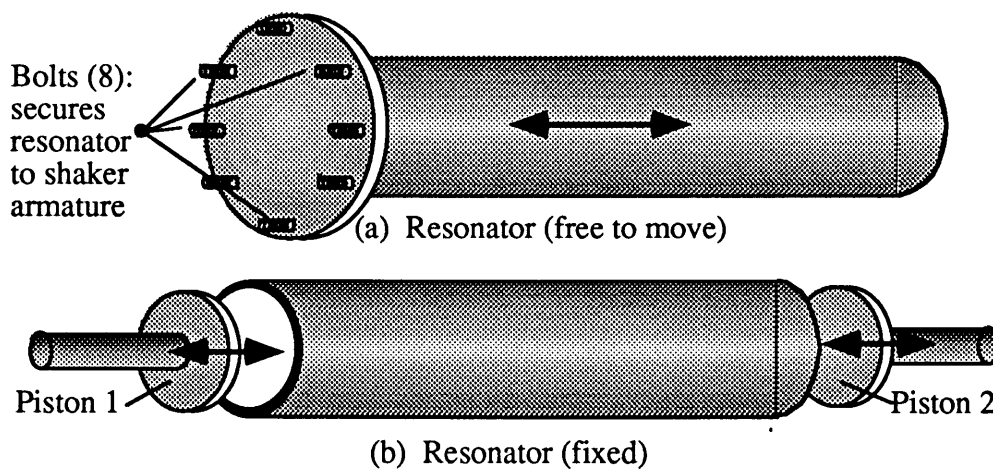
Figure 3.6 Enclosed resonator secured to shaker and its modeled setup.

---

[2] Coppens, 1968, and Gaitan, 1993.

Having two pistons moving in tandem presents another problem for the right circular cylinder cavity: the even modes cannot be excited by the pistons. For example, the second acoustic pressure mode $2\omega_0$ can be shown to have the spatial function shown in Fig. 3.7a. The fluid velocity is the same as the piston velocity at both ends while the fluid pressure is equal in magnitude and phase at the piston faces. In an odd mode (Fig. 3.7b), the piston velocities remain unchanged, but the fluid pressures are now out of phase by π.
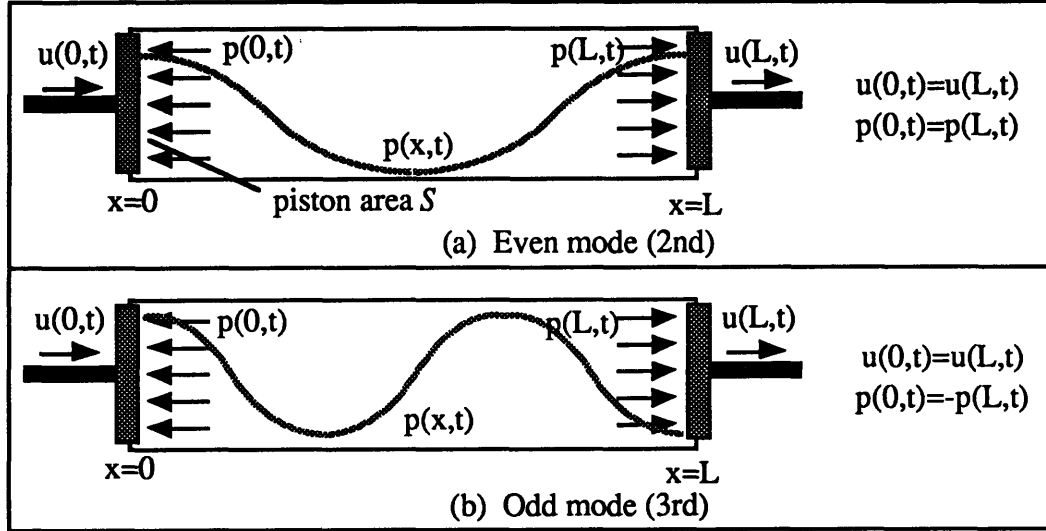
Figure 3.7 Even and odd mode pressure profiles in cylindrical resonator.
a) The second mode. b) The third mode. p(x,t) and u(x,t) are the acoustic pressure and velocity.

To setup a standing wave of any mode, power must be continuously supplied into the fluid by the piston faces. The power is calculated as the time average of the force (pressure p times area S) on the pistons and the velocity of the pistons. In the even mode, the average input power $\dot{W}_{av,even}$ is zero:

$$\dot{W}_{av,even} = \tfrac{1}{T}\int_0^T S[p(0,t)u(0,t) - p(L,t)u(L,t)]dt = 0, \qquad (3.16)$$

where T is the period of oscillation, $p(0,t)$ and $u(0,t)$ are the acoustic pressure and velocity at $x=0$ and time t, respectively, and $p(L,t)$ and $u(L,t)$ are the acoustic pressure and velocity at $x=L$, respectively. Without input power, a second forcing tone will be unable to quench the *nonlinearly* generated second harmonic p_2.

$$\dot{W}_{av,odd} = \tfrac{1}{T}\int_0^T S[p(0,t)u(0,t) - p(L,t)u(L,t)]dt = \tfrac{1}{T}\int_0^T 2S[p(0,t)u(0,t)]dt \qquad (3.17)$$

48

The net power into an odd mode, $\dot{W}_{av,odd}$, is nonzero (Eq. 3.17), thus enabling the generation of a standing wave by the pistons to quench nonlinearly generated odd harmonics. However, since quadratic nonlinear effects are expected stated to be stronger than cubic effects, the emphasis should first be placed on being able to set up the second mode by the pistons. To maintain harmonic resonances in the resonator and to allow for net input power into the even modes (at least the second, $2\omega_0$), a two-radii design was used.

3.2.1 (b) Two-Radii Resonator

In a two-radii resonator (TRR), shown in Fig. 3.8a, if the position of the area transition is at the halfway point, then the resonant frequencies are still integral multiples of the fundamental. However, by having two sections to the resonator, the area transition at the center effectively introduces a third annular piston (Fig. 3.8b).
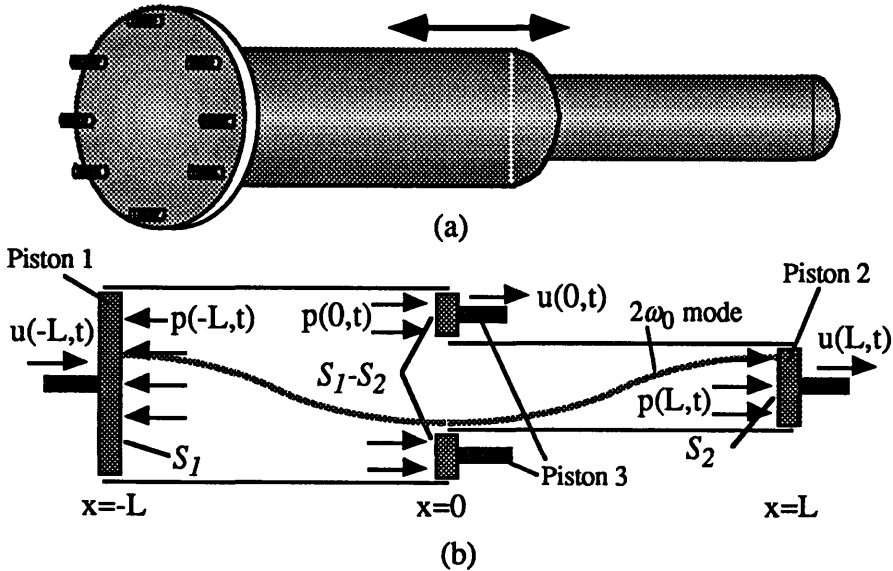
Figure 3.8 Two-radii resonator (TRR).
a) Physical appearance of the TRR. b) The TRR modeled with three pistons at x=-L, 0, and L. The $2\omega_0$ mode wave is shown. p(x,t) and u(x,t) are the acoustic pressure and velocity, S_1 and S_2 are the two areas.

Although the end pressures (at $x=\pm L$) are still the same for the second mode, the areas of the pistons have changed, S_1 is the area of piston at $x=-L$, and S_2 is the area of the piston at $x=L$. In addition, an annular piston with area S_1-S_2 now acts on the fluid at $x=0$ where the pressure is out of phase by π. The net input power into the second mode for the

TRR, $\dot{W}_{2,TRR}$, is then calculated as follows, noting $p(-L,t)=p(L,t)=-p(0,t)$ and $u(-L,t)=u(L,t)=u(0,t)$.

$$\dot{W}_{2,TRR}=\tfrac{1}{T}\int_0^T\left\{\left[S_1 p(-L,t)u(-L,t)\right]-\left[(S_1-S_2)p(0,t)u(0,t)\right]-\left[S_2 p(L,t)u(L,t)\right]\right\}dt$$

$$=\tfrac{1}{T}\int_0^T 2(S_1-S_2)p(-L,t)u(-L,t)dt.$$

(3.18)

The average power transfer is clearly nonzero for the second mode unless area S_1 is equal to area S_2, or the case of a straight cylinder. Eq. 3.18 shows that the amount of power that can be coupled into the $2\omega_0$ mode depend on the area ratio S_1/S_2 ; a larger ratio will lead to stronger coupling between the drive and the second resonant mode.

Eigenfunctions of the TRR
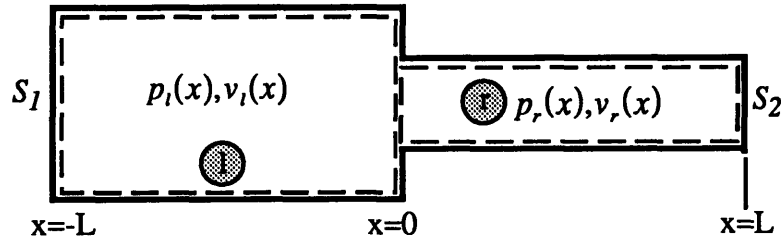
Figure 3.9 TRR modeled in two sections.
$p_l(x)$ and $v_l(x)$ are the spatial acoustic pressure and velocity in the left half, respectively. $p_r(x)$ and $v_r(x)$ are the pressure and velocity in the right half of the resonator.

Here we generate the orthonormal set of eigenfunctions $|m\rangle$ for the TRR. In Fig. 3.9. $p_l(x)$ and $v_l(x)$ are the pressure and velocity of the fluid in the left section. $p_r(x)$ and $v_r(x)$ are the pressure and velocity of the fluid in the right section. The four boundary conditions are

1)	@ $x=0$,	$p_l(0)=p_r(0)$ (continuous pressure),
2)	@ $x=0$,	$S_1 v_l(0)=S_2 v_r(0)$ (continuity),
3)	@ $x=-L$,	$v_l=0$,
4)	@ $x=+L$,	$v_r=0$.

(3.19)

The eigenfunctions are found using standing wave solutions:

$$p_l = A\sin kx + B\cos kx \qquad (-L\le x\le 0),$$
$$p_r = C\sin kx + D\cos kx \qquad (0<x\le +L),$$

(3.20)

where A, B, C, D , and k are coefficients determined by the boundary conditions.

The first two boundary conditions result in $B=D$ and $C=S_rA$, where $S_r=S_1/S_2$. Applying the last two conditions yields

$$k_n = \frac{n\pi}{2L} \quad (n = 1, 2, 3, ...).$$

(3.21)

As expected, k is discrete, designating the eigenmodes of the TRR. If n is odd, then B is found to equal 0; if n is even, then $A=0$. Thus the eigenfunctions can now be written as follows.

$$Odd \ n's: \quad p_{ln} = A\sin(k_nx); \quad p_{rn} = S_rA\sin(k_nx)$$

$$Even \ n's: \quad p_{ln} = p_{rn} = B\cos(k_nx)$$

(3.22)

Note that the even modes have the same amplitude B throughout the TRR whereas the odd modes change in amplitude from A to S_rA at the transition point (x=0). The first four eigenfunctions are shown in Fig. 3.10.
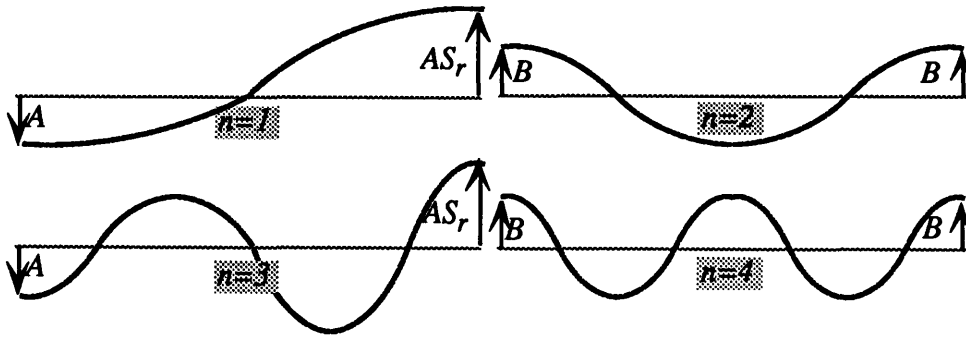
Figure 3.10 First four pressure eigenfunctions for the TRR.

The constants A and B are found by noting that these functions have to be orthonormal. This means the volume integral of the product of one mode p_n with itself is

$$\langle p_n | p_n \rangle = \int p_n p_n dV = 1,$$

and the volume integral of the product of one mode p_n and some other mode p_m is

$$\langle p_n | p_m \rangle = \int p_n p_m dV = 0,$$

where $n \neq m$, and V is the volume of the TRR. To find A, compute $\langle \mathbf{p}_1 | \mathbf{p}_1 \rangle = \int \mathbf{p}_1^2 dV = 1$ using $dV = S dx$, where $S = S_1$ for $-L \leq x \leq 0$ and $S = S_2$ for $0 \leq x \leq L$:

$$\int \mathbf{p}_1^2 dV = \int_{-L}^{0} S_1 p_{l1}^2 dx + \int_{0}^{L} S_2 p_{r1}^2 dx \quad \rightarrow \quad A = \sqrt{\frac{2}{S_1 L (1 + S_r)}}. \tag{3.23}$$

B is found using $\langle \mathbf{p}_2 | \mathbf{p}_2 \rangle = \int \mathbf{p}_2^2 dV = 1$:

$$\int \mathbf{p}_2^2 dV = \int_{-L}^{0} S_1 p_{l2}^2 dx + \int_{0}^{L} S_2 p_{r2}^2 dx \quad \rightarrow \quad B = \sqrt{\frac{2}{L(S_1 + S_2)}}. \tag{3.24}$$

Finally, the orthonormal set of eigenfunctions is written as

$$|m_{odd}\rangle = \sqrt{\frac{2}{S_r L(1 + S_r)}} \cdot \begin{cases} \sin(k_n x) & -L \leq x \leq 0 \\ S_r \sin(k_n x) & 0 < x \leq L \end{cases}$$

$$|m_{even}\rangle = \sqrt{\frac{2}{L(S_1 + S_2)}} \cdot \cos(k_n x) \qquad -L \leq x \leq L \tag{3.25}$$

where k_n has been defined in Eq. 3.21. The k_n's determine the calculated resonant frequencies:

$$k_n = \frac{\omega_{n,calc}}{c_0} \quad \rightarrow \quad \omega_{n,calc} = k_n c_0. \tag{3.26}$$

Because the exact value of k_n is critical in calculating the generated harmonics' magnitudes, the computational model will use empirical values of k_n by measuring the actual resonant frequencies ω_n. The sound speed will be assumed constant at all times, calculated as

$$c_0 = \sqrt{\gamma R T_0},$$

where γ is the ratio of specific heats of the fluid, R is the gas constant, and T_0 is the starting temperature.

3.2.2 Input Forcing Function Modeled

The modeling of the forcing functions (piston motions) is presented in this section. When the TRR is vibrated by a shaker, Fig. 3.8b shows that there are effectively three

pistons acting on the fluid inside. The three pistons can be treated as 'mass' generators[3] located at $x=-L$, 0, and L. In terms of G, the mass rate per volume, the forcing function F_{dr} is the sum of three Dirac delta functions:

$$F_{dr} = \frac{\partial G}{\partial t} \quad G: \begin{cases} G_{-L} = \rho_0 u_{dr}(t)\delta(x+L) \\ G_0 = -\rho_0 u_{dr}(t)\delta(x) \\ G_L = -\rho_0 u_{dr}(t)\delta(x-L) \end{cases}, \tag{3.27}$$

where ρ_0 is the ambient density of the fluid, and $u_{dr}(t)$ is the velocity function of the pistons, and δ is the Dirac delta function. The forcing function can be written as the product of its time and spatial components:

$$F_{dr} = F_{dr}(t) \cdot F_{dr}(x). \tag{3.28}$$

Since the piston velocity function is the only time dependent variable, and a common factor of G ($u_{dr}(t)$ is the same for all pistons in the experimental apparatus) then the separated components of F_{dr} are

$$F_{dr}(t) = \frac{du_{dr}(t)}{dt} = \dot{u}_{dr}(t), \qquad F_{dr}(x) = \rho_0[\delta(x+L) - \delta(x) - \delta(x-L)]. \tag{3.29}$$

The forcing frequency information is in the time-dependent component $F_{dr}(t)$ and is simply the acceleration function $\dot{u}_{dr}(t)$ of the pistons. Introduction of actual acceleration functions into the equations developed thus far requires special care. When only one driving frequency ω_{dr}, equal to the fundamental resonant frequency ω_1 of the resonator, is present in the acceleration function, say

$$F_{dr}(t) = \dot{u}_{dr}(t) = F_1 \sin(\omega_{dr}t),$$

then the entire forcing function can be used directly in finding the first-order perturbation solution $|p^{(1)}\rangle$ (Eq. 2.20). The higher-order perturbation solutions are then found from the information already known (Eqs. 2.21-2.23). When a second driving frequency is introduced to quench the second harmonic generated by the quadratic nonlinear coupling effects, the acceleration function will look like

---

[3] L. E. Kinsler, et. al., *Fundamentals of Acoustics*, 120 (1982).

$$F_{dr}(t) = \dot{u}_{dr}(t) = \underbrace{F_1 \sin(\omega_{dr} t)}_{F_{drI}} + \underbrace{F_2 \sin(2\omega_{dr} t + \phi_2)}_{F_{drII}}.$$

In this case, the total forcing function must be separated into two terms, F_{drI} and F_{drII}, to find the first and second-order perturbation solutions, as discussed in Section 3.1 (Eqs. 3.3-3.4). Similarly, when a third tone is introduced to quench the third harmonic generated by the cubic nonlinear coupling effects, the total forcing function needs to be separated into three terms. Each term then contributes to each of the first three-order perturbation solutions (Eqs. 3.3, 3.4, and 3.8).

$$F_{dr}(t) = \dot{u}_{dr}(t) = \underbrace{F_1 \sin(\omega_{dr} t)}_{F_{drI}} + \underbrace{F_2 \sin(2\omega_{dr} t + \phi_2)}_{F_{drII}} + \underbrace{F_3 \sin(3\omega_{dr} t + \phi_3)}_{F_{drIII}}.$$

3.2.3 Variables in the Computational Model

The discussions to this point have concentrated on formulating expressions for the perturbation solutions $p^{(n)}$. The first three order perturbation solutions $p^{(1)}$, $p^{(2)}$ and $p^{(3)}$ are to a first approximation also the frequency solutions p_1, p_2, and p_3. (see Section 3.1). Since the objective is to quench nonlinearly generated harmonics, the computational model will not be set up to compute for harmonics higher than p_3. One reason is that once quenching of the lower harmonics is attained, previous discussions have shown that higher harmonics cannot prevail and will thus be quenched as well. Another reason is that the computations for higher harmonics are too complex and time-consuming.

The computational modeling was performed on an IBM-compatible Pentium 75 Mhz computer from Micron Computers, Inc. The software used is *Maple V* (Release 3), a system for doing mathematics by computer. Maple was used in the thesis to symbolically generate the resonator response equations and then to produce real-valued results by substituting variables with actual values. The following discussion will formulate equations for ε_{quad}, F_2, and ϕ_2, the variables needed to *generate* as well as to *quench* the second harmonic. Although not shown here, variables for quenching the third harmonic may be formulated in a similar fashion.

54

3.2.3 (a) The Effective Quadratic Coupling Coefficient

The generation of harmonics via quadratic nonlinear coupling effects depends on the quantity ε_{quad}, which was assumed constant and shall be derived here for its explicit form. The *magnitude* of ε_{quad} will be shown to require empirical values of the first two frequency terms at $x=L$, $p_1(L)$ and $p_2(L)$, when driven by only one tone. To begin the analysis, recall the second-order perturbation solution, Eq. 2.21:

$$\left|p^{(2)}\right\rangle = -\sum_{m=1}^{\infty} \frac{\langle m|F_{dr2}\rangle}{\left(\hat{k}^2-k_m^2\right)}|m\rangle; \quad \left|F_{dr2}\right\rangle = \varepsilon_{quad}\left|p^{(1)}\right\rangle * \left|p^{(1)}\right\rangle.$$

When a single forcing tone is present, $F_{dr}(x,t) = F_{dr}(x)\cdot F_1\sin(\omega_{dr}t)$, with the drive frequency ω_{dr} equal to the fundamental resonant frequency ω_1 of the resonator, the frequency convolution $\left|p^{(1)}\right\rangle * \left|p^{(1)}\right\rangle$ yields two terms, one is of 0 frequency and the other of frequency $2\omega_{dr}$, the second harmonic. $F_{dr}(x)$ is the spatial component of $F_{dr}(x,t)$, shown in Eq. 3.29, and $F_1\sin(\omega_{dr}t)$ is the time component of $F_{dr}(x,t)$. Removing the 0 frequency term (see Section 2.2.1) then results in the following for $\left|p^{(2)}\right\rangle$, which is now approximated as $|p_2\rangle$:

$$\left|p^{(2)}\right\rangle = |p_2\rangle = -\frac{\langle 2|F_{dr2}(2\omega_{dr})\rangle}{\left(\hat{k}_2^2-k_2^2\right)}|2\rangle; \qquad \left|F_{dr2}(2\omega_{dr})\right\rangle = \varepsilon_{quad}\left|p^{(1)}\right\rangle * \left|p^{(1)}\right\rangle, \qquad (3.30)$$

where $\hat{k}_2^2$ and k_2^2 have been defined in Eqs. 3.11-12.

The first-order response $p^{(1)}=p_1$ is assumed the form:

$$p_1(x,t) = p_{1a}f_1(x)\sin(\omega_{dr}t), \qquad (3.31)$$

where p_{1a} is an effective amplitude of the response and $f_1(x)$ is the first eigenfunction, $|1\rangle$. The nonlinearly generated second harmonic is a function of $2\omega_{dr}$ and is assumed the form:

$$p_2(x,t) = p_{2a}f_2(x)\sin(2\omega_{dr}t+\theta_2), \qquad (3.32)$$

where p_{2a} is the amplitude, $f_2(x)$ is the second eigenfunction $|2\rangle$, and θ_2 is a phase offset. The effective forcing function on $p_2(x,t)$ is proportional to the square of $p_1(x,t)$:

$$F_{dr2}(x,t) = \varepsilon_{quad}p_1^2(x,t) = \varepsilon_{quad}p_{1a}^2 f_1^2(x)\sin^2(\omega_{dr}t). \qquad (3.33)$$

Using the trigonometric identity $\sin^2(\omega_{dr}t) = \frac{1}{2}[1 - \cos(2\omega_{dr}t)]$ and keeping only the $2\omega_{dr}$ term results in

$$F_{dr2}(x,t) = -\tfrac{1}{2}\varepsilon_{quad}p_{1a}^2 f_1^2(x)\cos(2\omega_{dr}t).$$ (3.34)

In determining the value of ε_{quad}, the temporal components are neglected when Eqs. 3.32 and 3.34 are substituted into Eq. 3.30:

$$|p_{2a}f_2(x)| = \left| \frac{-\tfrac{1}{2}\varepsilon_{quad}p_{1a}^2 \langle f_2(x)f_1^2(x)\rangle}{\left(\hat{k}_2^2 - k_2^2\right)} f_2(x) \right|,$$ (3.35)

where $\langle f_2(x)f_1^2(x)\rangle$ is the volume integral of the product of $f_1^2(x)$ and $f_2(x)$, and $|\,|$ means *the amplitude of*. Since all experimental measurements will be made at $x=L$ (right-end of resonator, Fig. 3.8), the value of p_{2a} is determined by using Eq. 3.32, noting that the magnitude of p_2 at $x=L$ is $p_2(L)=|p_{2a}f_2(L)|$. The magnitude of p_1 at $x=L$ is $p_1(L)=|p_{1a}f_1(L)|$. $p_1(L)$ and $p_2(L)$ are to be measured experimentally, thus the values for p_{1a} and p_{2a} are

$$p_{1a} = \frac{|p_1(L)|}{|f_1(L)|}; \qquad p_{2a} = \frac{|p_2(L)|}{|f_2(L)|}.$$ (3.36)

Evaluating Eq. 3.35 at $x=L$ with Eq. 3.36 and solving for ε_{quad} results in

$$\varepsilon_{quad} = \left| \frac{2p_2(L)f_1^2(L)\left(\hat{k}_2^2 - k_2^2\right)}{p_1^2(L)f_2(L)\langle f_2(x)f_1^2(x)\rangle} \right|.$$ (3.37)

The dependence of ε_{quad} on the quantity $\left(\hat{k}_2^2 - k_2^2\right)$, a complex number, would seemingly violate the assuming made in Chapter 2 that ε_{quad} is a real number. However, ε_{quad} is calculated in Eq. 3.37 to depend on the *magnitude* of $\left(\hat{k}_2^2 - k_2^2\right)$, a real number, thus ε_{quad} is *real*. The information inherent (phase) in the imaginary portion of $\left(\hat{k}_2^2 - k_2^2\right)$ is not really lost when ε_{quad} is used to calculate the nonlinearly excited second harmonic because the quantity $\left(\hat{k}_2^2 - k_2^2\right)$ is present in both the numerator and denominator of Eq. 3.30, and is

thus irrelevant in calculating the second harmonic. The same cannot be said for calculations of higher harmonics.

With ε_{quad}, the magnitudes of nonlinearly generated harmonics can now be predicted computationally. More importantly, the analysis can now be extended to include a second forcing function, $F_{drII}(x,t) = F_{2x}F_2 \sin(2\omega_{dr}t + \phi_2)$, to quench the nonlinearly generated second harmonic. F_{2x} is the spatial dependent component of F_{drII} and is equal to $F_{dr}(x)$, since for the resonator used, all forcing functions are physically applied at the same locations (Eq. 3.29).

3.2.3 (b) Second Forcing Tone Amplitude and Phase

This section will formulate expressions for F_2 and ϕ_2, the amplitude and phase of the second forcing tone, respectively, necessary to quench nonlinear effects when only quadratic nonlinear coupling is considered. In Section 3.2.1, Eq. 3.15 was established as the criterion for quenching the nonlinearly generated second harmonic. This equation shows that quenching occurs when the two volume integrals are equal in magnitude but opposite in sign:

$$\langle 2|F_{drII}\rangle = -\langle 2|F_{dr2}\rangle, \tag{3.38}$$

where $F_{drII} = F_2 F_{2x} \sin(2\omega_{dr}t + \phi_2)$, $F_{dr2} = F_{dr2x}F_{dr2t} = \varepsilon_{quad}(p^{(1)})^2$, $p^{(1)} = p_1$ is the fundamental harmonic response, F_{dr2x} and F_{dr2t} are the spatial and time component of F_{dr2}, respectively, $|2\rangle = f_2(x)$ is the second eigenfunction, and ε_{quad} is a real constant determined in the preceding discussion. The unknown variables are F_2 and ϕ_2, which are now found.

The inverse Fourier transform of Eq. 3.38 results in The analysis is commenced by transforming Eq. 3.38 to time space. The equation will not be affected because the volume integrals, $\langle 2|F_{drII}\rangle$ and $\langle 2|F_{dr2}\rangle$, are spatial:

$$\int f_2(x)F_{drII}dV = -\int f_2(x)F_{dr2}dV. \tag{3.39}$$

If the time components are factored out, and noting that the fundamental response p_1 to the first driving tone $F_{dr}(t) = F_1 \sin(\omega_{dr}t)$ will behave as $\cos(\omega_{dr}t)$, then Eq. 3.39 is rewritten as

$$\sin(2\omega_{dr}t+\phi_2)\int f_2(x)F_2F_{2x}dV = -\cos^2(\omega_{dr}t)\int f_2(x)F_{dr2x}dV. \qquad (3.40)$$

Expanding $\cos^2(\omega_{dr}t)$ and retaining just the time-dependent term $(2\omega_{dr}t)$ results in

$$\sin(2\omega_{dr}t+\phi_2)\int f_2(x)F_2F_{2x}dV = -\cos(2\omega_{dr}t)\int \tfrac{1}{2}f_2(x)F_{dr2x}dV. \qquad (3.41)$$

Assuming the volume integrals will be equal in amplitude and sign when computed (if the sign is opposite, simply change the sign of ϕ_2), then looking at just the time-dependent terms, ϕ_2 can be calculated as

$$\begin{aligned}\sin(2\omega_{dr}t+\phi_2) &= -\cos(2\omega_{dr}t)\\ \phi_2 &= -90° \, or \, 270°\end{aligned} \qquad (3.42)$$

F_2 is now determined by concentrating on just the volume integral portions of Eq. 3.41. F_2 is a constant and can be taken out of the integral, resulting in

$$F_2 = \frac{\int \tfrac{1}{2}f_2(x)F_{dr2x}dV}{\int f_2(x)F_{2x}dV}. \qquad (3.43)$$

Eq. 3.43 predicts the amplitude of the second forcing tone necessary to quench the second harmonic, given some amplitude F_1 on the first tone. If F_1 is too large, having just a second forcing tone to quench the second harmonic may be insufficient in quenching all nonlinearly generated harmonics, and a third tone is needed, $F_{drlll} = F_3F_{3x}\sin(3\omega_{dr}t+\phi_3)$, to quench the third harmonic generated by cubic nonlinear coupling effects. Although not shown here, the values of F_3 and ϕ_3 may be determined in a similar fashion to the above.

3.3 Experimental Setup of Concept

This section will now discuss the experimental setup used in demonstrating the active control approach. The first part of this section will present the setup in simple block-diagram form. The feasibility of the proposed setup is then discussed and the actual experimental setup presented. Equipment of particular importance will be looked at and finally, concerns and problems encountered in matching experimental to computational results are discussed.

3.3.1 Active Control Loop Devised

Given the chosen TRR harmonic resonator and a forcing function that drives the standing waves with the fundamental resonant frequency, nonlinear effects will generate harmonics p_2, p_3, and so on to yield in a total pressure waveform of $p=p_1+p_2+p_3+...$, where p_1 is the fundamental/linear response to the forcing function. The previous sections have shown that harmonics can be quenched by using additional forcing tones. A simple active control loop is shown in Fig. 3.11, this will serve as the starting point in devising the actual setup to be constructed.
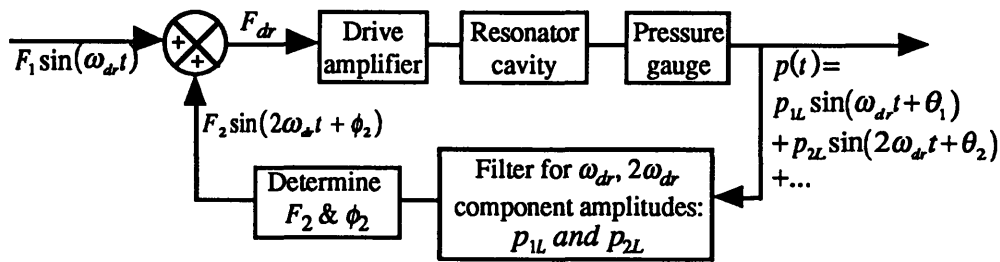

Figure 3.11 Simple active control loop to eliminate the second harmonic.
The total acoustic pressure $p(t)$ is filtered for the first two frequency component amplitudes, p_{1L} and p_{2L}, which are used to calculate ε_{quad} and then a starting value of F_2. The actual value of F_2 and ϕ_2 are controlled manually, to compensate for experimental and computational differences.

Before analyzing the loop, the fact that only *one* set of pressure measurements will be taken, at $x=L$, should be reiterated. Being able to quench the nonlinearly generated harmonics at this location implies that the rest of the resonator is also quenched of the harmonics. This is because the frequency (time) dependent component of the acoustic waves can be treated separately from the spatial dependent component,

$$p = p_1(t)p_1(x) + p_2(t)p_2(x) + p_3(t)p_3(x)+... \ .$$

Clearly, when $p_2(t)$ is quenched at one location, it is quenched everywhere else, provided $p_2(x)\neq0$ at that location. Thus, from here on, the symbols p_1, p_2, p_3, etc. will be understood to be just the time portions of the harmonics evaluated at $x=L$: $p_1 = p_1(t)$, $p_2 = p_2(t)$, $p_3 = p_3(t)$, etc.

Fig. 3.11 shows how an active control loop might be assembled to quench the second harmonic. Quenching the third harmonic will only require minor modifications to

the loop and will be discussed briefly later. Now, the control loop to quench the second harmonic can be explained as follows.

A controller first generates a single tone forcing function (at the resonator's fundamental frequency, $\omega_{dr}=\omega_1$), which is amplified by the vibrator setup and applied to the resonator cavity. The pressure signal at $x=L$ is detected with a pressure gauge and then filtered to retain the amplitudes of the fundamental harmonic p_{1L}, and the amplitude of the second harmonic p_{2L}, generated from nonlinear effects. From this information, the amplitude of a second forcing tone is calculated and added to the original forcing function. The phase has already been determined to be $\phi_2=-90°$, see Section 3.2.3(b). Finally, the revised forcing function is amplified and applied to the resonator. The resulting pressure signal should then be free of all nonlinearly generated harmonics, assuming no cubic nonlinear coupling effects are present.

The above description of the basic setup has assumed that information such as the resonant frequencies ω_n's and quality factors Q_n's of the resonator are already known and unchanging. Also, this simple setup has assumed that the experimental equipment to be used can be controlled precisely to produce the desired results. For example, the drive amplifier is assumed to only amplify the forcing function and not introduce a phase difference. In designing this setup with actual equipment, all of these assumptions must be questioned and necessary steps taken to either accept them or to devise safeguards against possible problems. With the precautions in mind, the actual setup is now shown in modular form in Fig. 3.12.
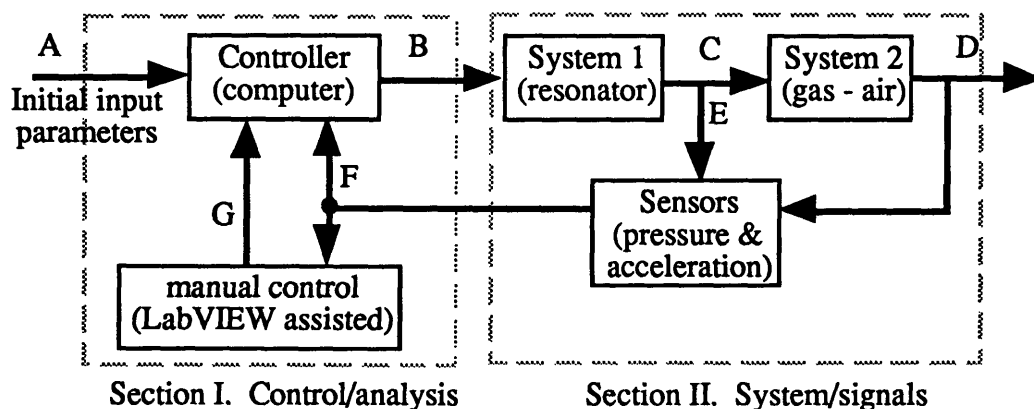

Figure 3.12 Actual setup in modular form.

The setup is divided into two main sections. In section I, a computer and a software package (LabVIEW) are utilized to generate the forcing functions (B) that will be supplied to the shaker/resonator setup, given initial input parameters specified by the user (A). The pressure and acceleration signals (F) from the system are then analyzed by the same software package as well as by several lock-in-amplifiers. One part of the information (F) is used to automatically make changes to the forcing function, while another part is processed by the user and manual changes (G) made to the forcing function.

In section II, the overall system is separated into two systems; the first is the resonator shell and the second is the fluid inside the shell. The acceleration amplitude of the resonator shell is measured, providing information on the actual forcing amplitude (C) applied to the fluid inside. This information (F) is sent back to section I to compare with the desired forcing function (B) in terms of amplitude and phase, so that any differences here can be compensated for in the computational model. Finally, the acoustic pressure (D) at the end cap of the TRR is measured with a pressure transducer and transferred to section I where it (F) is analyzed for the amplitudes of the harmonics.

3.3.2 Processes and Equipment in Experimental Setup

The experimental setup is shown in Fig. 3.13, it is comprised of about twenty major pieces of hardware and one major software package (LabVIEW). A schematics of the setup is shown in Fig. 3.14, following the modular form shown in Fig. 3.12. Two major processes of the control loop are now discussed followed by a brief description of the major components of the setup.

3.3.2 (a) Process 1: Generation of the Forcing Function

To generate the forcing function on the acoustic waves, the forcing function signal must proceed through the equivalent of eight transfer functions (Fig. 3.15). Each transfer function, K_1 through K_8, will alter the desired signal in terms of a gain difference or a phase offset.

1. Computer - Gateway 2000 P5-60
2. Data Acquisition Board - NI ATM-MIO-16E-2
3. Data Acquisition Board - NI Lab PC+
4. Computer - Micron P75
5. Data acquisition Board - NI ATM-MIO-16F-5
6. Oscilloscope - Tektronix 475
7. Attenuator - resistors setup
8. Signal filter - Krohn-Hite 3202
9. LDS Power Amplifier
10. LDS Field Generator
11. LDS 722 Vibrator
12. Resonator
13. Pressure transducer - Endevco 8510C
14. Pressure indicator - Endevco 4428A
15. Charge accelerometer - PCB J357B01
16. LDS Sine controller (used as acceleration indicator)
17. Pre-amp for pressure - PAR 113
18. Pre-amp for acceleration - PAR 113
19. Lock-in-amplifier 1 - EG&G 124A
20. Lock-in-amplifier 2 - EG&G 124A
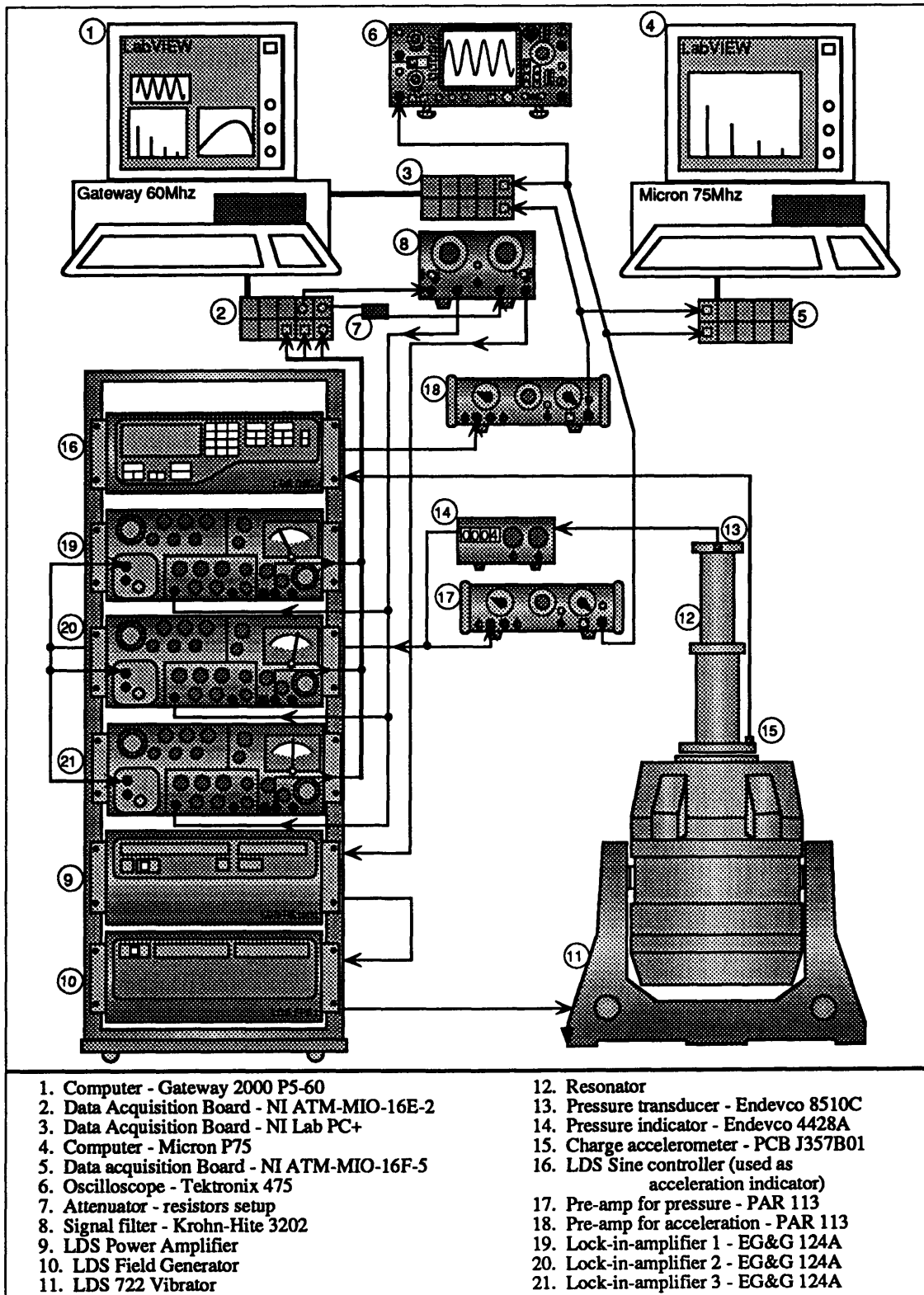21. Lock-in-amplifier 3 - EG&G 124A
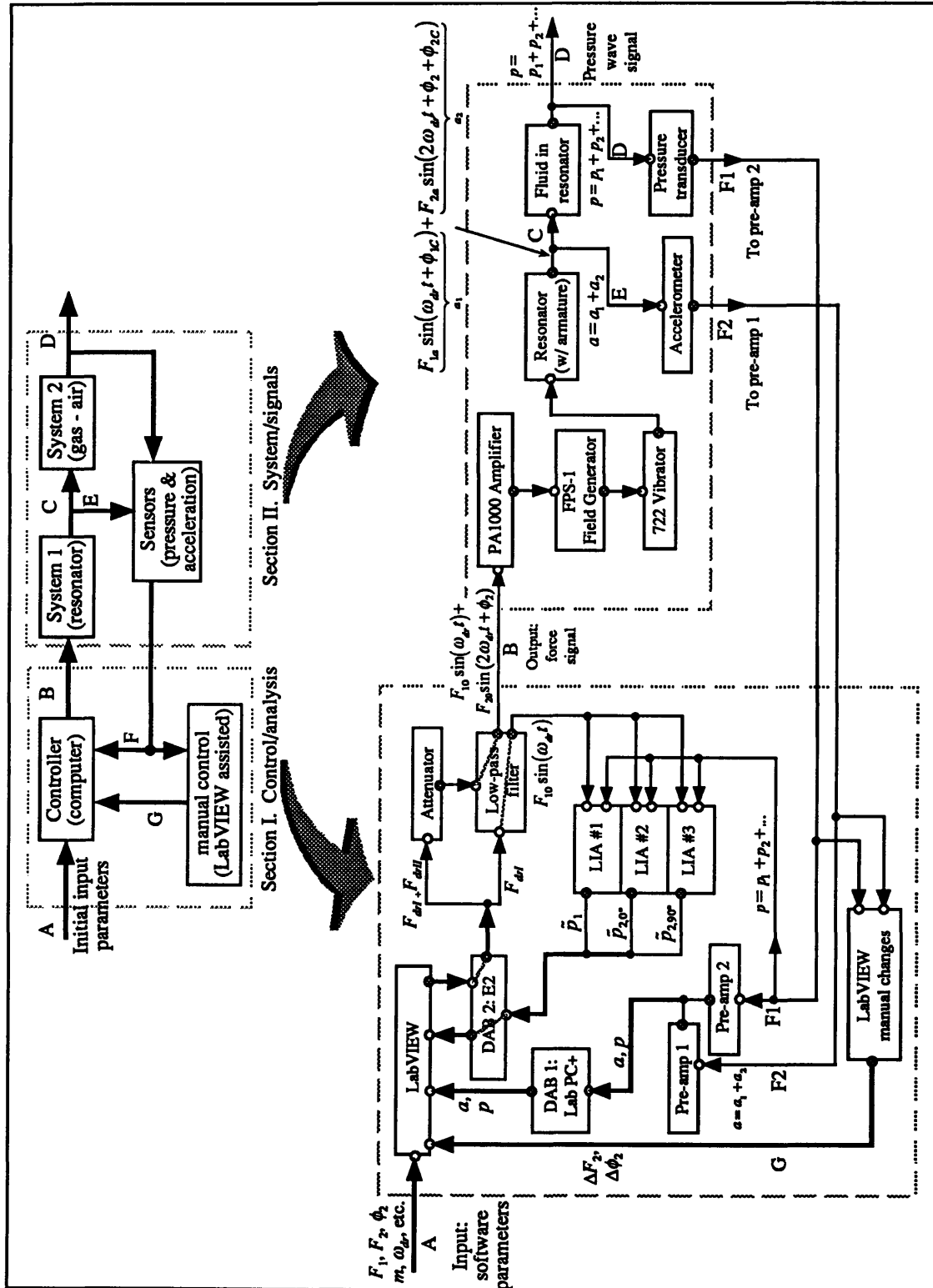
Figure 3.13 Experimental setup.

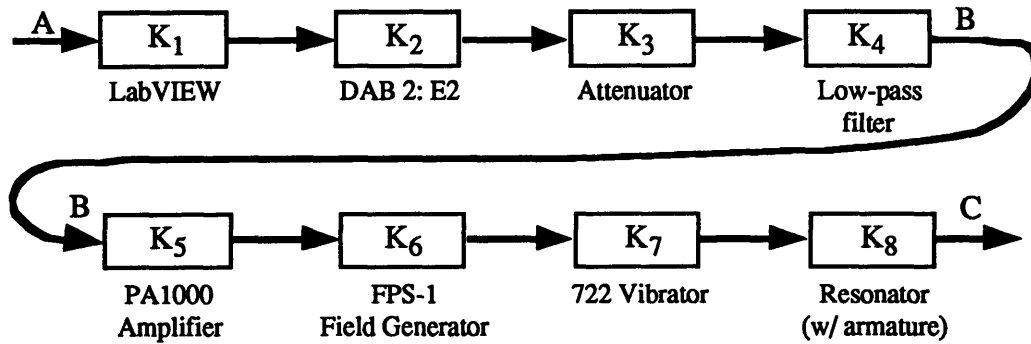*Figure 3.14 Experimental setup - schematics.*

63

Figure 3.15 Path for the forcing function signal.

The user first specifies the desired values of the forcing function (A) into the computer software (National Instruments LabVIEW). Two essential variables that the user will need to enter are the driving frequency ω_d, and the amplitudes of the desired forcing function F_1, F_2, and F_3. Since the software will be generating digital signals, the user will also need to specify variables such as the update rate and the resolution of the signals. The update rate is the number of points generated per second, and the resolution is the number of points, or steps, per cycle of waveform generated. The (time) resolution must be kept as high as possible to approximate a smooth waveform. The amplitude of the waveform must be converted from a force (g's) to a voltage via the gain K_1.

Once the digital waveform is generated, it must be converted to an analog signal using a digital-to-analog (DAC) converter. In this setup, a data acquisition board (DAB) from National Instruments was used: ATM-MIO-16E2, referred to as E2 in Fig. 3.15. The E2 has built-in digital-analog as well as analog-digital (ADC) converters, allowing analog input and output. The converters have fixed (amplitude) resolutions (12 bits, ±5 V Full Scale output, 2.44 mV/step) which limit the signal amplitude resolution. For example, if a high resolution (Δt small) digital signal has a peak-to-peak amplitude of only 15 mV, then when it is converted to an analog signal with a 12-bit converter, the resulting waveform is very coarse, having just six steps between the maximum and minimum points (Fig. 3.16). The resolution is fixed at 2.44 mV per step, thus to increase the smoothness of the analog signal, the initial digital signal amplitude is made as large as possible. The preceding condition helps in part to determine the magnitude of K_1. The gain K_2 is assumed to be one (1); the conversion from digital to analog will not alter the amplitude nor the phase of the signal if the amplitude is initially large ($>>2.44$ mV).
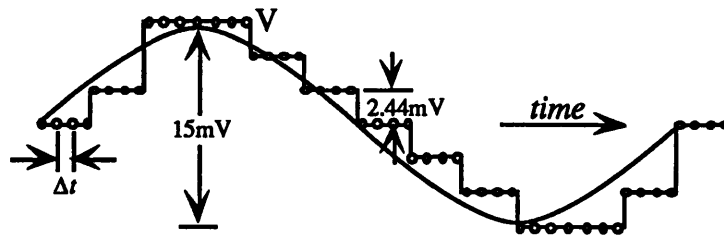
Figure 3.16 Digital signal converted to analog signal with a DAC.

The vibrator amplifier (PA1000) does not accept an incoming voltage signal (B) of amplitude greater than 1 V_{rms}, therefore, the high amplitude signal emanating from the DAB must be attenuated by K_3 so that when the signal is amplified by K_5 through K_8, the desired forcing function is generated. The low-pass filter (Krohn-Hite 3202) is used to smooth out the analog signal by filtering out the high-frequency steps and can be adjusted so the amplitude and phase offsets are negligible, thus K_4 is assumed the value one (1) with zero phase offset.

When the signal (B) reaches the vibrator setup (PA1000 to 722 Vibrator in Fig. 3.15), the three transfer functions, K_5, K_6, and K_7, combine to amplify and convert the voltage signal into a forcing function on the resonator. The resonator is mounted directly onto the armature of the vibrator, thus K_8 includes the information on the dynamics of the armature-resonator combination. The amplitude and phase response of the resonator-vibrator armature assembly is frequency dependent. This was measured using an accelerometer mounted at the base of the resonator. The deviations measured will determine the necessary modifications to the computational model to maintain consistency between theory and experiment. Finally, the mass of the air inside the resonator is assumed negligible compared to the resonator/armature mass, therefore, the forcing function on the fluid is assumed to be unaffected by the gas dynamics. The process by which the forcing function is summarized in Fig. 3.17.
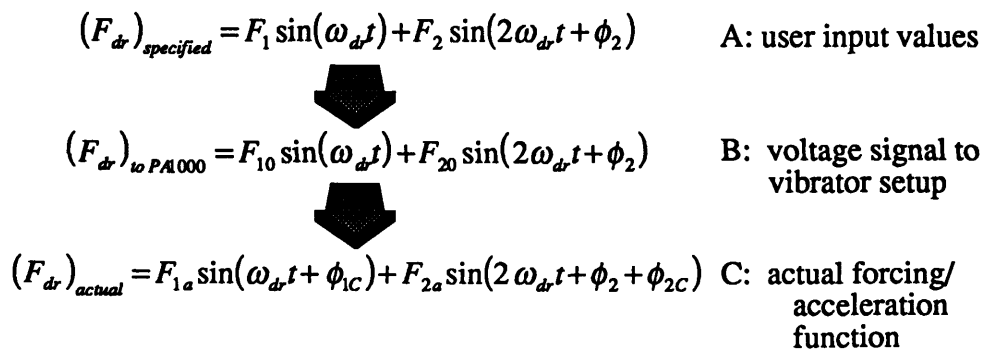
$$\left(F_{dr}\right)_{specified} = F_1 \sin\left(\omega_{dr}t\right) + F_2 \sin\left(2\omega_{dr}t + \phi_2\right)$$ A: user input values

$$\left(F_{dr}\right)_{to\,PA1000} = F_{10} \sin\left(\omega_{dr}t\right) + F_{20} \sin\left(2\omega_{dr}t + \phi_2\right)$$ B: voltage signal to vibrator setup

$$\left(F_{dr}\right)_{actual} = F_{1a} \sin\left(\omega_{dr}t + \phi_{1C}\right) + F_{2a} \sin\left(2\omega_{dr}t + \phi_2 + \phi_{2C}\right)$$ C: actual forcing/ acceleration function

Figure 3.17 Generation of the forcing function.

In the above figure, F_{1a} and F_{2a} are the actual forcing function amplitudes. These values must be compared with the user input values, F_1 and F_2, and appropriate actions taken to either keep F_{1a} and F_{2a} as the forcing amplitudes (in the computational model) or to change initial input values so that the desired amplitudes are the result. Thus, if the desired amplitude of F_1 is 1.5 g, but measurements show the actual amplitude to be only 1.2 g (a reduction factor of $1.2g/1.5g = 0.8$), then the initial value of F_1 should be increased to $1.5g/0.8 = 1.875g$. Similarly, the transfer functions K_5, K_6, K_7, and K_8 may have introduced phase offsets, ϕ_{1C} and ϕ_{2C}, which must also be included in the computational model as correction factors. Actual measurements of F_{1a}/F_1, F_{2a}/F_2, ϕ_{1C}, and ϕ_{2C} will be presented in Section 3.3.3.

3.3.2 (b) Process 2: Quenching the Second Harmonic

To quench the second harmonic, the pressure signal p is first be analyzed for the magnitudes of its frequency components p_n's. The pressure is measured with a pressure transducer (Endevco 8510C), shown in Fig. 3.18, and amplified (pre-amplifier PAR 113) before it is converted from an analog to a digital waveform by another data acquisition board (Lab PC+). The digital signal is processed by the same LabVIEW software which generates the forcing function signal. The LabVIEW VI (virtual instrument - object oriented program written for the experiment) uses an amplitude-spectrum analysis routine on the pressure signal, breaking down the pressure into its frequency components. The amplitude of the second harmonic p_2 is then used to determine any changes necessary to F_2 and ϕ_2: ΔF_2 and $\Delta \phi_2$. The changes are currently performed manually (to LabVIEW) because the computer processing capacity had been reached and further data processing was not feasible.

In order to quench the second harmonic, the discussions so far have assumed that the first forcing tone frequency ω_{dr} is always equal to the fundamental resonant frequency ω_1. The fundamental resonant frequency is not a constant and fluctuates with temperature. The forcing tone frequency has to be changed accordingly, to keep it equal to the changing fundamental resonant frequency. A lock-in-amplifier (LIA #1) was used to track ω_1 and a loop was set up to change ω_{dr} to match ω_1.
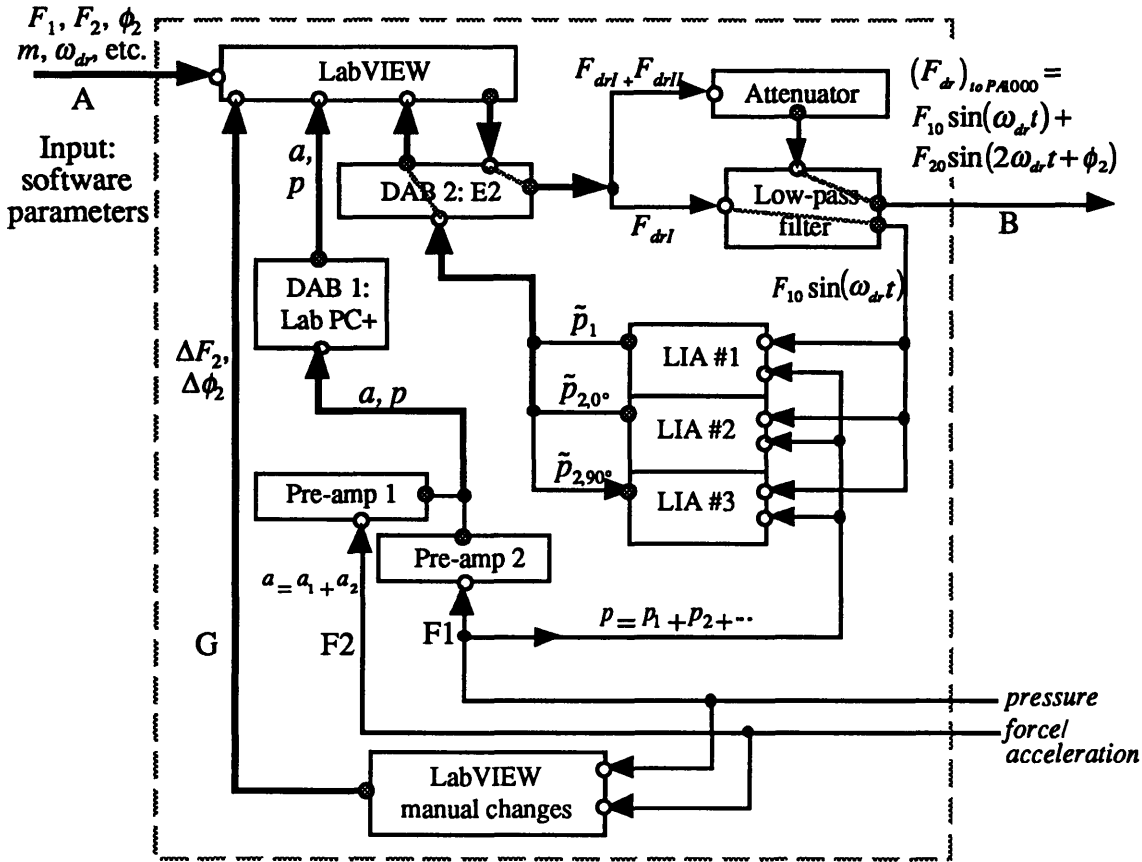
Figure 3.18 Section I of active control loop: Control/analysis.

The ingredients needed to track and match the fundamental resonant frequency are: a reference signal with which the actual pressure signal can be compared with to determine the resonant frequency, the pressure signal, and a routine in the LabVIEW VI that processes the LIA output and adjusts the driving frequency ω_{dr}. The reference signal is shown in Fig. 3.18 as F_{drl}, the fundamental forcing signal generated by LabVIEW. The pressure signal is a voltage waveform directly from the pressure transducer. The LIA compares the phases and amplitudes of the reference and pressure signal, and generates a DC output $\tilde{p}_1$. This output is set to zero at the initial resonant frequency ω_1. When ω_1 starts to drift, $\tilde{p}_1$ will become nonzero. The LabVIEW routine then calculates an updated driving frequency ω_{dr} to push $\tilde{p}_1$ to zero again. The routine was written with proportional control so that the correction frequency, $\Delta\omega_{dr}$, is equal to a constant K_{LIA} times the LIA output $\tilde{p}_1$: $\Delta\omega_{dr} = K_{LIA}\tilde{p}_1$. Thus, when $\tilde{p}_1$ is zero, then the correction frequency $\Delta\omega_{dr}$ is zero as well, and the driving frequency ω_{dr} is exactly equal to the fundamental resonant frequency ω_1.

3.3.2 (c) Resonator / LabVIEW Description

The main objective in this section is to introduce the resonator design, calculate the expected resonant frequencies $\omega_{n,calc}$, and to describe briefly how the software LabVIEW was used to control and analyze the force and pressure signals.

The TRR body consists of five sections, all made of aluminum 6061 (Fig. 3.19). The topmost section, **A**, is one of the two end-caps. At the exact center of the plate, a threaded thruhole is machined. The pressure transducer is flush mounted against the inside surface of the top end-cap. Another cavity is machined one inch off the center of the end-cap. In this cavity is a valve where the gas is to be extracted or exchanged. The opening of the cavity into the inside of the resonator was kept as small as possible to avoid disturbing the main flow dynamics.

The two tubes, **B** and **D**, are both of thickness 0.125". and have diameters 2.75" and 3.75", respectively. The area ratio is thus $S_r = 3.75^2/2.75^2 = 1.86$. The overall length of the resonator was decided to be $2L$=0.6 meter, or about 23.62". While the lower tube **D** is of length L, the upper tube **B** is slightly shorter, with the remaining length provided by the transition plate **C**. Note that the location where the radius should have abruptly changed has been smoothed to mitigate turbulence and other effects which may alter the expected behavior of the gas significantly. In experiments, the second resonant frequency was found to be slightly higher than two times the fundamental: $\omega_2=(2+\Delta)\omega_1$, $\Delta\approx0.02$. Whether the deviation was the result of smoothing the corner is unclear, however, this deviation can be easily included in the computational model. The other end-cap, **E**, has been machined with eight thruholes through which 3/8-24 UNF screws will secure the resonator to the armature of the vibrator.

Given the geometry of the resonator, from Eqs. 3.21 and 3.26, the resonant frequencies in Hertz, are calculated as

$$f_{n,calc} = \frac{\omega_{n,calc}}{2\pi} = \frac{n}{4L}c_0,$$ (3.44)

where n=1, 2, 3, ... , and c_0 is the speed of sound $c_0 = \sqrt{\gamma R T_0}$.

A. *Top plate* - 4" outer diameter; includes gas input valve and pressure transducer.

B. *Upper cavity* - 3.00" outer diameter, 2.75" inner. Length is 11.41" (289.8mm)

C. *Transition plate* - 5.00" outer diameter; connects upper and lower cavities.

D. *Lower cavity* - 4.00" outer diameter, 3.75" inner. Length is 11.81" (300mm)

E. *Lower plate* - 7.09" outer diameter; includes 8 thruholes for 3/8-24 UNF screws
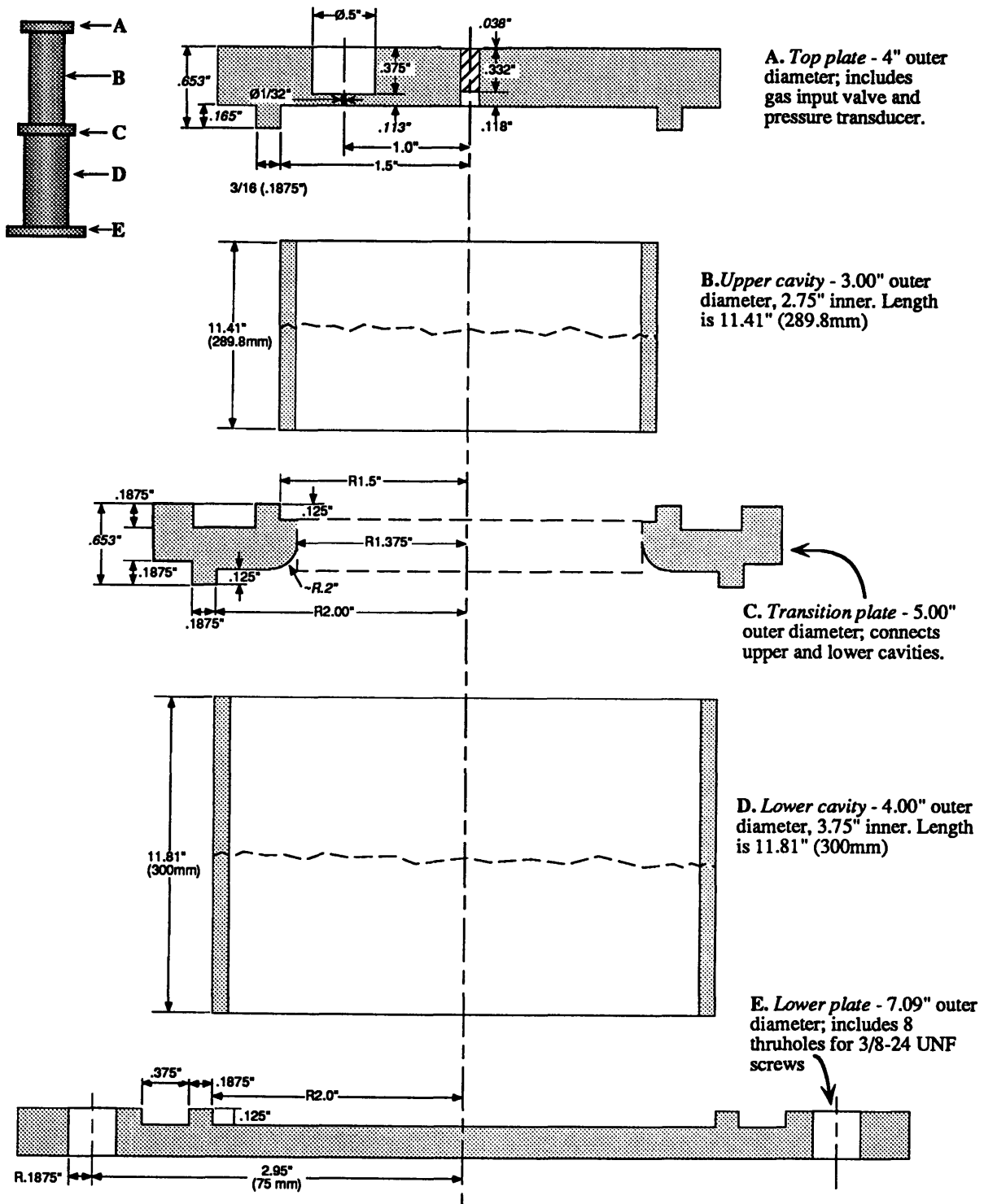
Figure 3.19 Resonator design.

69

Using air at ambient temperature (T_0=296 K), R=287 J/kgK, γ=1.4, the first three resonant frequencies are: $f_{1,calc} = 287.39 Hz$, $f_{2,calc} = 574.78 Hz$, and $f_{3,calc} = 862.17 Hz$. These values are purely theoretical and can only be used as starting points in the experiments. Actual resonant frequencies will need to be experimentally determined and the information incorporated into the computational model.

LabVIEW is a *graphical* programming system for data acquisition, control, analysis, and display. The programs created are called virtual instruments, or VI's, that can be assembled to create a more complex system. For example, a VI was written to continuously generate the forcing function signals. Another VI was written to acquire the pressure signals and to analyze them. Each of these VI's in turn may be composed of other VI's, and so on (Fig. 3.20).
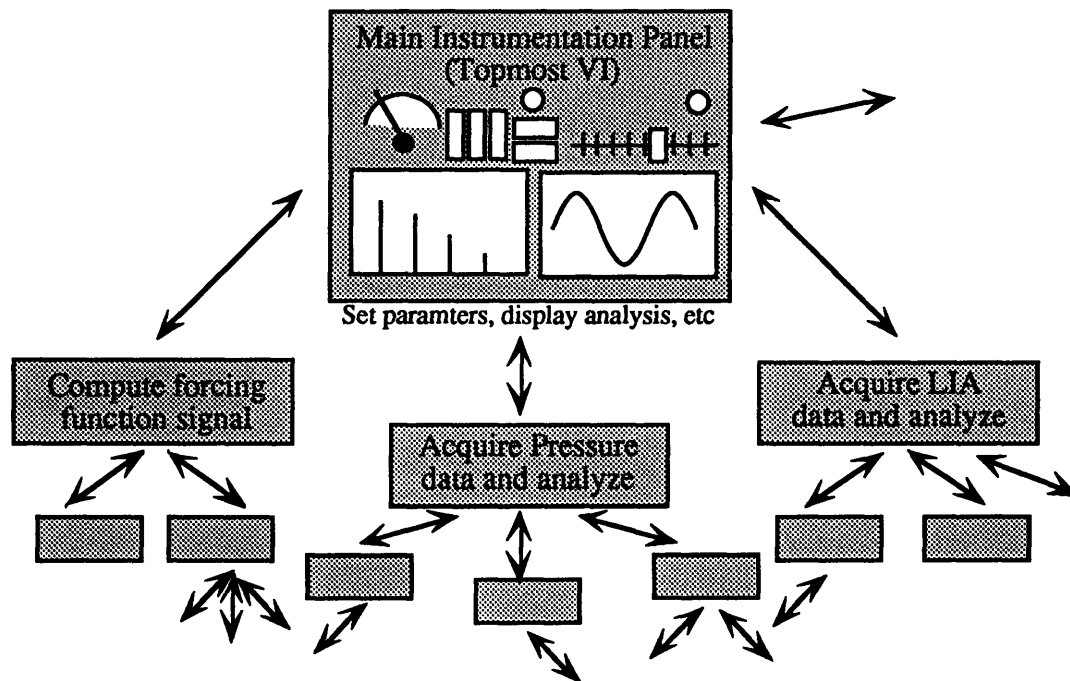

Figure 3.20 LabVIEW VI structure.
Each box is a VI and is connected to the topmost VI in some order, like a subroutine or sub-program in a text-based computer program.

In the topmost VI, the user inputs values for variables such as the starting forcing frequency, the forcing amplitudes, range of the amplitude-spectrum, update rate of the

signals, etc. These variables are then sent to the various VI's that are responsible for specific tasks. In tracking the fundamental resonant frequency, one VI acquires and analyzes the LIA data, the VI then signals another VI that generates the forcing function to execute a change to the frequency information. The time interval between changes is kept by another VI, and so on. In this way, a loop is created that constantly checks fluctuations to the resonant frequency and initiates the necessary changes to track the resonance.

3.3.3 Concerns with the Active Control Loop

There are two main concerns with the active control loop presented, both have already been discussed briefly in Section 3.3.2. The first concern is the drifting of the fundamental resonant frequency when quenching the second harmonic. The drifting will affect the experimental results for reasons discussed in Section 3.3.2(c). To address this concern, a control loop using a lock-in-amplifier and a routine in LabVIEW was developed. The loop tracks the fundamental resonance and adjusts the driving frequency accordingly. However, the drifting is not a phenomenon that needs to be included in the computational model because the two frequencies can be forced equal at all times.

The second concern does affect the computational model, and is associated with using the model to predict the quenching forcing amplitude F_2 and phase ϕ_2. As discussed, the actual values of F_2 and ϕ_2 will deviate from the initially assigned values as the forcing function signal progresses from the computer to the resonator. The deviations can be determined experimentally by analyzing the ratio of the amplitudes and the phase difference of the forcing function signals at the resonator base and after the low-pass filter (C and B in Fig. 3.15). A VI was designed for the purpose of measuring the deviations and functions as follows. With one forcing tone of constant amplitude, its frequency is swept from 50 Hz to 1000 Hz. This forcing function signal, once applied to the vibrator setup, undergoes changes in responding to the resonator/armature dynamics. The altered forcing function is then compared with the initial function from the computer for amplitude and phase deviations. This process is repeated for several forcing function amplitudes to determine if the deviations are amplitude dependent. The results are shown in Figs. 3.21 and 3.22.
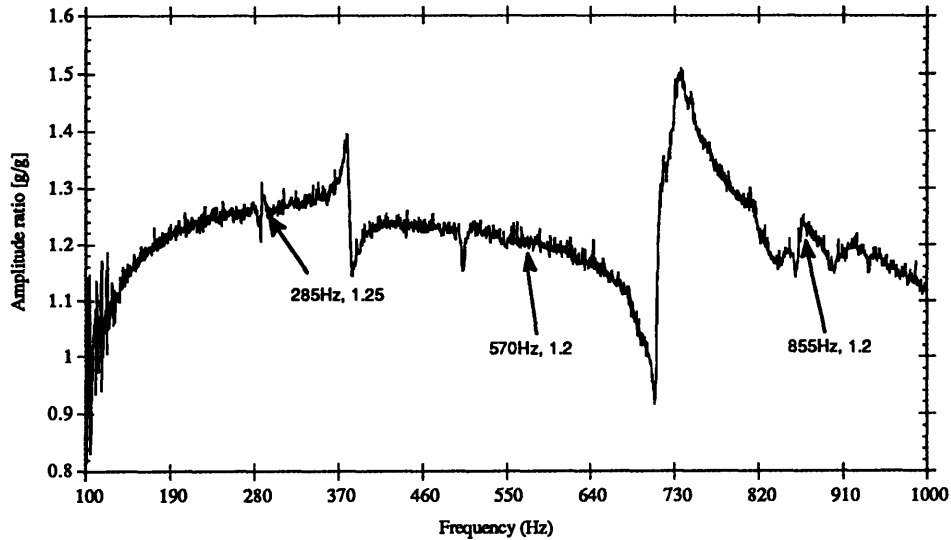
71

Figure 3.21 Amplitude ratio of actual acceleration to specified forcing function.
The specified forcing amplitude is 1.5 g, data points are 1 Hz apart. The amplitude ratio is indicative of the frequency response of the vibrator and shaker setup. Near the three resonant frequencies, the amplitude ratios are all about 1.2.
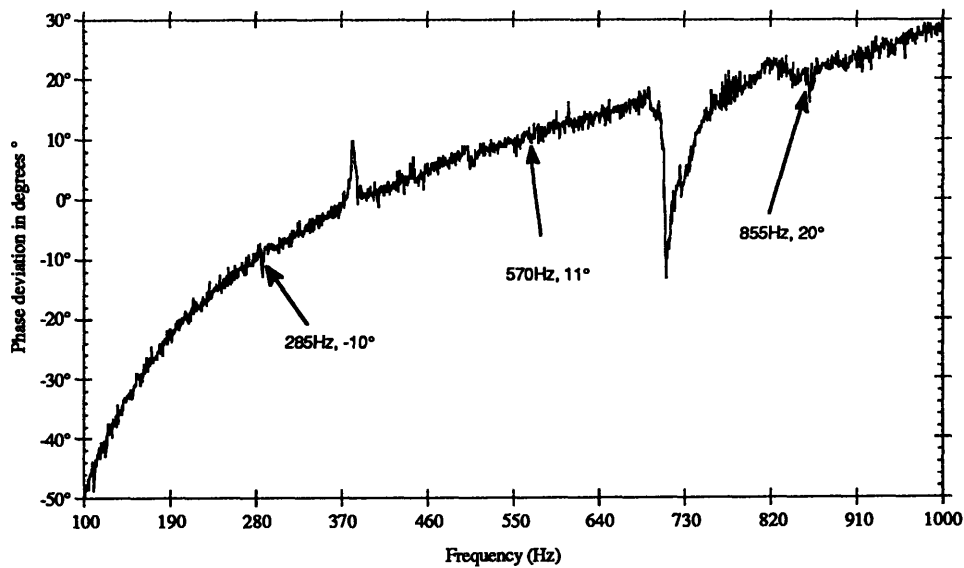

Figure 3.22 Phase deviation of actual acceleration to specified forcing function.
The specified forcing amplitude is 1.5 g, data points are 1 Hz apart. At a driving frequency near 700 Hz, the vibrator and shaker setup experiences a resonance.

Fig. 3.21 shows the amplitude ratio of the two measured signals as a function of the driving frequency. The ratio is $g_{actual} \div g_{specified}$, where g_{actual} is the actual forcing amplitude in g's on the resonator, and $g_{specified}$ is the user-specified forcing amplitude, also in g's. The figure shows the amplitude response of the resonator/armature setup and is quite complicated in some frequency ranges. At the frequencies of interest, i.e. the first three resonant frequencies, the ratios have values of about 1.25, 1.2, and 1.2, respectively. The frequency step size used in measuring the amplitude response was very rough at 1 Hz, thus the amplitude ratio values in Fig. 3.21 fluctuated quickly from one point to the next. To determine the ratio values more accurately, the frequency step size was reduced to 0.05 Hz in the vicinity of the resonances. The resulting, more exact, amplitude ratio values (at the first four resonances) are presented in the first section of Chapter 4. These amplitude ratio values are correction factors and will be used to adjust the experimental results when comparing with the computational results. For example, if a *specified* forcing amplitude of 1 g produced a 1200 Pa pressure amplitude, but the *actual* forcing amplitude was measured at 1.2 g, then the forcing amplitude used in the computational model should also be 1.2 g

The phase deviation is shown in Fig. 3.21. The phase offset of the actual forcing function relative to the specified forcing function is shown as a function of the driving frequency. From the figure, the actual signal lags behind the specified signal at the fundamental resonant frequency but leads the specified signal at the next two resonant frequencies. The values of the deviations are approximately -10°, 11°, and 20°, respectively, for the first three resonances. The same results were found when the forcing amplitude was changed to a low of 0.5 g and a high of 3.5 g. In the computational model, therefore, these phase deviations must be incorporated by subtracting them from the forcing functions. Thus, the first and second forcing tones would be changed as shown:

$$F_{dr}(t) = F_1 \sin(\omega_{dr} t) + F_2 \sin(2\omega_{dr} t + \phi_2)$$
$$\downarrow$$
$$F_{dr}(t) = F_1 \sin(\omega_{dr} t + 10°) + F_2 \sin(2\omega_{dr} t + \phi_2 - 11°). \tag{3.45}$$

The experimental and computational results are discussed next in Chapter 4.

Chapter 4 Experimental and Computational Results

T he results will be presented in three sections in this chapter. The first section presents the preliminary empirical information that must be determined to allow calculation of ε_{quad}, F_2, and ϕ_2. This includes the resonant frequencies f_n's, the quality factors Q_n's, and the amplitudes of the fundamental and second harmonic, p_{1L} and p_{2L}, measured experimentally at the fundamental resonant frequency.

The second section presents the experimental and computational results for a setup where only one forcing tone, $F_{dr}(t) = F_1 \sin(\omega_{dr} t)$, is imposed on the resonator. In the first part of this section, the forcing tone amplitude F_1 is fixed while the forcing frequency ω_{dr} is swept through each of the first four resonant frequencies, ω_1 to ω_4. In the second part, the forcing frequency is kept at the resonant frequencies while the forcing amplitude F_1 is varied.

In the last section, the experimental and computational pressure harmonics are shown and compared as additional forcing tones are imposed to quench the quadratic and cubic nonlinear effects. In addition to quenching the second and third harmonics, other combinations of interest will also be presented. These other combinations may be useful in probing coupling effects among the harmonics.

4.1 Preliminary Empirical Information

4.1.1 Measurement of ω_n's and Q_n's, p_{1L} and p_{2L}

Two virtual instruments (VIs) were constructed with LabVIEW to collect the data required for determining f_n's, Q_n's, and ε_{quad}. The first VI generated a forcing function of

constant amplitude but allowed the user to adjust the frequency. As the frequency was swept from below to above the nth resonance, the amplitude of the nth mode response was measured. Another part of the VI then determined the quality factor Q_n and resonant frequency f_n from the amplitude responses to the frequency sweep through the nth resonance. The frequency sweep rate was set at 0.05 Hz per second, thus each sweep took one to two minutes, depending on the frequency range swept. During this time, the temperature of the air in the resonator rose due to the continuous power supplied to the resonator by the vibrations.

An upper bound in the frequency deviation due to rising temperatures was found by driving the resonator continuously locked onto the resonant frequency and observing the value of the resonant frequency as a function of time. As shown in Fig. 4.1, the value of the fundamental resonant frequency increased by less than 0.1 Hz over a period of 240 seconds. Since a typical frequency sweep time in determining f_1 and Q_1 was about 100 seconds, the fundamental frequency increase should therefore not exceed more than 0.05 Hz from the beginning to the end of the sweep. Similar levels of error on resonant frequencies were found for sweeps through the second, third, and fourth resonances.

These levels of frequency deviations decrease the actual values of the Q_n's by only one to two percent, thus to a first approximation, the measured Q_n's will be used in the computational model. Each set of resonant frequencies varied from one day to the next, depending on the room temperature. In any particular day, however, the frequency
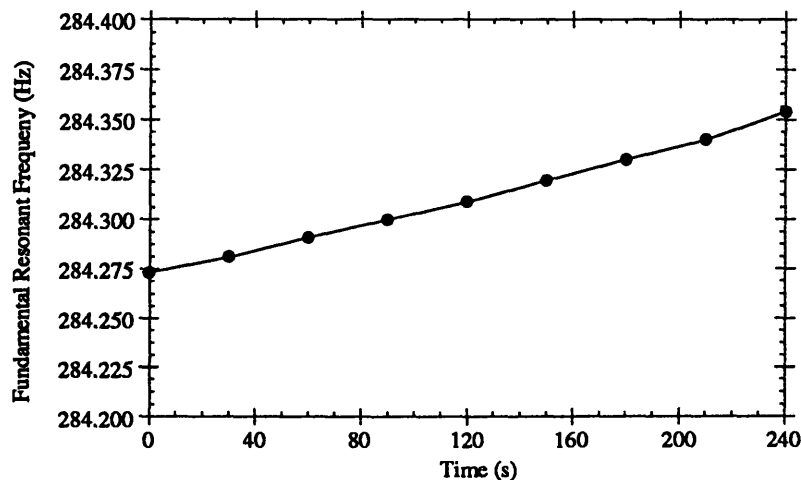

Figure 4.1 Fundamental resonant frequency increases slowly with time.

deviations due to the heating of the medium by the vibrations are small enough so that ratios of the nth resonant frequency to the fundamental resonant frequency could be measured with good accuracy. These ratios should be independent of day-to-day room temperature variations and were incorporated into the computational model by applying the ratios to the wave numbers k_n's. In theory, the k_n's are perfect integral multiples of the fundamental: $k_n = nk_1$, where n is an integer. However, to be able to compare computational with experimental results, the actual values of the multiples must be used:

$$k_n = n_r k_1, \qquad (4.1)$$

where n_r is the measured ratio of the nth resonant frequency to the fundamental resonant frequency. Although the computed resonant frequencies will no doubt be different from actual resonant frequencies because of some assumptions made in the model, the ratios of the resonant frequencies will be the same. The importance of the ratios will be discussed shortly.

Figs. 4.2 to 4.5 show the amplitudes of the harmonic responses to sweeps through the first four resonant frequencies. In each figure, the measured acceleration and pressure amplitude are graphed as a function of the driving force frequency. The two symbols and the connecting curves represent data points which are 0.05 Hz apart. For simplicity, all forcing amplitudes will from hereon be designated in terms of acceleration, in g's. The gas in the resonator is air at room temperature and pressure - about 298 K and 101.3 kPa, respectively. The estimated values of the resonant frequencies and the quality factors are summarized in Table 4.1.
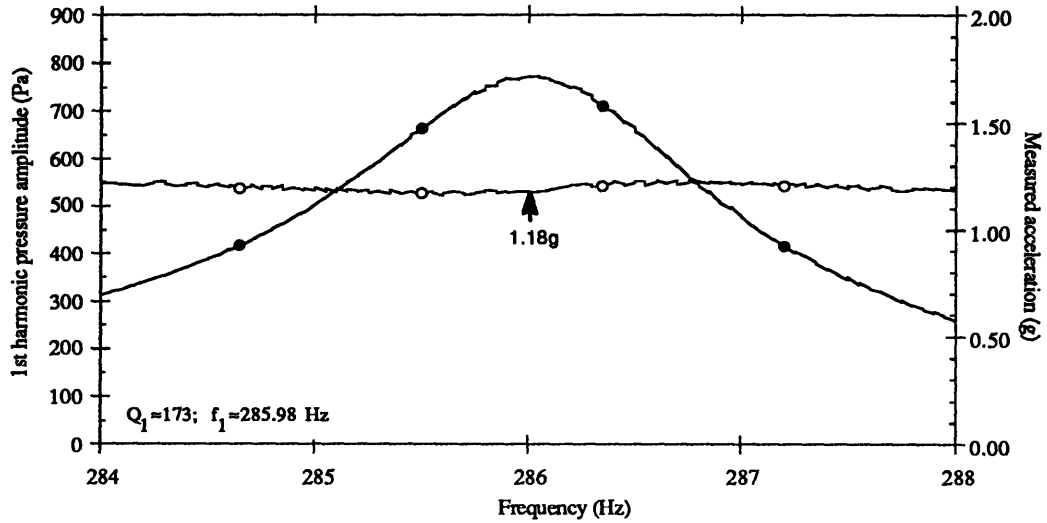
Figure 4.2 Amplitude response through the fundamental resonance.
Specified force $F_1 = 1.0$ g, amplitude at the fundamental resonant frequency is $p_1 = 773$ Pa, resonant frequency $f_1 = 285.98$ Hz, $Q_1 = 173$. ━●━: pressure response amplitude through the first resonance, left scale, ━○━: measured acceleration, right scale. The symbols and the connecting curves represent actual data points which are 0.05 Hz apart.
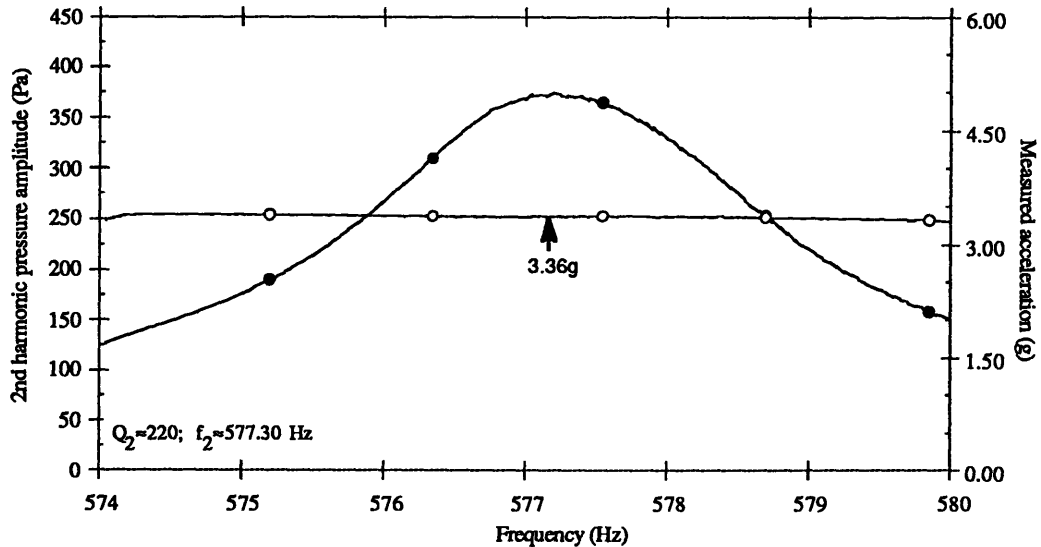

Figure 4.3 Amplitude response through the second resonance.
Specified force $F_2 = 3.0$ g, amplitude at the second resonant frequency is $p_2 = 374$ Pa, resonant frequency $f_2 = 577.3$ Hz, $Q_2 = 220$, $f_2/f_1 = 2.02$. ━●━: pressure response amplitude through the second resonance, left scale, ━○━: measured acceleration, right scale. The symbols and the connecting curves represent actual data points which are 0.05 Hz apart.
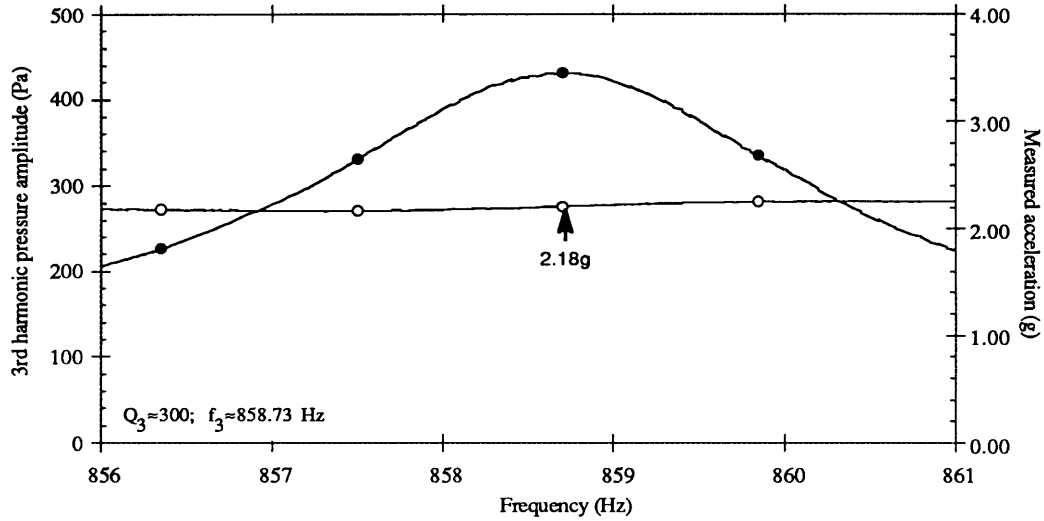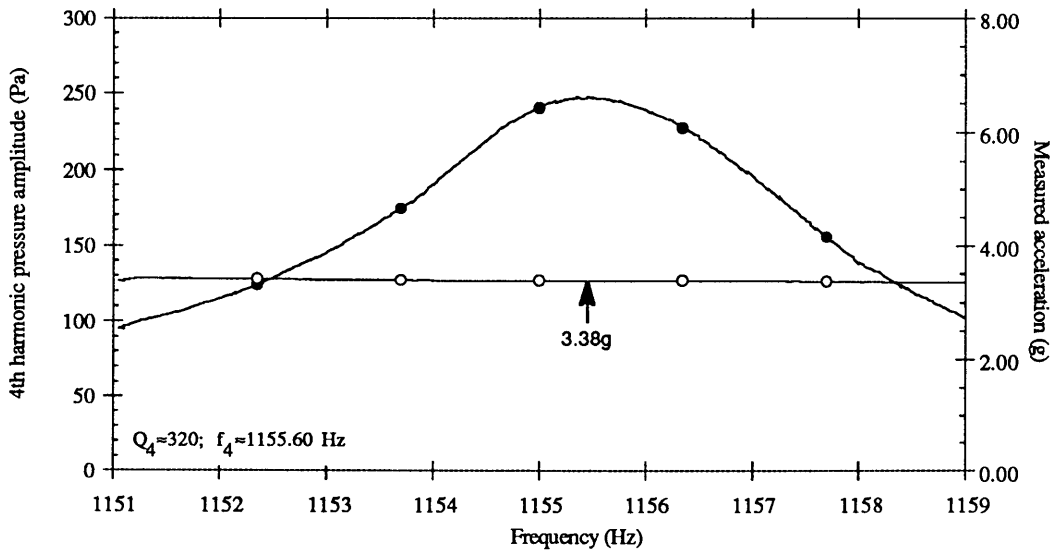
Figure 4.4 Amplitude response through the third resonance.
Specified force F_3= 2.0 g, amplitude at the third resonant frequency is p_3= 431 Pa, resonant frequency f_3= 858.73 Hz, Q_3 = 300, f_3/f_1= 3.00. —●—: pressure response amplitude through the third resonance, left scale, —○—: measured acceleration, right scale. The symbols and the connecting curves represent actual data points which are 0.05 Hz apart.

Figure 4.5 Amplitude response through the fourth resonance.
Specified force F_4= 4.0 g, amplitude at the fourth resonant frequency is p_4= 240 Pa, resonant frequency f_4= 1155.60 Hz, Q_4 = 320, f_4/f_1= 4.04. —●—: pressure response amplitude through the fourth resonance, left scale, —○—: measured acceleration, right scale. The symbols and the connecting curves represent actual data points which are 0.05 Hz apart.

79

	n	Specified force (g) $g_{n,specified}$	Actual force (g) $g_{n,actual}$	Pressure amp. at resonance (Pa) P_n (at f_n)	Resonant frequency (Hz) f_n	Quality factor Q_n	Ratio $n_r = f_n/f_1$
Fundamental resonance	1	1.00	1.18	773	285.98	173	1.00
Second resonance	2	3.00	3.36	374	577.30	220	2.02
Third resonance	3	2.00	2.18	431	858.73	300	3.00
Fourth resonance	4	4.00	3.38	248	1155.60	320	4.04

Table 4.1 The first four quality factors and resonant frequencies.

Table 4.1 includes the specified and actual forcing amplitudes in g's, and the corresponding peak response amplitudes at the resonances. For the fundamental response, the measured acceleration is about 18% higher than the specified value. For the next two resonances, the acceleration responses are also slightly higher than specified values, by about 12% and 9%, respectively. The measured acceleration is lower than specified, however, for the fourth resonance, by about 15%. From hereon, all experimental forcing amplitudes refer to *actual*, measured values in g's. The forcing amplitudes used in the computational model are these actual values. A direct comparison can thus be made between the experimental and computational responses.

Another important piece of information shown in Table 4.1 is the ratios of the resonant frequencies to the fundamental resonant frequency, n_r. For the first four resonances, the ratios of the frequencies show that the even modes are slightly higher in actual frequency values. The measured value of the second resonant frequency showed it to be about 1% higher than the calculated value, an increase of about 5.5 Hz. This was not the result of a temperature change, which would have required an increase of almost 6 K (the temperature was monitored to have been constant at 80°F during the actual experiment). Tests performed with other forcing amplitudes verified that the ratio $n_r=2.02$ for the second resonance is inherent to the resonator and not due to temperature fluctuations in the room. For the third resonance, the frequency ratio is 3.00, and the ratio is 4.04 for the fourth resonance, again resulting in a frequency of about 1% (or about 11.5 Hz) higher than the calculated value. These ratios are incorporated into the computational model by Eq. 4.1.

The values of the quality factors are higher for higher resonances. By Eq. 3.13, a higher Q_n means a larger response for the nth harmonic, *if* the difference in the nth harmonic driving frequency $n\omega_d$ and the nth resonant frequency $n_r\omega_1$ is very small. Thus, nonlinear

coupling to higher harmonics should become stronger and stronger, if the resonant frequencies of the resonator are integral multiples of the fundamental. If the resonant frequency ratios are far from integers, then the value of Q_n is less important. For the resonator (TRR) used in this research, the largest deviations of the resonant frequency ratios n_r's from integer values are for the even modes: 2.02 and 4.04 for the second and fourth modes, respectively. Thus, because of the high values for Q_2 and Q_4, the nonlinearly excited second and fourth harmonic responses will be weak since the frequencies of these harmonics do not overlap with the second and fourth resonant frequencies, i.e, when the n_r's are integers.

In past research efforts, the Q_n's and f_n's were measured in the linear acoustic regime, because when nonlinear effects become more significant in amplitude, the values of Q_n's and f_n's change. In Fig. 4.6, the pressure amplitude and quality factor of the first resonance are graphed as a function of the forcing amplitude F_1. Clearly the value of Q_1 decreases and the *rate of increase* of the pressure amplitude also decreases.
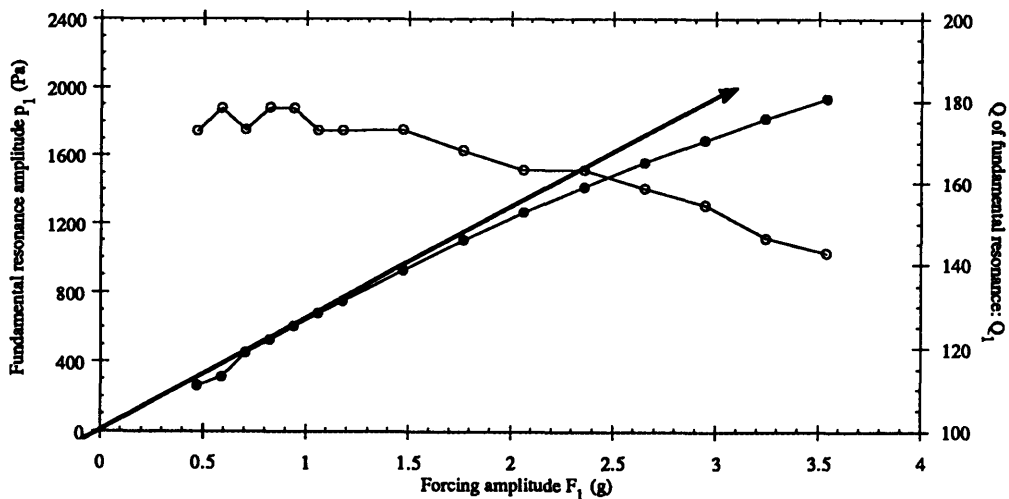

Figure 4.6 Fundamental harmonic response amplitude and quality factor of first resonance. The slope of the fundamental harmonic response amplitude (−●−, left scale) decreases, as well as the quality factor Q_1 (−○−, right scale) of the fundamental resonance, both nonlinearly due to emergence of nonlinear effects. The line with arrow shows how the pressure amplitude would increase in the absence of nonlinear effects.

At low forcing amplitudes, the amplitude of the pressure response is proportional to the forcing amplitude (F_1) imposed on the resonator. As nonlinear effects start to emerge, the pressure response amplitude at the fundamental resonance decreases because energy is now being extracted from the fundamental response to the second and higher-harmonics.

The decrease in Q_1 is clearly nonlinear and can be explained in part by the behavior of the first nonlinearly generated harmonic (the second harmonic), which for the quadratic nonlinear coupling case, is to grow as the *square* of the amplitude of the fundamental harmonic. The second nonlinearly generated harmonic (the third harmonic) grows as the *cube* of the fundamental harmonic. As the amplitudes of these harmonics increase with the forcing amplitude, Q_1 decreases faster and faster. The decrease in Q_1 decreases f_1, to be discussed shortly.

Before determining the values of the fundamental and second harmonic responses at the fundamental resonant frequency, the effect of the specified force on the pressure amplitudes at each of the first four resonances is now discussed (Fig. 4.7). The pressure amplitudes were calculated as one-half of the peak-to-peak value of the acquired pressure waveform. Thus, if nonlinear effects were present, they were assumed small so that the one-half of the peak-to-peak pressure waveform represented the dominant linear response at each resonance.

Fig. 4.7 shows that given the same forcing amplitude, the pressure response amplitudes are in the following descending order: fundamental resonance, third resonance, second resonance, and fourth resonance. When quenching nonlinear effects, the forcing amplitude of the tone required to quench the second harmonic can be *expected* to be much
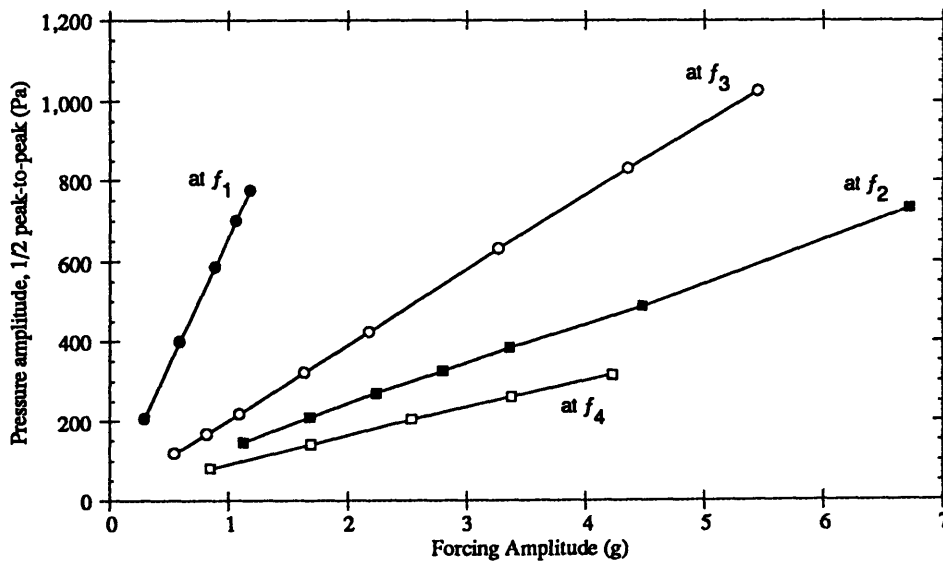

Figure 4.7 Experimental pressure response amplitudes at the first four resonances.
—●—: *Amplitude of the first resonance response,* —■—: *at the second resonance,* —O—: *at the third resonance, and,* —□—: *at the fourth resonance. Even modes respond weaker than odd modes.*

larger than the forcing amplitude of the tone to quench the third harmonic. There are two reasons for this: the second resonant frequency is not an exact integral multiple of the fundamental $n_r \neq 2$, thus the response to the forcing tone is small, and the second mode cannot be excited as easily as the fundamental or third mode in the TRR design, thus a much larger force is required to drive the second mode to an equivalent amplitude.

Using Eq. 3.37, the value of ε_{quad} was determined using empirical values of the fundamental and second harmonic response amplitudes when the resonator is driven at the fundamental resonant frequency. In the following discussions, the subscript "L" is used to designate the *amplitude* of the harmonic responses at the resonator's upper end-cap ($x=L$), ignoring the time-dependent components. Thus p_{1L} is the amplitude of the fundamental harmonic, p_{2L} is the amplitude of the second (nonlinearly generated) harmonic, and so on.

In Eq. 3.37, $p_1(L)=p_{1L}$ and $p_2(L)=p_{2L}$ at the fundamental resonant frequency f_1. The value of ε_{quad} is proportional to the ratio of p_{2L} to p_{1L}^2; assuming the other variables have already been determined and are constant.

$$\varepsilon_{quad} \propto \left(\frac{p_{2L}}{p_{1L}^2} \right)_{f_1} . \tag{4.2}$$

Thus, the essential information in determining ε_{quad} is not the absolute values of the first two harmonic responses, but rather the ratio as seen in Eq. 4.2. Since metric units were used in all analysis, the unit to ε_{quad}, consistent with Pascals (Pa) for the pressure amplitudes, was determined as $s^2/kg\cdot m$. To determine the ratio in Eq. 4.2, a second LabVIEW VI was constructed so that at a fixed forcing amplitude, the forcing frequency f_{dr} is swept from slightly below to slightly above the first resonance f_1 (Fig. 4.8), while maintaining a constant forcing amplitude. The pressure amplitudes p_{1L} and p_{2L} needed to determine ε_{quad} were measured when $f_{dr}=f_1$ (Fig. 4.8b).

The VI also acquired the amplitude of the third harmonic, p_{3L}, to show its growth behavior compared to that of p_{1L} and p_{2L}. The results to the frequency sweeps through the fundamental resonance at three specified forcing amplitudes, 0.35 g, 1.2 g, and 2.1 g, are shown in Figs. 4.9 to 4.11. The three harmonic amplitudes, when the forcing frequency is locked onto the fundamental resonant frequency, are graphed as a function of the forcing amplitude in Fig. 4.12.
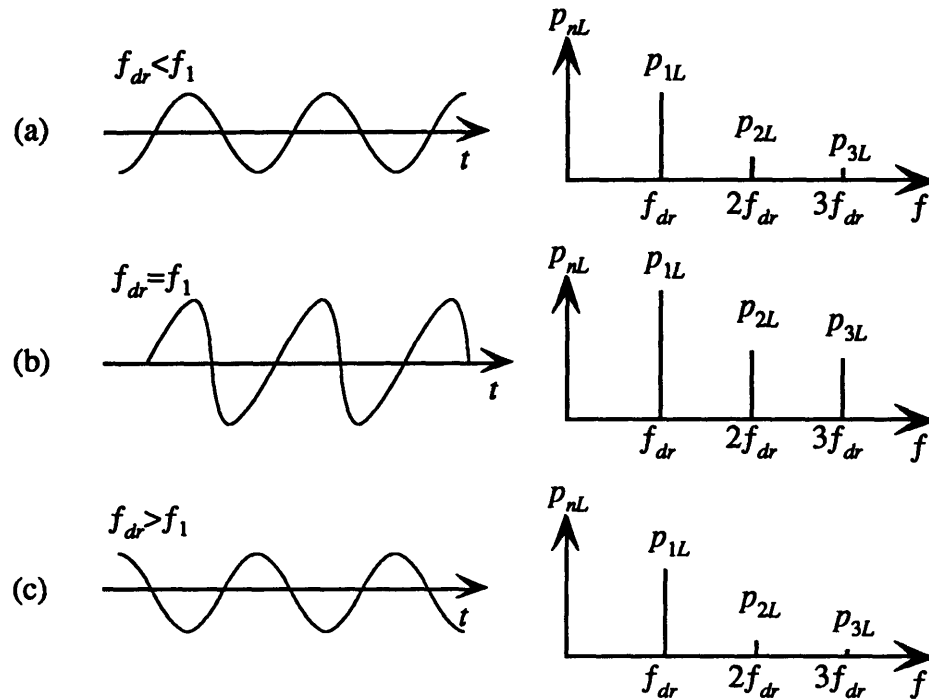
Figure 4.8 The pressure waveform and amplitude spectrum near the first resonance.
The driving frequency is increased from below (a) to above (c) the fundamental resonance, producing maximum nonlinear effects at the resonant frequency (b), where p_{1L} and p_{2L} are measured to determine ε_{quad}.

In Fig. 4.9, the forcing amplitude is low, at 0.35 g, and the resulting nonlinear effects is small. The second harmonic, the only nonlinearly generated harmonic, is still very small, with a peak amplitude of about 3 Pa which is only about 1.4% of the fundamental harmonic amplitude (210 Pa) at the fundamental resonant frequency. In Fig. 4.10, the forcing amplitude was increased to 1.2 g, resulting in a proportional increase in the fundamental harmonic, from 210 Pa to 700 Pa (3.33 times). However, the second harmonic amplitude has increased by more than 12 times (from 3 Pa to 36 Pa), and the third harmonic has risen to almost the same amplitude (from near 0 Pa to 33 Pa).
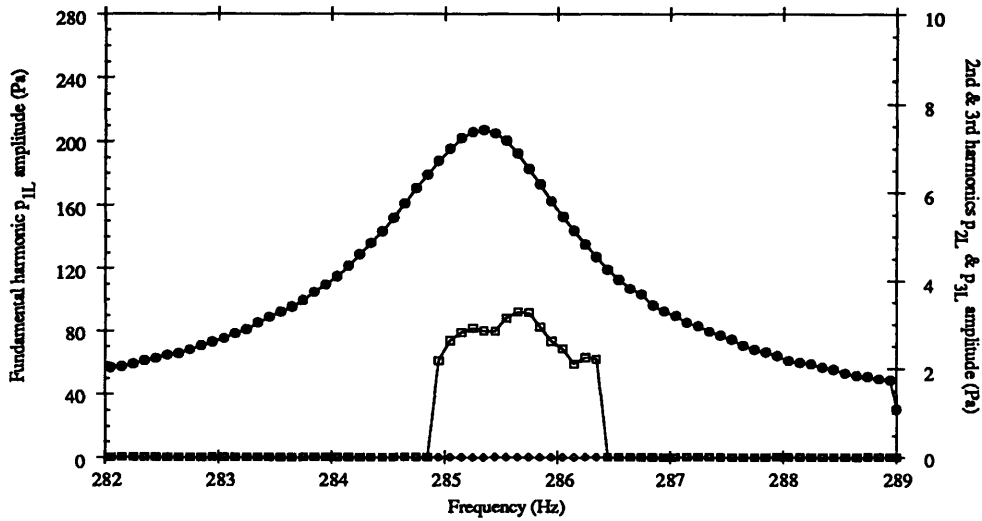
Figure 4.9 First three harmonic responses when driven near the fundamental resonance.
Forcing amplitude is $F_1=0.35$ g. The third harmonic (—◇—, right scale) is not yet evident, the second harmonic (—□—, right scale) is still small, with a maximum amplitude of about 3Pa, compared to 220Pa of the fundamental harmonic (—●—, left scale).
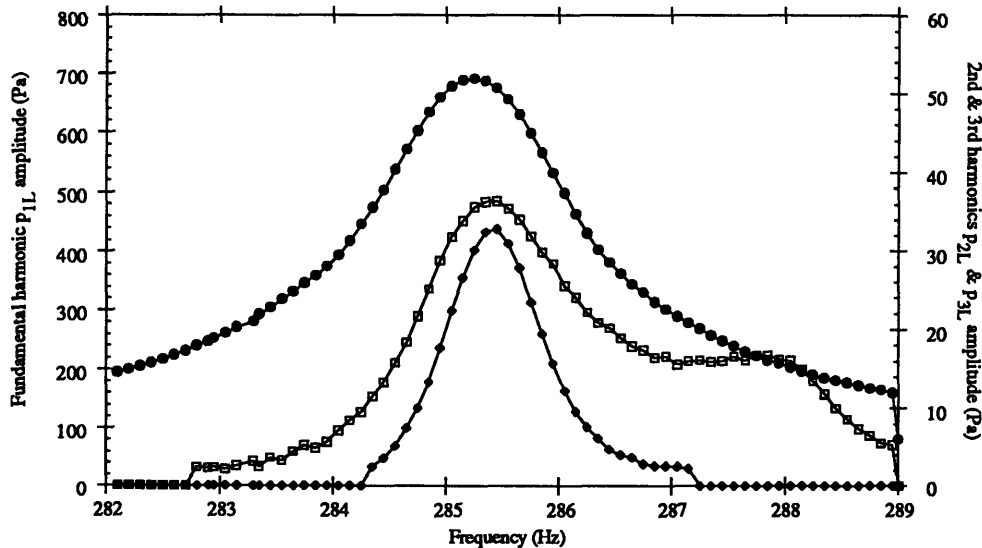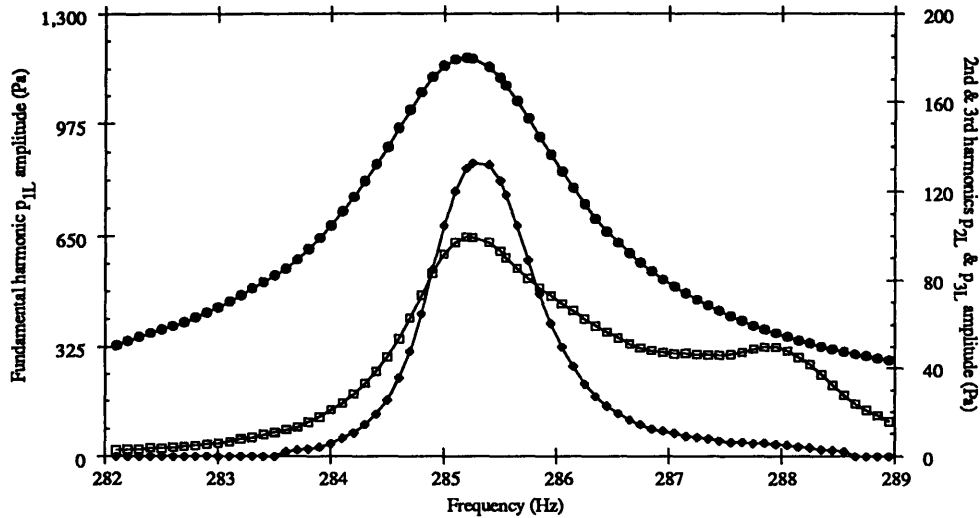

Figure 4.10 First three harmonic responses when driven near the fundamental resonance.
Forcing amplitude is $F_1=1.2$ g. Both the second (—□—, right scale) and third harmonic (—◇—, right scale) are of considerable amplitudes now, see text for the discussion on the second hump in the second harmonic response at about 2.7Hz above the resonance. —●—: amplitude of the fundamental harmonic, left scale.

Figure 4.11 First three harmonic responses when driven near the fundamental resonance. Forcing amplitude is $F_1=2.1$ g. The third harmonic amplitude (—◇—, right scale) exceeds that of the second harmonic (—□—, right scale) at the resonant frequency f_1. —●—: amplitude of the fundamental harmonic, left scale.
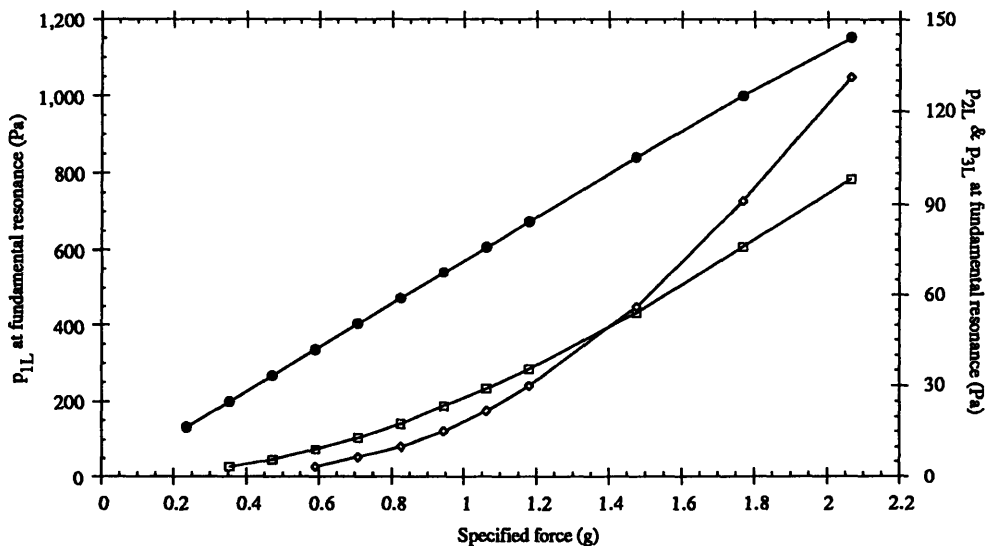

Figure 4.12 First three harmonic responses when driven at the fundamental resonance frequency. Forcing amplitude is increased from 0.35 g to 2.1 g. The amplitude of the second (—□—, right scale) and third harmonics (—◇—, right scale) behave as the square and cube of the forcing amplitude, respectively. —●—: amplitude of the fundamental harmonic at f_1, left scale.

In Fig. 4.10, the presence of the second hump in the second harmonic response, is explained by the mismatch between the second mode's resonant frequency and the fundamental mode's resonant frequency. The second mode's resonant frequency is 1% above the calculated value, or about 5.5 Hz above twice the fundamental resonant frequency. This means that when the driving frequency is the fundamental resonant frequency, the effective driving frequency on the nonlinearly generated second harmonic is not quite equal to the second resonant frequency, it is about 5.5Hz below where the *resonant* response would occur. However, the amplitude of the second harmonic depends on the *square* of the amplitude of the fundamental harmonic, thus when the resonator is driven at the fundamental resonance, the second harmonic response is still large despite the fact that the effective driving frequency is not resonant with the second mode's resonant frequency. The same dependence on the fundamental harmonic response limits the size of the second hump. No hump is expected for the third harmonic response because the third mode's resonant frequency was found to be almost exactly three times that of the fundamental.

When the forcing amplitude is increased further to 2.1 g (Fig. 4.11), the amplitude of the third harmonic becomes larger than that of the second harmonic. The pressure amplitudes of the first two nonlinearly generated harmonics have now increased to about 8% and 11%, respectively, of the fundamental harmonic. Fig. 4.12 shows the amplitudes of the fundamental, second, and third harmonics as a function of the forcing amplitude. The fundamental harmonic amplitude is seen to increase linearly with the forcing amplitude while the second and third harmonic amplitudes increase quadratically and cubically, respectively. These behaviors correspond to the perturbation solutions found in Chapter 2. For the second harmonic (see Eq. 2.22), the effective forcing function F_{dr2} was $\varepsilon_{quad}p_1^2$. For the third harmonic (see Eq. 2.23), the effective forcing function F_{dr3} was the product of p_1 and p_2, but since p_2 behaves as p_1^2, then the third harmonic should behave as p_1^3, which has now been shown in Fig. 4.12.

The value of p_{2L}/p_{1L}^2 gradually decreases as the forcing amplitude increases (Fig. 4.13). The decrease is expected because the third harmonic is increasingly extracting energy from the second harmonic as the forcing amplitude rises, thereby *decreasing* the increase in the second harmonic amplitude. ε_{quad} is thus dependent on the forcing amplitude since p_{2L}/p_{1L}^2 is not quite constant. However, since this dependence (see
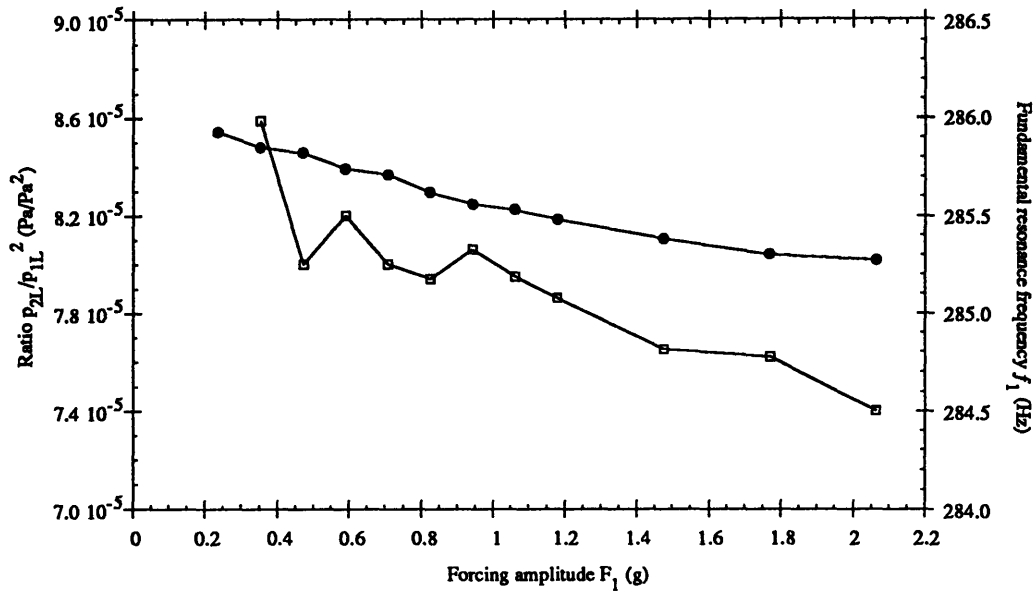
Figure 4.13 p_{2L}/p_{1L}^2 *and the fundamental resonant frequency as a function of forcing amplitude.*
Both the resonance frequency (-●-) and the ε_{quad} *factor* p_{2L}/p_{1L}^2 *(-□-) decrease with the forcing amplitude.*

Section 4.1.2) is small, a single representative value of p_{2L}/p_{1L}^2 corresponding to a forcing amplitude of 1.2 g was chosen in determining the value of ε_{quad} to use in the model.

The fundamental resonant frequency also seen to decrease as a function of the forcing amplitude. The decrease can be explained if the energy loss from the fundamental harmonic to higher harmonics is blithely interpreted as an effective nonlinear "dissipation". When nonlinear effects are small, the main damping factor is the viscous losses at the resonator walls. However, when nonlinear effects are large, it can be thought of as another damping factor. If β is an overall damping coefficient, then from classical dynamics, the resonant frequency f_1 can be defined[1] as the following,

$$f_1 = \sqrt{f_{10}^2 - 2\beta^2} \,, \tag{4.3}$$

where f_{10} is the resonant frequency in the absence of damping. When nonlinear effects are neglected, β is constant. Once the nonlinear effects are included in β, however, the value of β will increase as the forcing amplitude is increased, resulting in a lower resonant

---

[1] J. B. Marion, *Classical Dynamics of Particles and Systems*, 121 (1970).

frequency. The increase in β can be calculated from the decrease in Q_1, which has already been discussed. Using the information acquired on Q_1, the decrease in f_1 was calculated, although it was found to be smaller than the observed values. The causes for the discrepancy are unclear at this time.

4.1.2   Variables to Quench the Second Harmonic

The three parameters needed to quench the second harmonic were presented in Chapter 3. These are: ε_{quad} - the effective quadratic nonlinear coupling coefficient, F_2 - the forcing amplitude of a second forcing tone, and, ϕ_2 - the relative phase between the second and the first forcing tone. The one variable that was shown to be independent of the amplitudes of the nonlinearly generated harmonics is ϕ_2, the relative phase angle of the second forcing tone to the first forcing tone. In Section 3.2.3(b), the value of ϕ_2 was found to be 270°, a value which assumed that the vibrator setup had zero phase shift between the electrical input and its mechanical response to that input. However, the vibrator setup did not respond with constant gain or phase (Figs. 3.21 and 3.22). The phase deviations (actual forcing signal to the specified forcing signal) were found to be about -10° and 11° at the fundamental and second resonant frequencies, respectively. Incorporating these deviations results in the following for the two-tone forcing function used in the computational model:

$$F_{dr}(t)=F_1\sin\left(\omega_{dr}t+10°\right)+F_2\sin\left(2\omega_{dr}t+\phi_2-11°\right),\qquad(4.4)$$

where ω_{dr} is the fundamental resonant frequency: $\omega_{dr}=\omega_1=2\pi f_1$. In Eq. 4.4, the relative phase angle between the second and first forcing tone is a function of the phase deviations and the originally calculated $\phi_2=270°$. If the phase on the first tone is set to 0°, then the following is the result:

$$F_{dr}(t)=F_1\sin\left(\omega_{dr}t\right)+F_2\sin\left(2\omega_{dr}t+\underbrace{\phi_2-11°-2(10°)}_{270°}\right).\qquad(4.5)$$

The new value of ϕ_2 is then calculated as 270°+31°=301°. The second harmonic, therefore, should be quenched when ϕ_2 is about 300°, given the appropriate amplitude (F_2) on the second forcing tone. The amplitude of the second forcing tone depends directly on the amplitude of the second harmonic, which depends on the quadratic nonlinear coupling

coefficient ε_{quad}. The coupling coefficient and the amplitude of the second forcing tone were found explicitly in Eqs. 3.37 and 3.43, rewritten here as

$$\varepsilon_{quad} = \left| \frac{2f_1^2(L)\left(\hat{k}_2^2 - k_2^2\right)}{f_2(L)\langle f_2(x)f_1^2(x)\rangle} \left(\frac{p_{2L}}{p_{1L}^2}\right)_{f_1} \right|, \tag{4.6}$$

and

$$F_2 = \frac{\int \frac{1}{2}f_2(x)F_{dr2x}dV}{\int f_2(x)F_{2x}dV}. \tag{4.7}$$

The ratio p_{2L}/p_{1L}^2 in Eq. 4.6 was determined experimentally in the previous section and was shown to depend weakly on the amplitude of the first forcing tone F_1. Using the values in Table 4.1 and Fig. 4.13, the values of ε_{quad} as a function F_1 is shown in Fig. 4.14. These values are approximate and will only be used as starting points in the quenching process; adjustments to the experimental setup are expected.

To determine the value of F_2, the amplitude of the second forcing tone, Eq. 4.7 shows that the only variable subject to change is F_{dr2x}, the spatial component of F_{dr2} (the effective forcing function that generates the second harmonic):

$$F_{dr2} = F_{dr2x}F_{dr2t} = \varepsilon_{quad}\left[p_1(x,t)\right]^2 \;\rightarrow\; F_{dr2x} = \varepsilon_{quad}\left[p_1(x)\right]^2, \tag{4.8}$$

where $p_1(x,t) = p_1(x)p_1(t)$ is the fundamental harmonic response, and $p_1(t)$ has an amplitude of unity. In Eq. 4.8, the amplitude of $p_1(x)$ is a function of p_{1L}, thus the value of F_2 can be expected to grow as the square of p_{1L}. Since p_{1L} depends directly on F_1, then the amplitude of the second (quenching) forcing tone F_2 can thus be written

$$F_2 = F_{2,const}F_1^2, \tag{4.9}$$

where $F_{2,const}$ is a constant of unit g^{-1} which includes the ratio of the volume integrals in Eq. 4.7 and depends directly on ε_{quad}. Since ε_{quad} depends only weakly on F_1, one value of ε_{quad} is chosen corresponding to $F_1 = 1.2\ g$, then F_2 should behave quadratically as shown in Fig. 4.15.

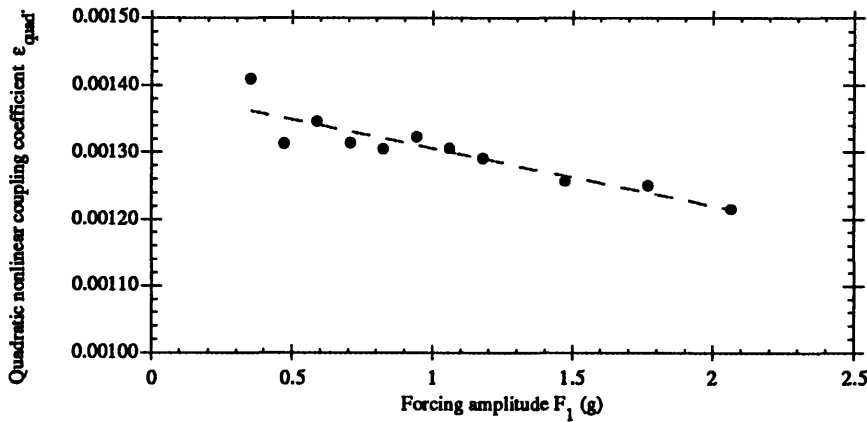*Figure 4.14 Quadratic nonlinear coupling coefficient as a function of first forcing tone amplitude.*
—●—: The quadratic nonlinear coupling coefficient ε_{quad}. The dashed line is a guide to the eye.
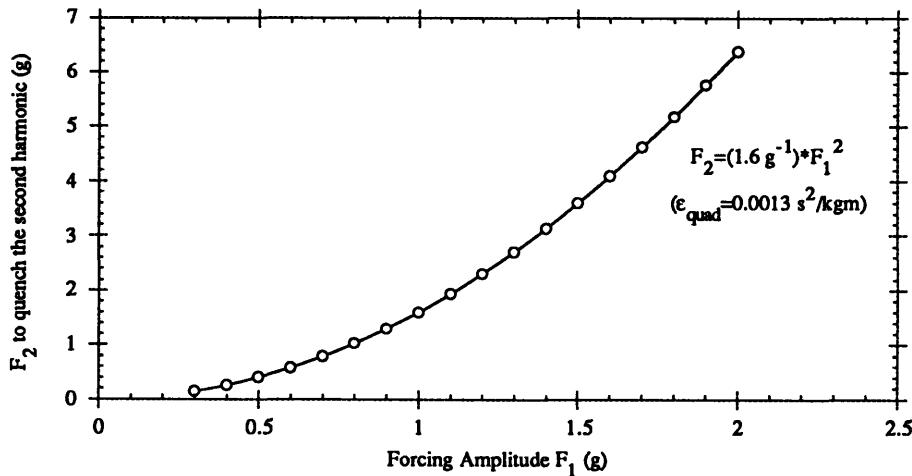

Figure 4.15 Modeled second forcing tone amplitude versus first forcing tone amplitude.
—○—: Second forcing tone amplitude F_2.

From Eq. 4.7, the constant $F_{2,const}$ was calculated as about 1.6 g^{-1}. Thus, given an amplitude of 1 g on the first forcing tone, to quench the nonlinearly generated second harmonic, the amplitude of the second forcing tone should be approximately 1.6 g. If the amplitude of the first forcing tone is doubled to 2 g, then the expected quenching amplitude of the second forcing tone increases four times, to 6.4 g. The second forcing tone can only quench the second harmonic, thus if the first forcing amplitude is large, another forcing tone needs to be introduced to quench the third harmonic due to a combination of quadratic and cubic coupling effect.

4.2 Single forcing frequency response

This section will compare the *single* forcing tone response results obtained from the experimental setup and the computational model. The computational model was limited to calculating just the first three harmonics. Among other assumptions, the model calculated the amplitude of the first harmonic assuming no energy loss to the higher harmonics. Thus, the model will become invalid when significant energy is coupled to modes above the third harmonic for very large forcing amplitudes. The responses as a function of frequency with a constant forcing amplitude will be discussed first. Then, as the forcing frequency is fixed at the fundamental resonant frequency, the responses of the harmonics as a function of the forcing amplitude will be presented.

4.2.1 Amplitude response (to frequency)

The experimental and computational responses of the gas to frequency sweeps through the first three resonances with specific forcing amplitudes are shown in Figs. 4.16 to 4.18. Although the forcing amplitudes were kept small, experimentally, nonlinear effects were still evident by observing the amplitude spectrum. Only the dominant harmonic components are shown in these graphs. Thus, when the driving frequency is swept through the second resonant frequency ω_2, although harmonics with frequencies $2\omega_2$, $4\omega_2$, and so on are excited, Fig. 4.17 assumes these harmonics to be small and only graphs the dominant response, the ω_2 component of the amplitude spectrum. On the other hand, the computational model assumes linear response so that near the resonant frequencies, the only response is of the same frequency, no nonlinearly excited harmonics are present. The variables Q_n (quality factors) and n_r (resonant frequency ratios) needed in the model were determined experimentally in Section 4.1. The forcing amplitudes are F_1=1.18 g, F_2=2.24 g, and F_3=1.64 g, respectively, through the first three resonances.
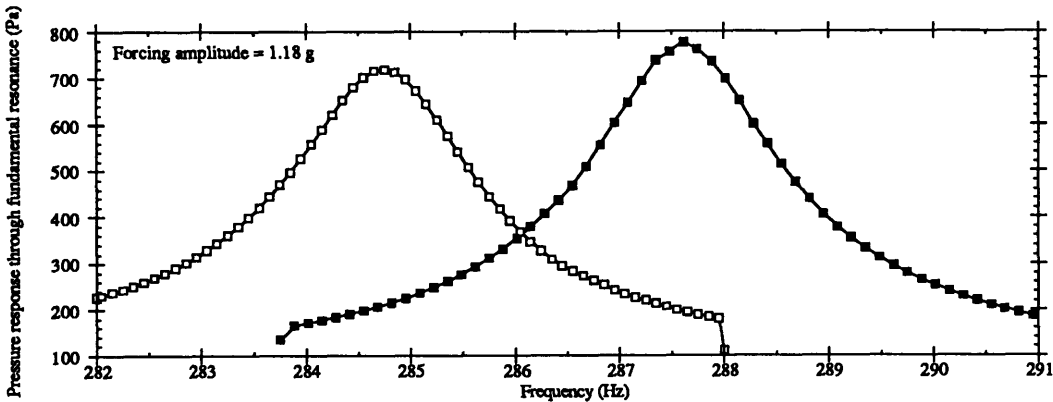
Figure 4.16 Experimental and computational response through the fundamental resonance. Forcing amplitude is 1.18 g. —□—: experimental pressure response amplitude, —■—: computational values of pressure response amplitudes near the fundamental resonant frequency.
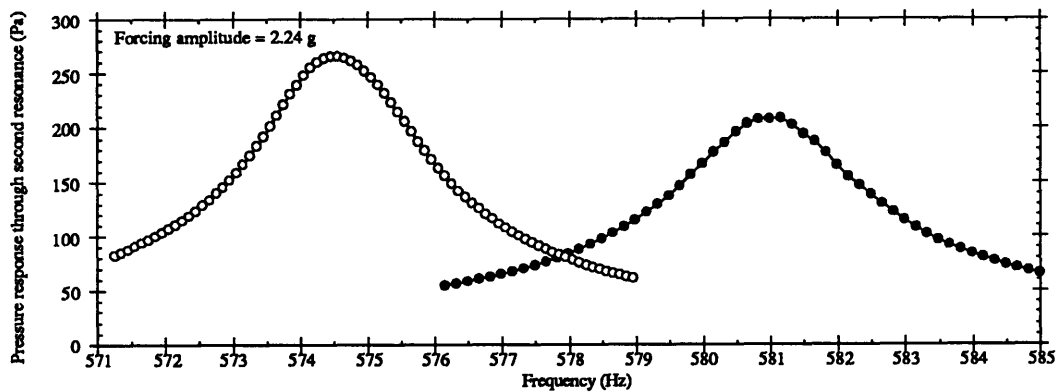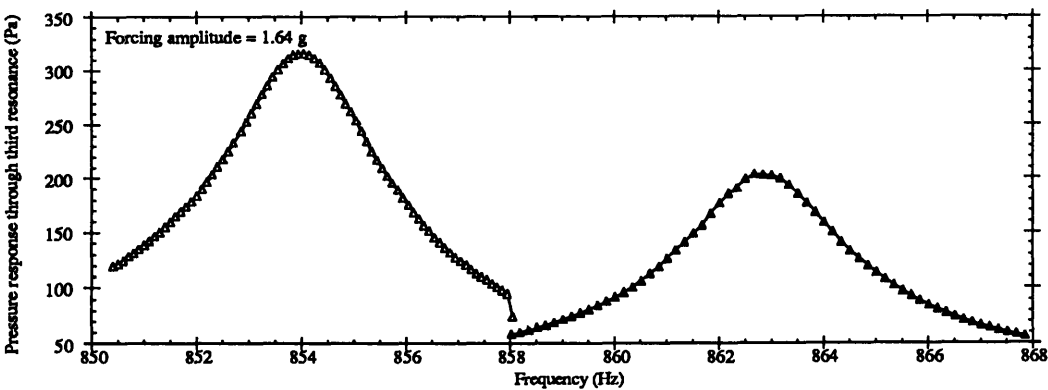

Figure 4.17 Experimental and computational response through the second resonance. Forcing amplitude is 2.24 g. —○—: experimental pressure response amplitude, —●—: computational values of pressure response amplitudes near the second resonant frequency.

Figure 4.18 Experimental and computational response through the third resonance. Forcing amplitude is 1.64 g. —△—: experimental pressure response amplitude, —▲—: computational values of pressure response amplitudes near the third resonant frequency.

93

The amplitude deviation was smallest for the first resonance, computational values were about 7% above measured values. The amplitude deviation was much larger for the second and third resonance responses, the modeled response amplitudes were about 17% and 35% lower, respectively, than the measured values. The shifts in the values of the resonant frequencies are mainly the result of assumptions made in determining the resonant frequencies in the model. For example, the flow of the medium through the area transition at the center of the resonator is not smooth and will certainly affect the resonant frequencies.

The next set of graphs (Figs. 4.19 to 4.28) show how the experimental and modeled amplitudes of the fundamental harmonic (p_{1L}) and the first two nonlinearly generated harmonics $(p_{2L}$ and $p_{3L})$ behave as the single forcing tone frequency is swept from a few Hertz below to a few Hertz above the fundamental resonant frequency at a fixed force.

The forcing amplitude in Figs. 4.19 to 4.23 is $F_1=1.2\ g$. Fig. 4.19 shows the experimental response where the amplitudes of the second and third harmonic are seen to be about equal at the fundamental resonant frequency f_1. The amplitudes of the nonlinear effects are not maximized at f_1, but slightly above it. This *pulling* effect may be explained by the non-integer resonant frequency ratios n_r, which is especially apparent in the second harmonic response amplitude p_{2L}. A thorough investigation of the pulling effects has not been conducted. The second maxima or hump on p_{2L} occurs as a result of the *effective* driving frequency on the second harmonic finally matching the actual second resonant frequency. The effect is better displayed in Fig 4.20, where the amplitude ratios of the second and third harmonic to the first harmonic are graphed against the driving frequency. The amplitude of the second harmonic is smaller than its peak value when the driving frequency is at the fundamental resonant frequency. However, relative to the first harmonic, the amplitude of the second harmonic is largest when the driving frequency is exactly one-half of the second resonant frequency $(n_r=2.02)$, or about 1% higher than the fundamental resonant frequency. There is no hump seen for the third harmonic because the third resonant frequency is almost exactly three times the fundamental, i.e., $n_r=3.00$.
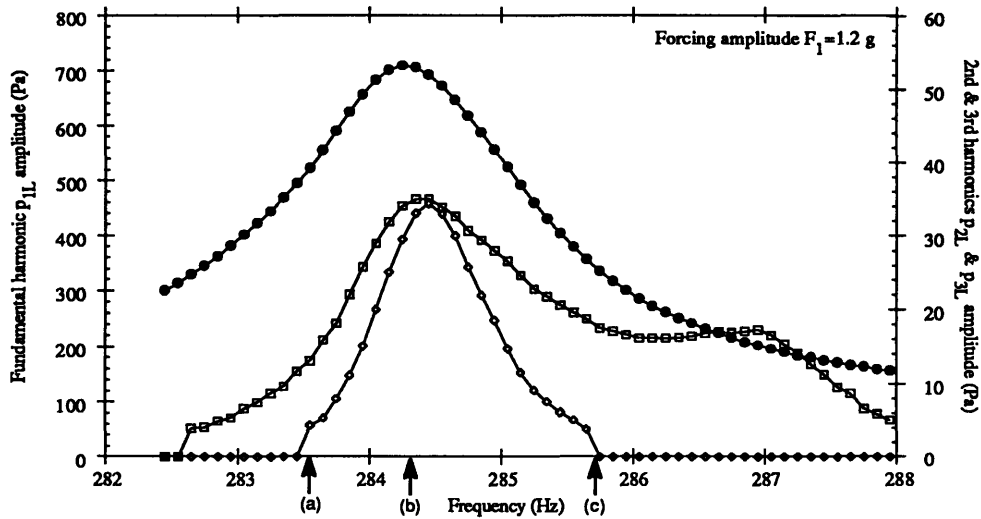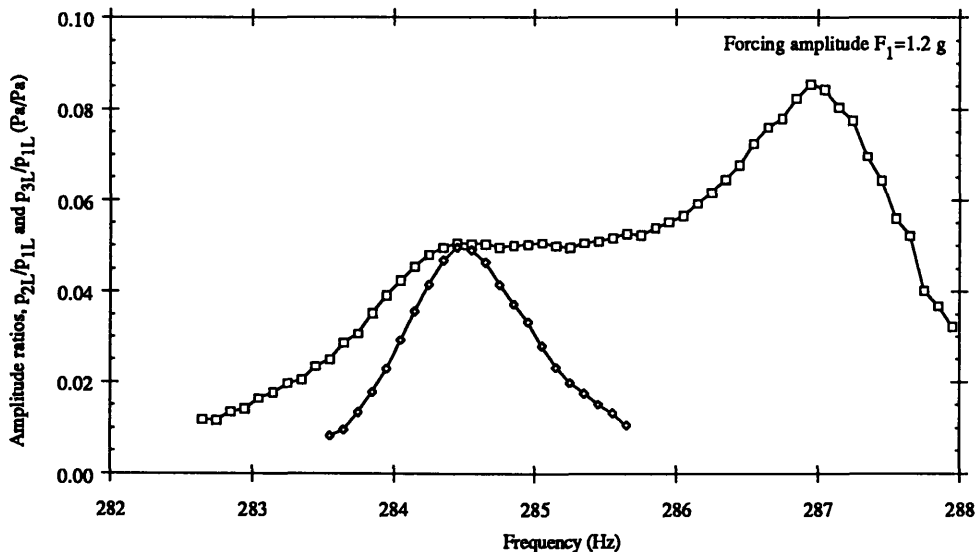
Figure 4.19 Experimental amplitudes of the first three harmonics near the first resonance.
Forcing amplitude is $F_1=1.2$ g. The forcing frequency f_{dr} is swept through the fundamental resonant
frequency f_1. p_{2L} and p_{3L} (-□- and -◇-, right scale) are about equal at f_1. Changes in p_{3L} occur more
quickly about f_1 than does p_{2L} because $Q_3>Q_2$. The three arrows refer to frequencies at which the total
pressure profile and amplitude spectrum will be shown in Fig. 4.23. -●-: p_{1L}, left scale.

Figure 4.20 Experimental amplitude ratios of the second and third harmonics near the first resonance.
Forcing amplitude is $F_1=1.2$ g. The ratio of the second to first harmonic, p_{2L}/p_{1L} (-□-) is largest
when the effective driving frequency $(2f_{dr})$ on the second harmonic is equal to the resonant frequency of
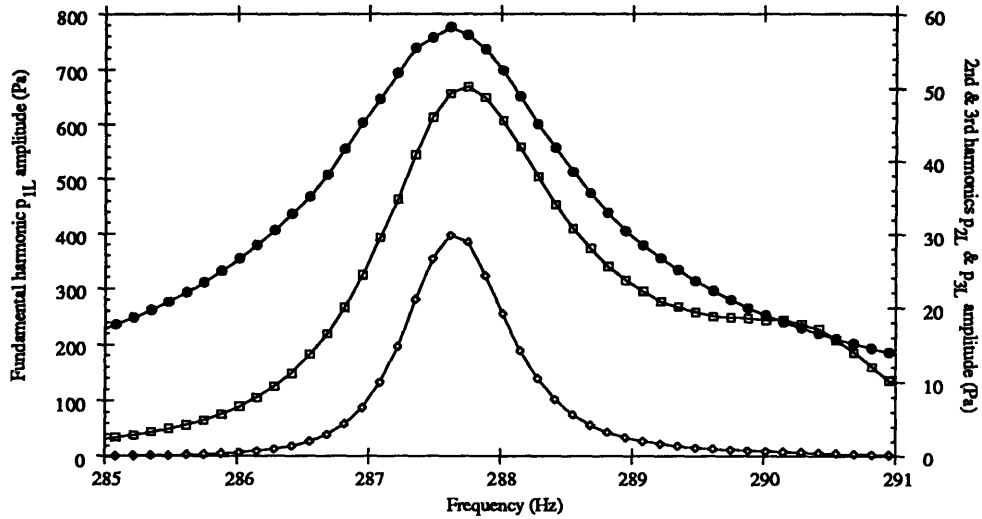the second mode. p_{3L}/p_{1L} (-◇-) is maximum at slightly above f_1.

Figure 4.21 Modeled amplitudes of the first three harmonics near the first resonance.
Forcing amplitude is $F_1=1.2$ g. p_{2L} (─□─, right scale) is much larger than measured values while p_{3L} (─◇─, right scale) is about equal to measured values at f_1. p_{2L} is larger because it depends on the square of p_{1L} (─●─, left scale) which is also larger than measured values.
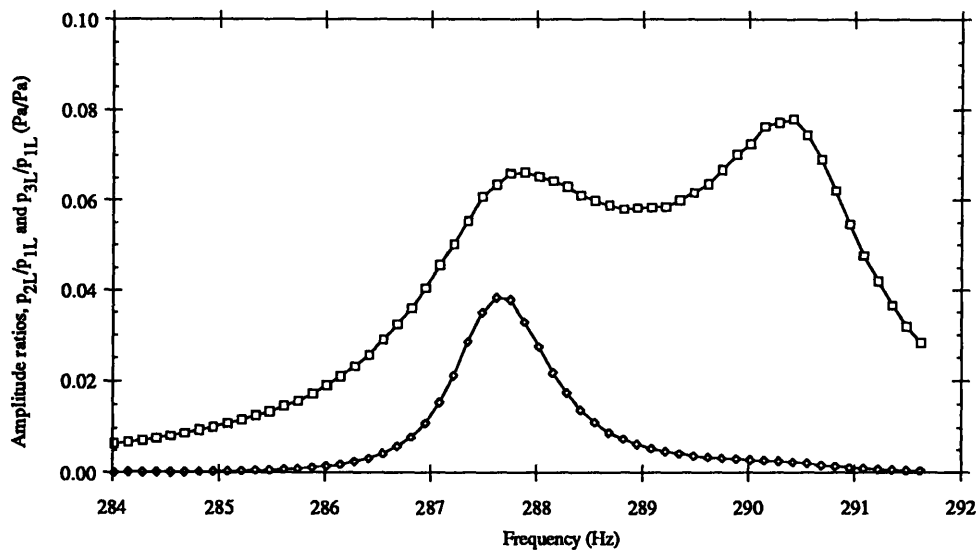

Figure 4.22 Modeled amplitude ratios of the second and third harmonics near the first resonance. Forcing amplitude is $F_1=1.2$ g. The ratio of the second to first harmonic, p_{2L}/p_{1L} (─□─) is largest when the effective driving frequency on the second harmonic is equal to the resonant frequency of the second mode. p_{3L}/p_{1L} (─◇─) is maximum at f_1.
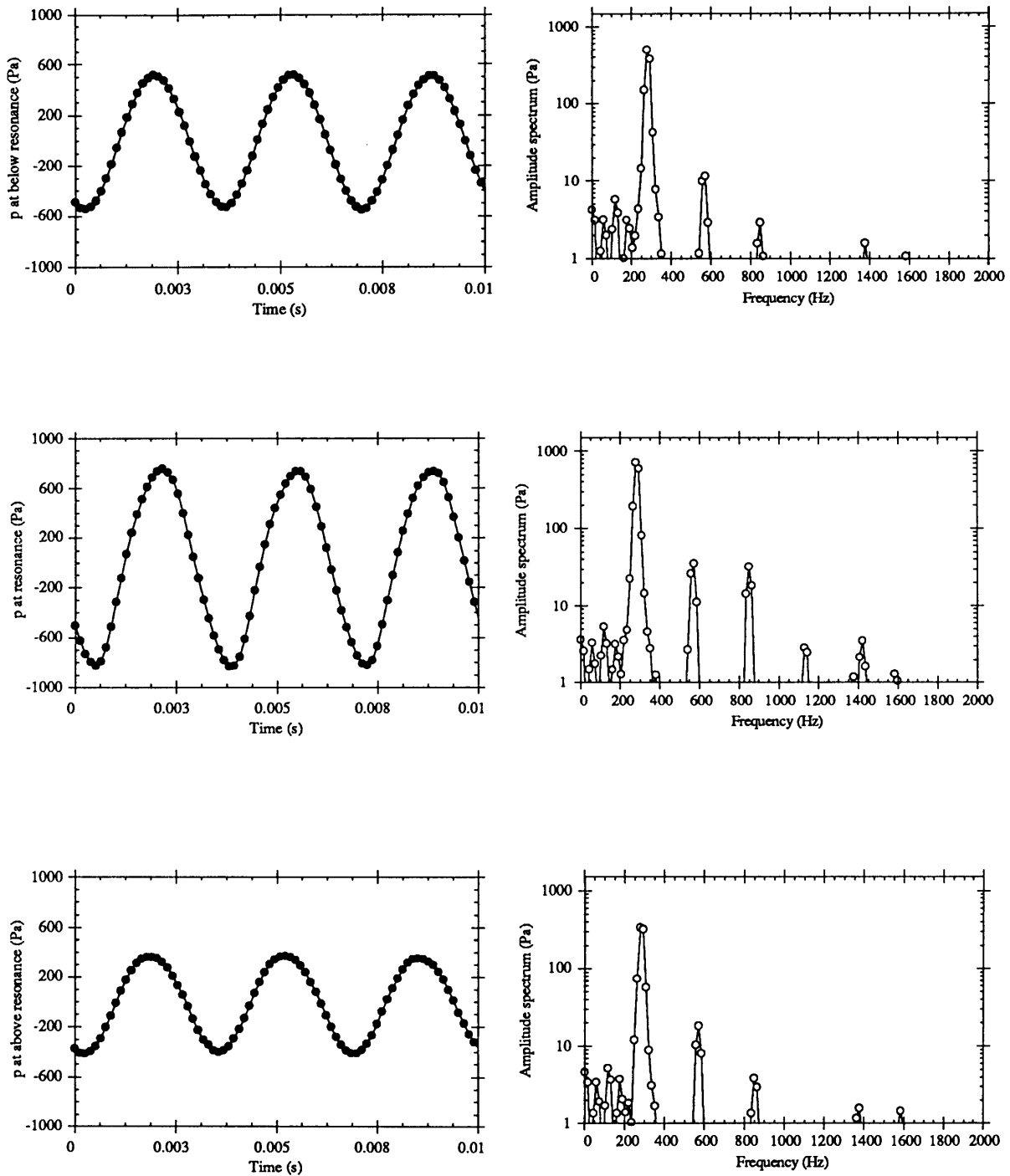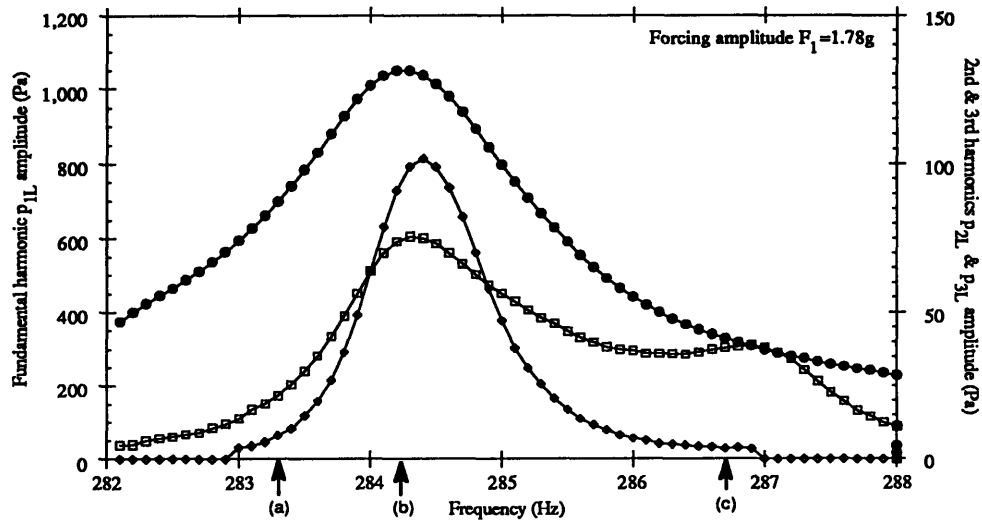
Figure 4.23 Experimental pressure profile and amplitude spectrum about the first resonance. Forcing amplitude is $F_1=1.2$ g. (a) top two graphs: driving frequency (283.5 Hz) is below f_1. (b) middle two graphs: driving frequency (284.3 Hz) is at f_1. (c) bottom two graphs: driving frequency (285.8 Hz) is above f_1. —●—: pressure profile, —○—: amplitude spectrum.

Figure 4.24 Experimental amplitudes of the first three harmonics near the first resonance. Forcing amplitude is $F_1=1.78$ g. p_{3L} ($\diamond$, right scale) is larger than p_{2L} ($\square$, right scale) at f_1. The three arrows refer to frequencies at which the total pressure profile and amplitude spectrum will be shown in Fig. 4.28. $\bullet$: p_{1L}, left scale.

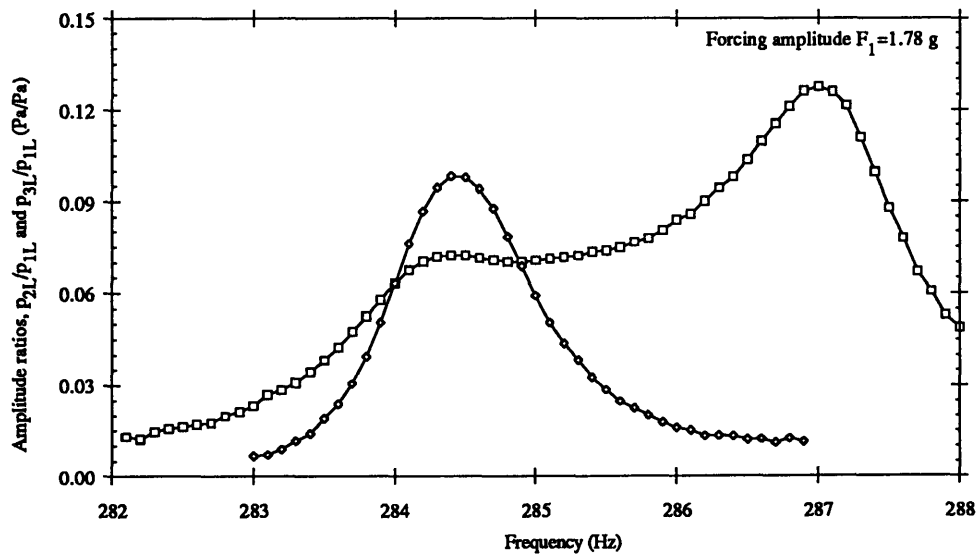
Figure 4.25 Experimental amplitude ratios of the second and third harmonics near the first resonance. Forcing amplitude is $F_1=1.78$ g. The ratio of the second to first harmonic, p_{2L}/p_{1L} ($\square$) is largest when the effective driving frequency on the second harmonic is equal to the resonant frequency of the second mode. p_{3L}/p_{1L} ($\diamond$) is maximum at slightly above f_1.
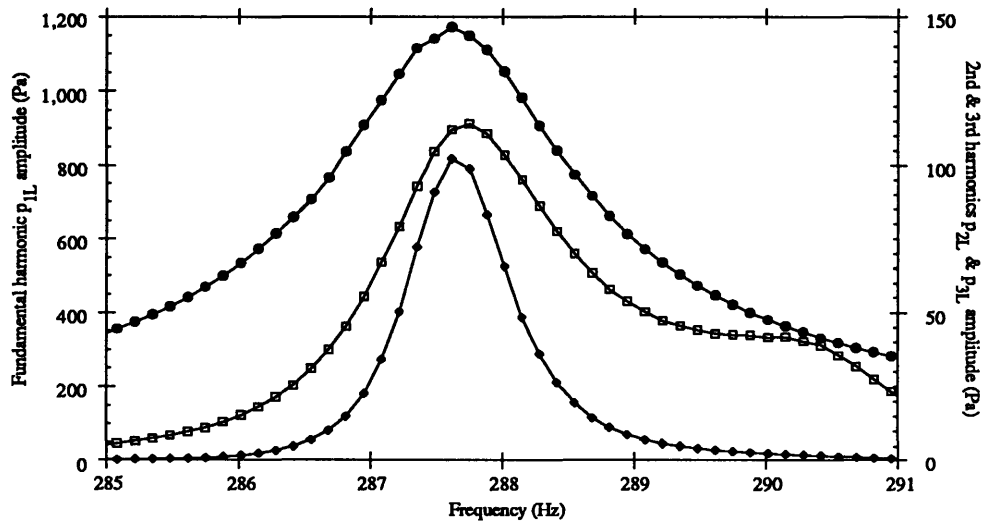
98

Figure 4.26 Modeled amplitudes of the first three harmonics near the first resonance. Forcing amplitude is $F_1=1.78$ g. p_{2L} (⊓⊐⊓, right scale) is much larger than measured values while p_{3L} (◇, right scale) is still about equal to measured values at f_1. ●: p_{1L}, left scale.
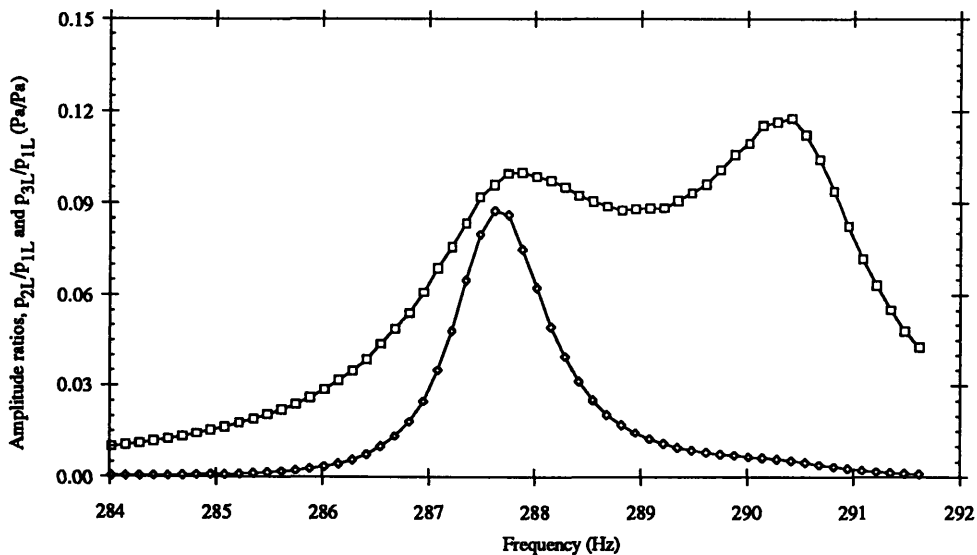

Figure 4.27 Modeled amplitude ratios of the second and third harmonics near the first resonance. Forcing amplitude is $F_1=1.78$ g. The ratio of the second to first harmonic, p_{2L}/p_{1L} (⊓⊐⊓) is largest when the effective driving frequency on the second harmonic is equal to the resonant frequency of the second mode. p_{3L}/p_{1L} (◇) is maximum at f_1.
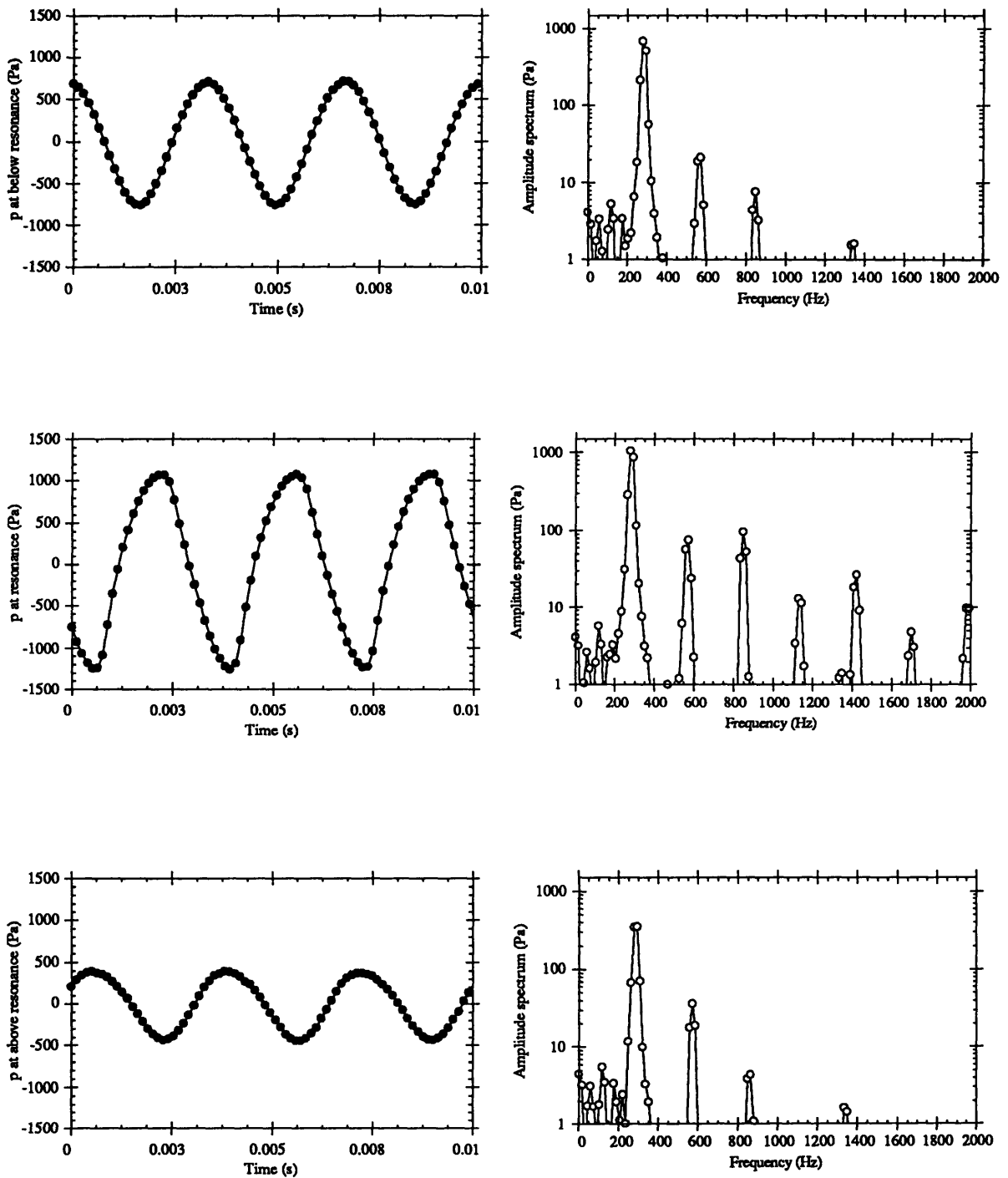
Figure 4.28 Experimental pressure profile and amplitude spectrum about the first resonance. Forcing amplitude is $F_1=1.78$ g. (a) top two graphs: driving frequency (283.3 Hz) is below f_1. (b) middle two graphs: driving frequency (284.23 Hz) is at f_1. (c) bottom two graphs: driving frequency (286.7 Hz) is above f_1. ─●─: pressure profile, ─○─: amplitude spectrum.

100

The modeled results of the frequency sweep through the fundamental resonant frequency with a forcing amplitude of $F_1=1.2$ g are shown in Figs. 4.21 and 4.22. The hump in the second harmonic is also present because in the computational model, the resonant frequency ratios were defined from experimental values of n_r. The amplitude of the modeled second harmonic (Fig. 4.21) at f_1 is much higher (40%) than experimental values because the computed amplitudes of the first harmonic is already larger than measured values, and the second harmonic amplitude depends on the square of the first harmonic amplitude. The modeled amplitude of the third harmonic p_{3L}, is slightly lower (12%) than experimental values. Fig. 4.22 shows the amplitude ratios from the model, p_{2L}/p_{1L} is again maximum at the second hump where the effective driving frequency on the second harmonic is equal to the second resonant frequency.

The experimental pressure profile and the breakdown to its harmonic components at three frequency points labeled (a), (b), and (c) in Fig. 4.19 are shown in Fig. 4.23. The amplitude spectrums in this figure are rough (the frequency resolution is: $\Delta f=14.6$ Hz), but sufficient to show harmonics generation. The resolution was kept low to reduce processing time required by the LabVIEW VI's, which are currently set to calculate the amplitude spectrums continuously once every two seconds. In Fig. 4.23a, the driving frequency is at about 0.8 Hz (0.3%) below f_1, the amplitude spectrum shows that only the second harmonic is of significant amplitude. The third harmonic is just beginning to emerge from the background. In Fig. 4.23b, the driving frequency is at f_1 and the nonlinearly excited harmonics have reached near-maximum values. While the pressure profile show that the overall pressure amplitude is at a maximum, the shape is not as sinusoidal as in Fig. 4.23a or 4.23c. In Fig. 4.23c, the driving frequency is about 1.5 Hz (0.5%) above f_1. The second harmonic is still of significant amplitude relative to the first harmonic but the higher harmonics have diminished to negligible levels, which results in a near sinusoidal pressure profile.

Figs. 4.24 to 4.28 show the same information as Figs. 4.19 to 4.23, except that the forcing amplitude has been increased by 50% to $F_1=1.78$ g. In Fig. 4.24, the experimental amplitude of the third harmonic p_{3L} is larger (35%) than the amplitude of the second harmonic p_{2L} at f_1. This was expected since p_{3L} had been found to grow as the cube of p_{1L}, and p_{2L} only the square of p_{1L}. Fig. 4.25 shows the experimental amplitude ratios p_{2L}/p_{1L} and p_{3L}/p_{1L} as a function of forcing frequency. Both ratios have increased from values corresponding to a lower forcing amplitude (Fig. 4.20), with the ratio p_{3L}/p_{1L} increasing

faster than p_{2L}/p_{1L}. The modeled results for this forcing amplitude are shown in Figs. 4.26 and 4.27. In Fig. 4.26, the amplitude of the third harmonic has increased to about the same level as the measured values, but the amplitude of the second harmonic is still larger (46% over experimental p_{2L}) even though its growth rate is lower than the third harmonic. The modeled amplitude ratios (Fig. 4.27) have also increased from before (Fig. 4.22) in the similar manner to the experimental results.

The experimental pressure profile and the breakdown to its harmonic components at three frequency points labeled (a), (b), and (c) in Fig. 4.24 are shown in Fig. 4.28. When the driving frequency is at f_1 and $F_1=1.78$ g, many more harmonics are generated through nonlinear effects (Fig. 4.28b) than when $F_1=1.2$ g. These higher harmonics are generated by the increased amplitudes and interactions among the lower harmonics. The pressure profile in Fig. 4.28b is clearly much less sinusoidal (than the pressure profile in Fig. 4.24b) because of the emergence of the higher harmonics at a larger forcing amplitude.

4.2.2 Amplitude response (to forcing amplitude)

In Section 4.2.1, the experimental and modeled pressure response amplitudes of frequency sweeps through the first three resonant frequencies were shown (Figs. 4.16 to 4.18). Each of the three resonance-sweep response comparisons corresponded to a specific forcing amplitude. Now, the frequencies are kept at the three resonant frequencies while the forcing amplitudes are changed. The experimental and modeled response amplitudes are compared in Fig. 4.29. The modeled response amplitudes at the fundamental resonant frequency matched well with experimental values. At both the second and third resonant frequencies, the modeled response amplitudes were smaller than experimental values for all forcing amplitudes. Furthermore, the growth rates (slopes) of the modeled response amplitudes corresponding to the second and third resonant frequencies are clearly less than that actually measured, especially at the third resonant frequency (Fig. 4.29c). The cause of the deviations may be related to the assumptions made in the model on boundary conditions and should be investigated in more detail in the future.
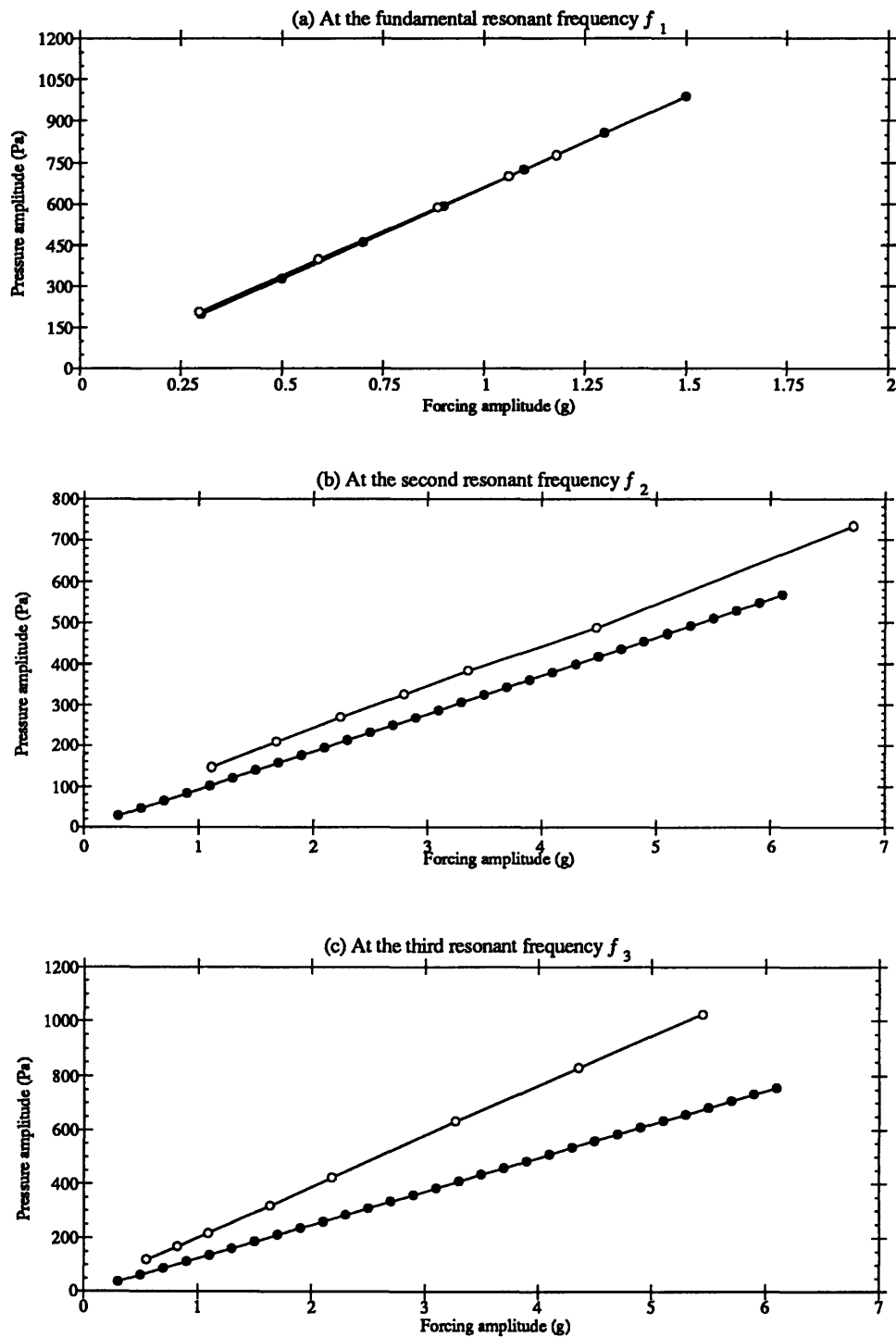
Figure 4.29 Experimental and modeled response amplitudes at the first three resonant frequencies. Response amplitudes at (a) the fundamental resonant frequency, (b) the second resonant frequency, and (c), the third resonant frequency. ●: modeled response amplitudes, ○: experimental response amplitudes.

The discussion is now turned to comparing the modeled and measured values of the first three harmonics when the forcing tone is at the fundamental resonant frequency f_1 and the forcing amplitude F_1 varied. Fig. 4.30 shows the experimentally measured values of the harmonics and Fig. 4.31 shows the computed values with the same scales. In Fig. 4.30, the fundamental harmonic pressure amplitude behaves linearly with the forcing amplitude at first, when nonlinear effect losses are small, but becomes more and more nonlinear as the forcing amplitude is increased. The computed fundamental harmonic, however, behaves linearly with the force because of the assumptions made in the computational model. In the model, the reduction in the amplitude of the fundamental harmonic due to energy transferred to the higher harmonics was not included, thus the computed fundamental harmonic is strictly a function of the force, not of all other harmonics.

The second and third harmonics increase quadratically and cubically as discussed. The measured values of p_{2L} and p_{3L} show that experimental curves are approximately equal at $F_1=1.3$ g while the computed values are equal at $F_1=1.9$ g . The differences between the measured and computed values for each of the three harmonics are compared individually in Fig. 4.32. In (a), the measured values are always smaller than the modeled values and as nonlinear effect losses increase with the forcing amplitude, the measured values increase with a decreasing rate. In (b) and (c), the same effects are evident. The increases in the measured values of the second and third harmonics eventually deviate from strictly quadratic and cubic behavior, respectively, as higher harmonics are generated and extract energy from the lower harmonics.

Thus, the computational model is seen to predict the amplitudes of the first three harmonics well for forcing amplitudes below about $F_1=1.25$ g. Beyond this forcing amplitude, the present model grossly over-predicts the harmonic amplitudes.
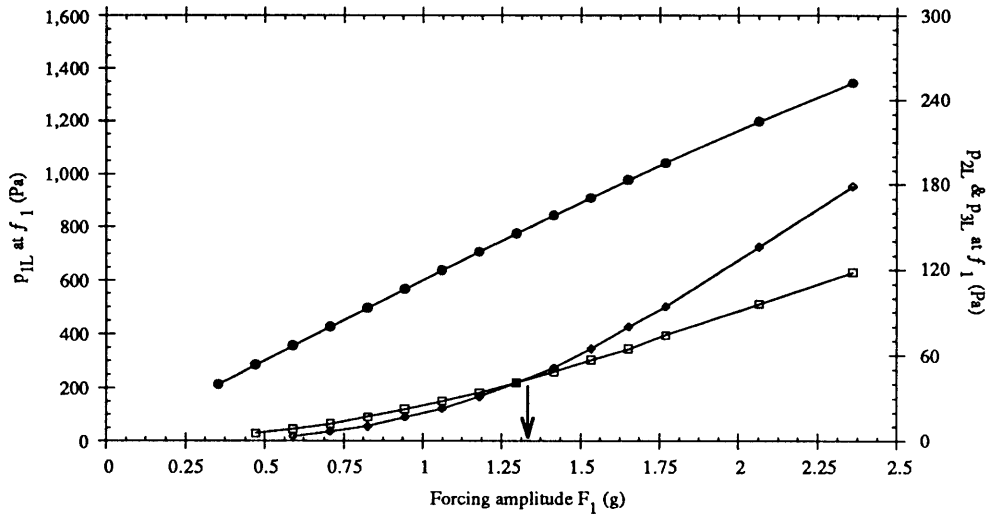
Figure 4.30 Experimental pressure response amplitudes of the first three harmonics.
The driving frequency is held at the fundamental resonant frequency f_1. The fundamental harmonic
amplitude p_{1L} (─●─, left scale) is almost linear, the decrease in the slope is due to losses to higher
nonlinearly generated harmonics which increase rapidly, especially p_{3L} (─◇─, right scale). p_{3L}
exceeds p_{2L} (─□─, right scale) at about $F_1 = 1.3$ g.
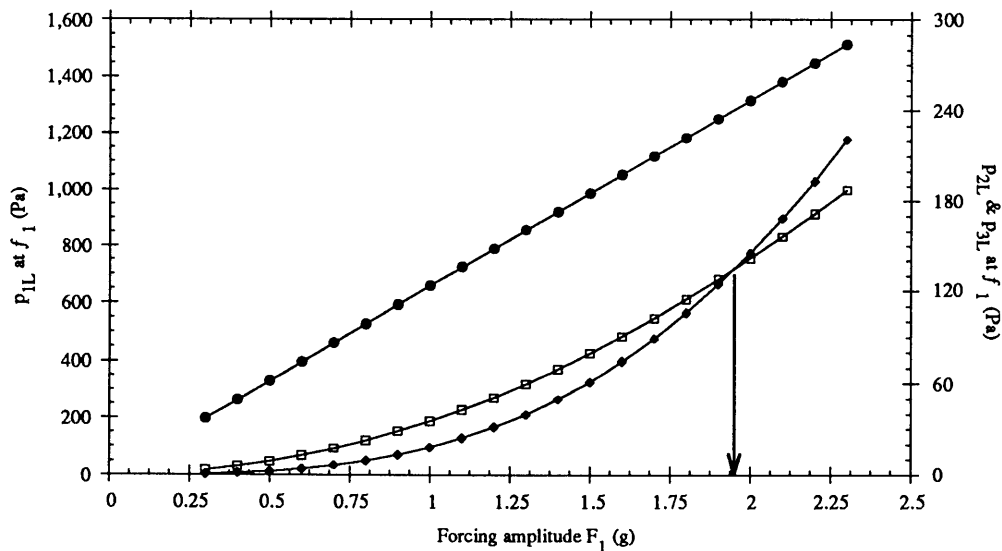

Figure 4.31 Modeled pressure response amplitudes of the first three harmonics.
The fundamental harmonic is linear by assumption, $p_{2L} = p_{3L}$ when F_1 is about 1.9 g. ─●─: p_{1L},
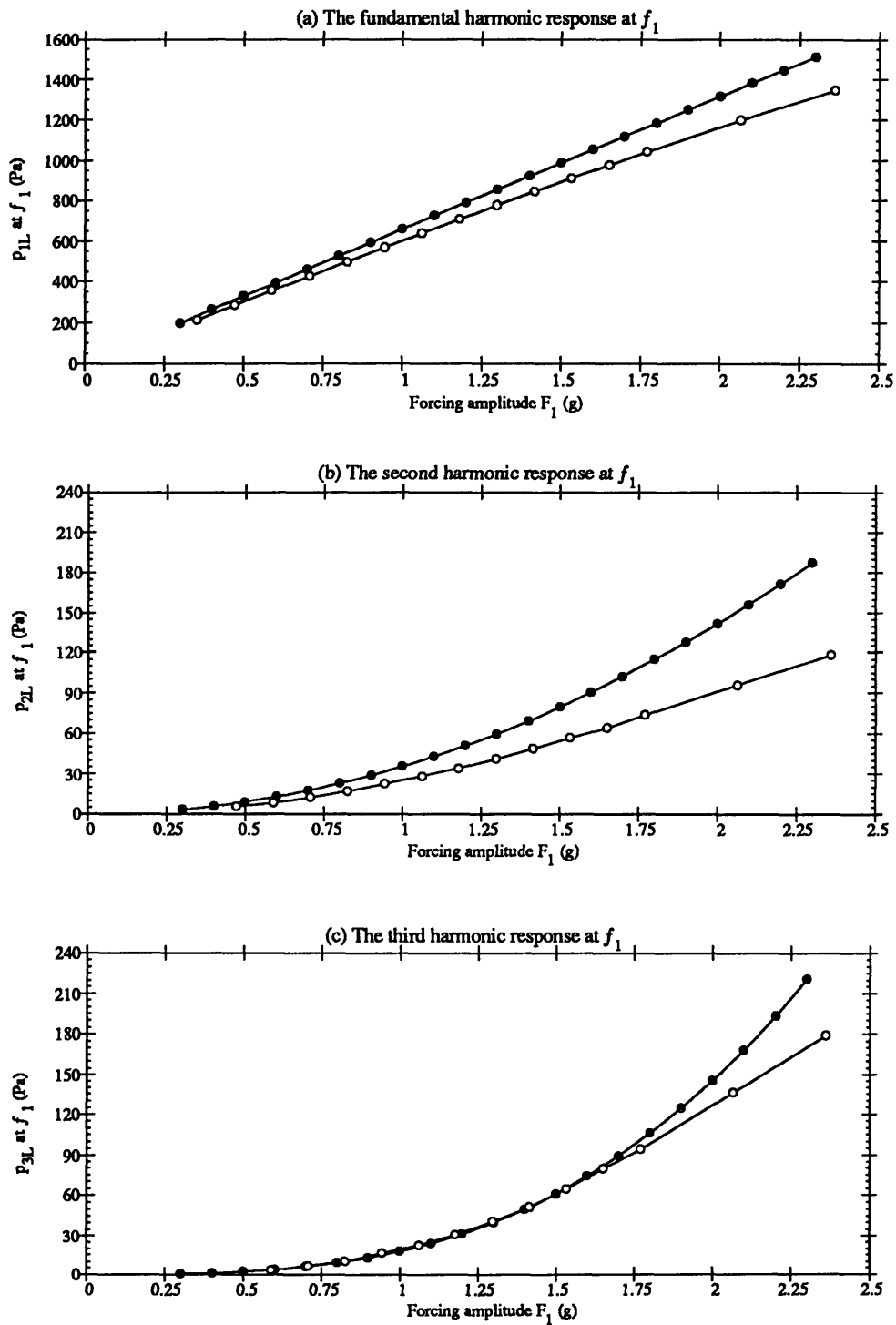*left scale, ─□─: p_{2L}, right scale, and ─◇─: p_{3L}, right scale.*

Figure 4.32 Experimental and modeled pressure response amplitudes of the first three harmonics. The driving frequency is held at the fundamental resonant frequency f_1. (a) The fundamental harmonic, (b) the second harmonic, and (c), the third harmonic. $-\!O\!-$: experimental response amplitudes, $-\!\bullet\!-$: modeled response amplitudes.

4.3 Multiple forcing frequencies response

In this section, the principle of the active control approach is demonstrated experimentally. The first objective is show experimentally and computationally that the nonlinearly generated second harmonic can be quenched by a second forcing tone (frequency $2f_1$). If the amplitude of the first forcing tone is kept low (to avoid direct cubic nonlinear coupling effects), quenching the second harmonic with the second forcing tone will also result in the quenching of all higher harmonics, as discussed in Chapter 3. When a second forcing tone is no longer sufficient in quenching all of the higher harmonics because of the emergence of cubic nonlinear coupling effects, the amplitude of the unquenched third harmonic is then used to calculate the direct cubic nonlinear coupling coefficient, ε_{cubic}. A brief discussion on calculating ε_{cubic} will be presented, followed by a discussion on the experimental results to a three-tone (frequencies f_1, $2f_1$, and $3f_1$) forcing function that quenches both the second and third harmonics. Finally, the responses to other combinations of frequency tones in a forcing function will be briefly discussed.

4.3.1 Quenching the Second Harmonic

In Section 4.1.2, the amplitude of the second forcing tone necessary for quenching the quadratic response of the resonator, F_2, was calculated as approximately $1.6F_1^2$ g, where F_1 is the amplitude of the first forcing tone. The value of F_1 used here to demonstrate the quenching of the harmonics is a fixed 1.2 g.

In Eq. 4.5, the relative phase angle between the second and the first forcing tone was estimated at about $\phi_2 = 300°$. If the amplitude of the second forcing tone is fixed while a sweep of ϕ_2 is performed, then the behavior of the amplitudes of the second and third harmonics can be shown as a function of ϕ_2. Three values of F_2 were imposed; the corresponding responses of p_{2L} and p_{3L} as a function of ϕ_2 are shown in Figs. 4.33 to 4.38. In Fig. 4.33, the value of F_2 is 1.12 g and is too weak to quench the harmonics experimentally. Computationally (Fig. 4.34), similar behavior is seen, except that the computed p_{2L} is larger than the experimental values seen in Fig. 4.33. The value of ϕ_2 at which the second forcing tone destructively interferes with the second harmonic is indeed seen to be about 300°. The actual measured value of ϕ_2 was about 306°.
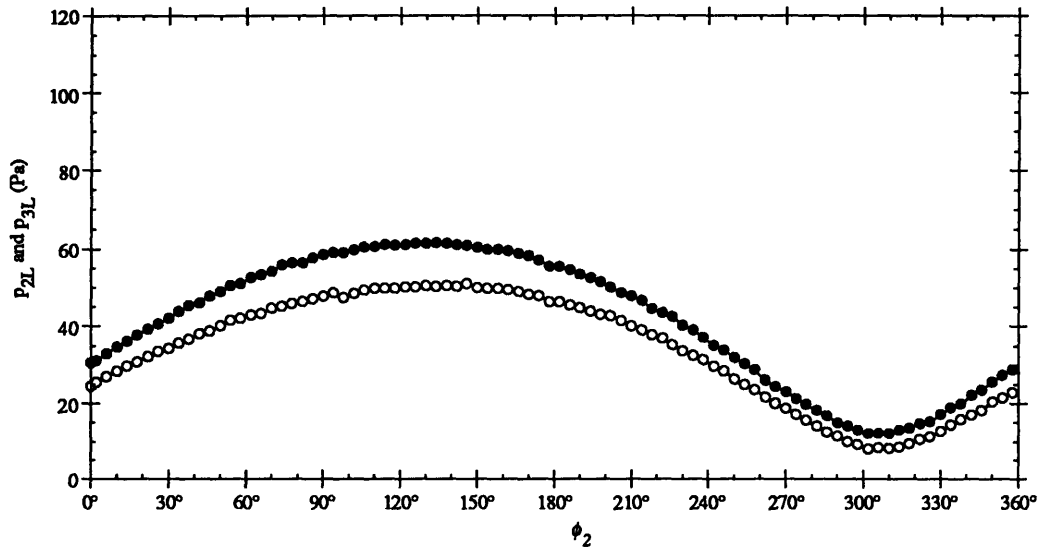
Figure 4.33 Experimental response amplitudes of the second and third harmonics.
Forcing amplitudes are $F_1=1.2$ g and $F_2=1.12$ g. The first forcing tone is fixed at frequency f_1
while a second forcing tone of frequency $2f_1$ and amplitude F_2 is applied and its phase relative to
the first tone, ϕ_2, swept from $0°$ to $360°$. p_{3L} (—O—) decreases along with p_{2L} (—●—), as expected.
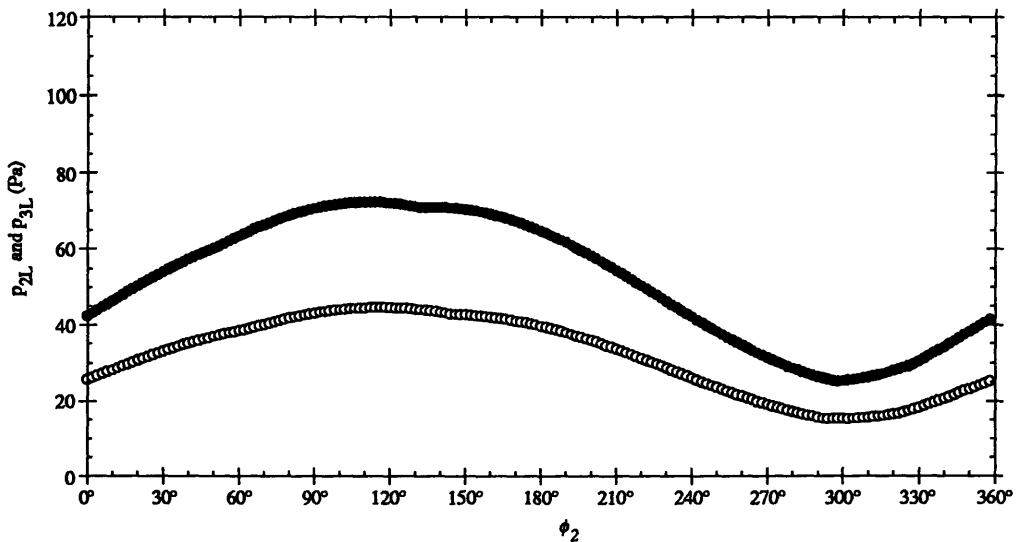*F_2 is too weak to quench p_{2L} totally.*

Figure 4.34 Modeled response amplitudes of the second and third harmonics.
Forcing amplitudes are $F_1=1.2$ g and $F_2=1.12$ g. p_{2L} (—●—) is larger than experimental values, but
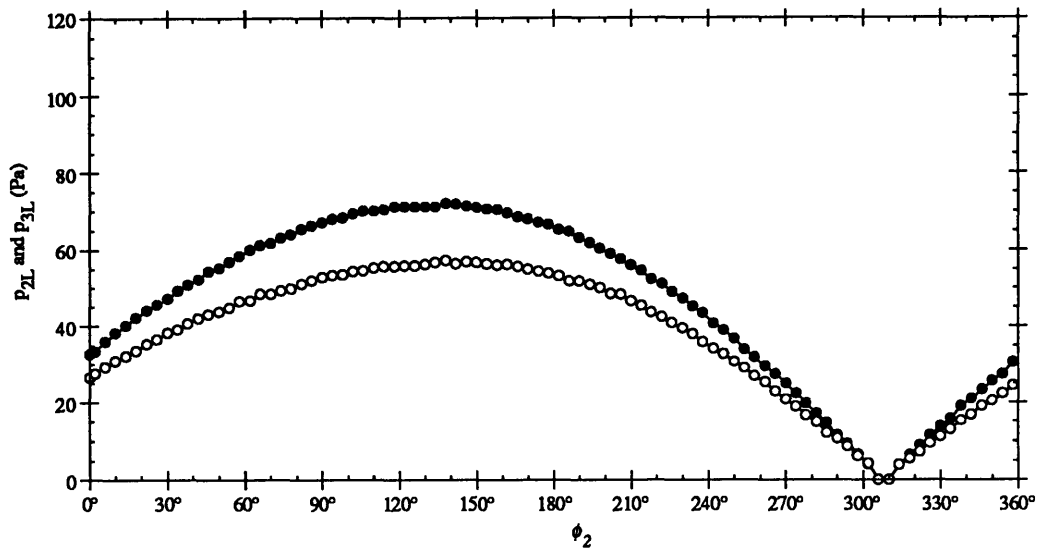*behavior is similar. —O—: p_{3L}.*

Figure 4.35 Experimental response amplitudes of the second and third harmonics.
Forcing amplitudes are $F_1=1.2$ g and $F_2=1.62$ g. Both p_{2L} (—●—) and p_{3L} (—○—) have been quenched
at $\phi_2 \approx 306°$. The increased F_2 also increased the constructive interference amplitude; compare p_{2L}
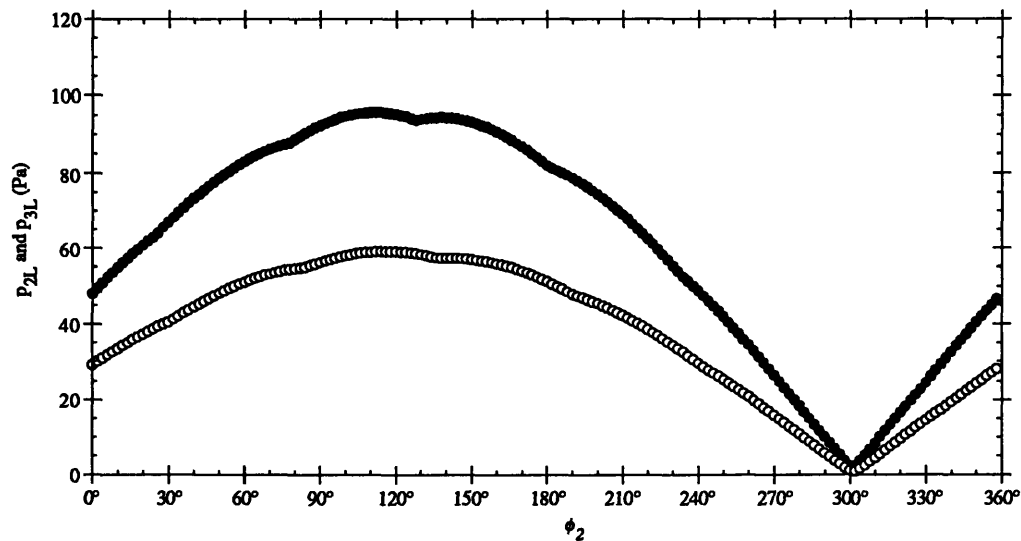*and p_{3L} at $\phi_2 \approx 130°$ to Fig. 4.33.*

Figure 4.36 Modeled response amplitudes of the second and third harmonics.
Forcing amplitudes are $F_1=1.2$ g and $F_2=2.23$ g. Both p_{2L} (—●—) and p_{3L} (—○—) have been
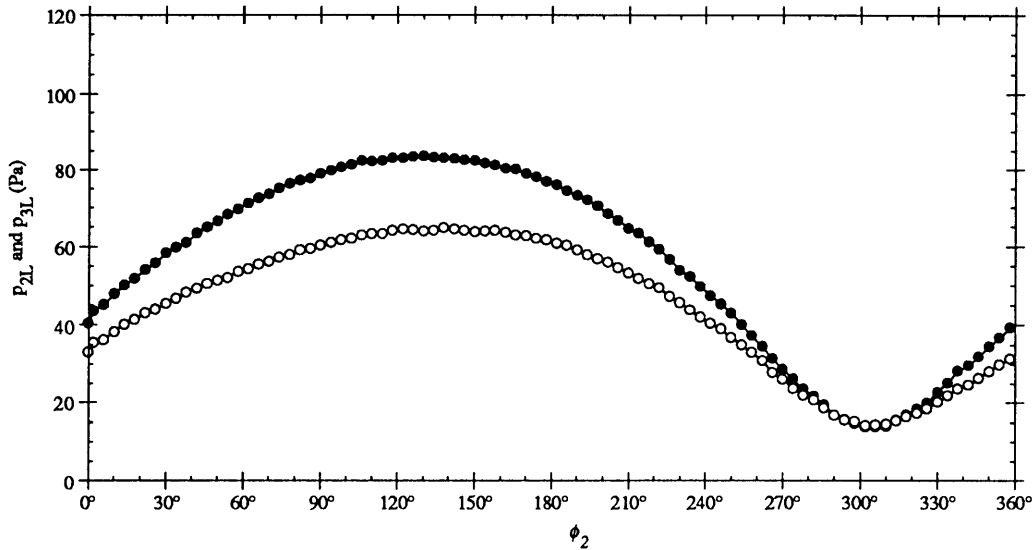*quenched. F_2 here is higher than the experimental F_2.*

Figure 4.37 Experimental response amplitudes of the second and third harmonics.
Forcing amplitudes are $F_1=1.2$ g and $F_2=2.24$ g. F_2 is too strong so that no value of ϕ_2 can quench p_{2L} (—●—) and p_{3L} (—O—).
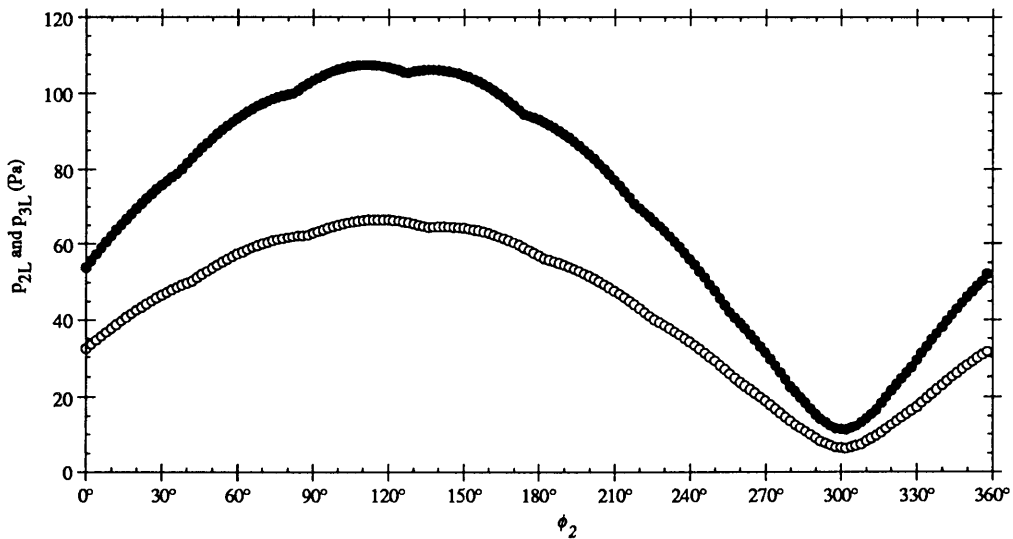

Figure 4.38 Modeled response amplitudes of the second and third harmonics.
Forcing amplitudes are $F_1=1.2$ g and $F_2=2.78$ g. F_2 is too strong so that no value of ϕ_2 can quench p_{2L} (—●—) and p_{3L} (—O—).

In Fig. 4.35, the second and third harmonics are totally quenched at ϕ_2=306°. The value of F_2 is 1.62 g and is lower than the computed value of 2.23 g (Fig. 4.36). If the value of F_2 is increased further to 2.24 g, then the quenching of p_{2L} and p_{3L} is not possible (Figs. 4.37 and 4.38). For all values of F_2, the preceding graphs have shown that although p_{2L} is the only harmonic being quenched, by quenching it, the other (higher) harmonics are also quenched.

p_{2L}'s for all three values of F_2 are graphed as a function of ϕ_2 in Figs. 4.39 and 4.40. For clarity, not all data points are delineated by symbols for the unquenched p_{2L} and p_{3L} curves, for both experimental and modeled results. In both experimental and computational setups, the results show that by increasing F_2, the maximum (at ϕ_2≈130°) of p_{2L} increases, but the minimum (at ϕ_2≈306°) first decreases to zero and then increases again. The same behavior is observed about p_{3L} in Figs. 4.41 and 4.42.

When p_{2L} and higher harmonics have been quenched, the leaking of energy from the first harmonic, p_{1L}, should have been minimized. p_{1L} should behave opposite to p_{2L} and p_{3L}, when p_{1L} is minimum, p_{2L} and p_{3L} should be maximum, and vice versa. The experimental p_{1L}'s for the three values of F_2 are graphed against ϕ_2 in Fig. 4.43. Although for each value of F_2, p_{1L} do go through a cycle like p_{2L} and p_{3L}, the maximum value of p_{1L} (ϕ_2≈230°) does not occur at where p_{2L} and p_{3L} are minimums (ϕ_2≈306°). Similarly, p_{1L} is minimum at ϕ_2≈60° whereas p_{2L} and p_{3L} are maximums at ϕ_2≈130°. The differences in ϕ_2 of $(p_{1L})_{maximum}$ and $(p_{1L})_{minimum}$ from $(p_{2L}$ and $p_{3L})_{minimum}$ and $(p_{2L}$ and $p_{3L})_{maximum}$ are both about 70°. The causes of the differences have not yet been determined.

Since the nonlinearly generated harmonics represent effective dissipation on the fundamental harmonic, from previous discussions, the value of the fundamental resonant frequency f_1 should increase as the amplitudes of the second and third harmonics decrease. Similarly, when p_{2L} and p_{3L} are at their maximum values, f_1 should be at its minimum. The values of f_1 as a function of ϕ_2 and F_2 are shown in Fig. 4.44. The vertical shifts in f_1 as F_2 is increased from $1g$ to $2g$ are due to temperature rises as each experiment was performed. Without effective nonlinear dissipation, f_1 should only increase due to the temperature rise, but f_1 does decrease as shown, and the cause must be related to the effective nonlinear dissipation (see Eq. 4.3 and the discussion following it). In fact, f_1, like p_{1L}, should also behave opposite to p_{2L} and p_{3L}.

Noting that the temperature rises during the phase sweep from $\phi_2=0°$ to $\phi_2=360°$, the behavior of f_1 due to nonlinear effects will be offset by a continuous tendency for the increasing temperature to increase f_1. In Fig. 4.44, f_1 decreases to a minimum at $\phi_2\approx130°$, or about the same angle at which p_{2L} and p_{3L} are at their maximums. The amount of decrease and increase in f_1 becomes more apparent as F_2 is increased because of the increased amounts of effective nonlinear dissipation in the system. When p_{2L} and p_{3L} are at their minimums, f_1 should have increased to a maximum. However, because the temperature continues to rise beyond $\phi_2=306°$, f_1 does not decrease appreciably and in fact, increases slightly. The increase of f_1 due to the temperature rise beyond $\phi_2=306°$ is more apparent at a low F_2 because of smaller effective nonlinear dissipation effects.

The preceding discussions have shown that given $F_1=1.2$ g, with the appropriate value of F_2, p_{2L} and p_{3L} (and higher harmonics) can be quenched at $\phi_2\approx306°$. With a higher value of F_1, however, p_{2L} may be quenched but a nonzero p_{3L} still remain. The remaining p_{3L} is the result of cubic nonlinear coupling, to be discussed in the next section. Here, two graphs of p_{2L} and p_{3L} corresponding to $F_1=1.78$ g and two values of F_2 show experimentally the *emergence* of cubic nonlinear coupling effects. In Fig. 4.45, the value of F_2 is 1.68 g and is insufficient to quench the second harmonic p_{2L}. In Fig. 4.46, $F_2=3.64$ g and is seen to quench p_{2L} at $\phi_2\approx306°$. However, p_{3L}, which was larger than p_{2L} before p_{2L} is quenched, reaches a minimum at $\phi_2\approx306°$, but not zero. The unquenched p_{3L} is the result of direct leakage of energy from the fundamental harmonic to the third harmonic, a cubic nonlinear coupling phenomenon.
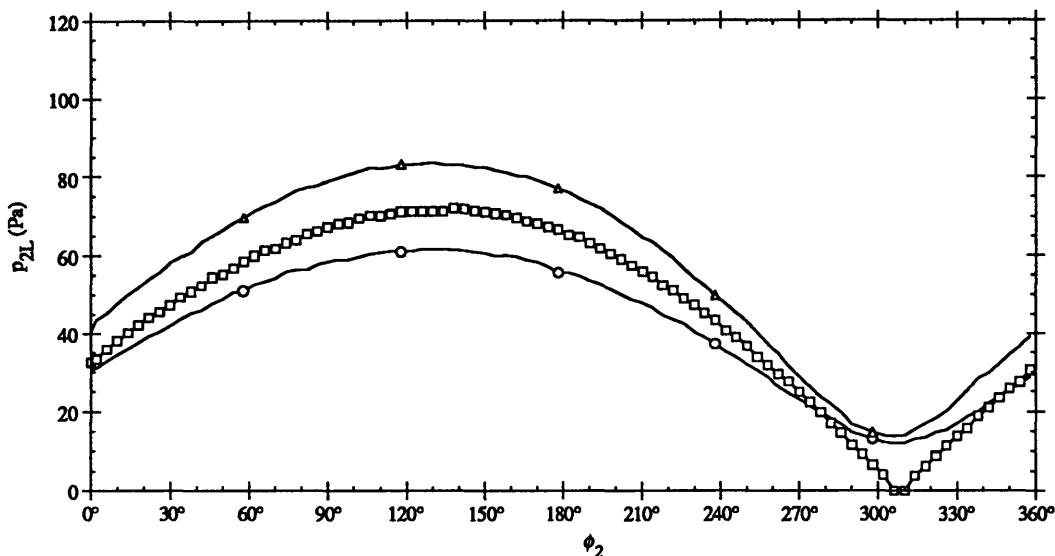
Figure 4.39 Experimental response amplitudes of the second harmonic.
Forcing amplitudes are $F_1=1.2$ g and $F_2=1.12$ g, 1.62 g, and 2.24 g. The maximum of p_{2L} increases with F_2, the minimum first decreases to zero, then increases again. $-O-$: $F_2=1.12$ g, $-\square-$: $F_2=1.62$ g, and $-\triangle-$: $F_2=2.24$ g. For clarity, not all data points are delineated by symbols for the $F_2=1.12$ g and 1.62 g curves.

Figure 4.40 Modeled response amplitudes of the second harmonic.
Forcing amplitudes are $F_1=1.2$ g and $F_2=1.12$ g, 2.23 g, and 2.78 g. $-O-$: $F_2=1.12$ g, $-\square-$: $F_2=2.23$ g, and $-\triangle-$: $F_2=2.78$ g. Not all data points are delineated by symbols for the $F_2=1.12$ g and 2.78 g curves.

Figure 4.41 Experimental amplitudes of the third harmonic.
Forcing amplitudes are $F_1=1.2$ g and $F_2=1.12$ g, 1.62 g, and 2.24 g. The maximum of p_{3L} increases with F_2, the minimum first decreases to zero, then increases again. $-\bigcirc-$: $F_2=1.12$ g, $-\square-$: $F_2=1.62$ g, and $-\triangle-$: $F_2=2.24$ g. For clarity, not all data points are delineated by symbols for the $F_2=1.12$ g and 1.62 g curves.
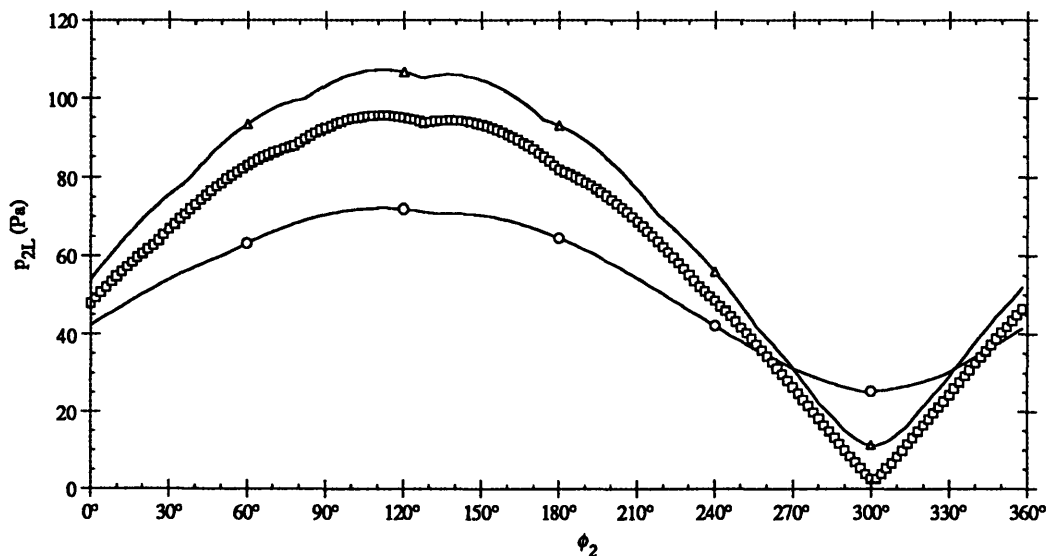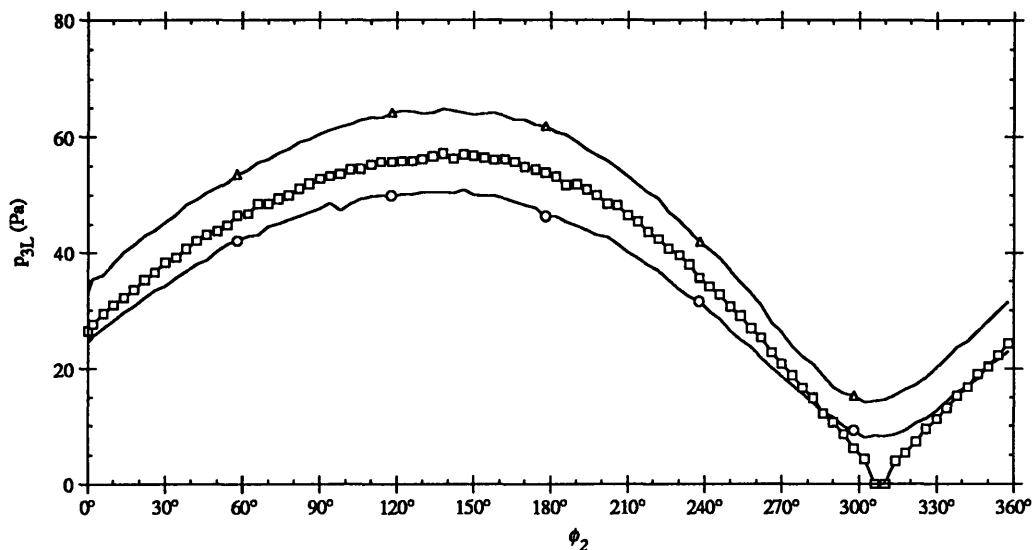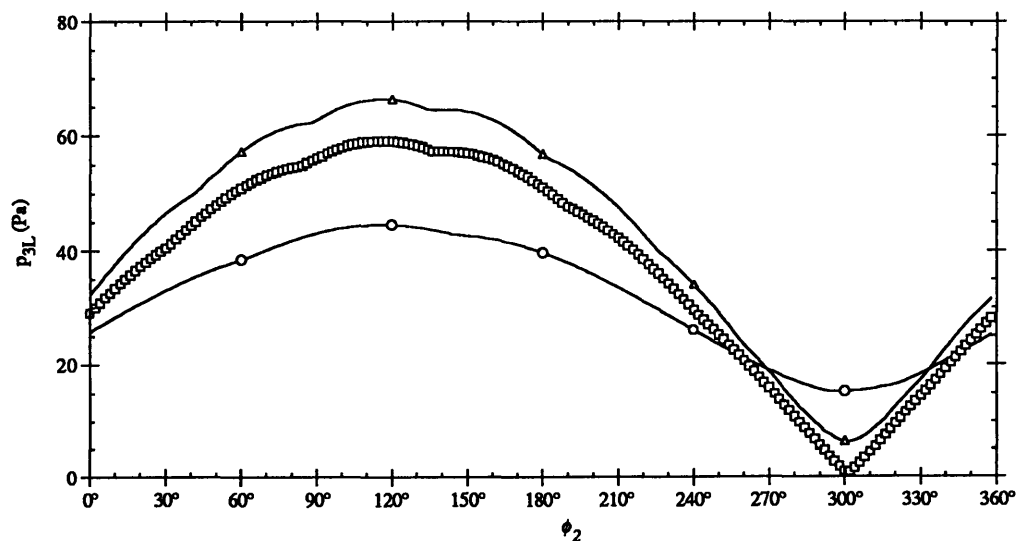

Figure 4.42 Modeled response amplitudes of the third harmonic.
Forcing amplitudes are $F_1=1.2$ g and $F_2=1.12$ g, 2.23 g, and 2.78 g. $-\bigcirc-$: $F_2=1.12$ g, $-\square-$: $F_2=2.23$ g, and $-\triangle-$: $F_2=2.78$ g. Not all data points are delineated by symbols for the $F_2=1.12$ g and 2.78 g curves.

114
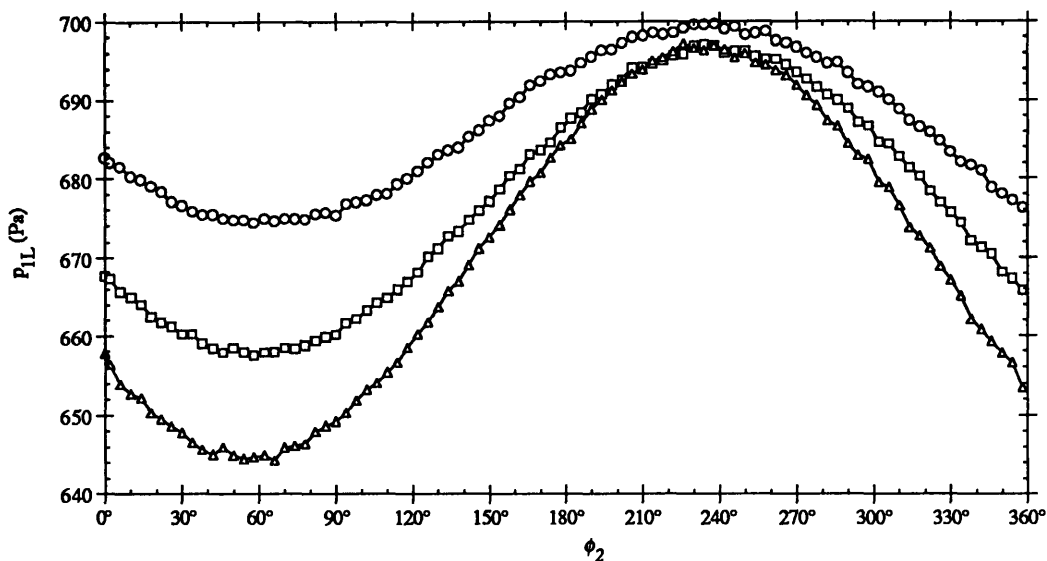
Figure 4.43 Experimental response amplitudes of the first harmonic
Forcing amplitudes are $F_1=1.2$ g and $F_2=1.12$ g, 1.62 g, and 2.24 g. p_{1L} goes through a cycle, like p_{2L} and p_{3L}, but not entirely opposite in trend as expected. -O-: $F_2=1.12$ g, -□-: $F_2=1.62$ g, and -△-: $F_2=2.24$ g.
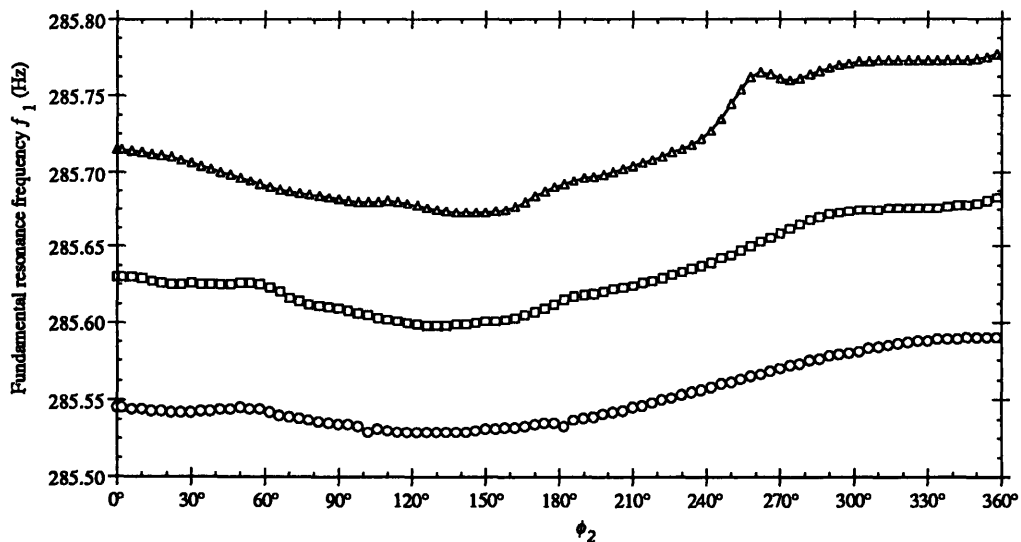

Figure 4.44 Experimental values of the resonant frequency.
Forcing amplitudes are $F_1=1.2$ g and $F_2=1.12$ g, 1.62 g, and 2.24 g. The behavior of f_1 is approximately opposite to the behavior of p_{2L} and p_{3L}; nonlinear effects present an effective dissipation which decreases the value of f_1. -O-: $F_2=1.12$ g, -□-: $F_2=1.62$ g, and -△-: $F_2=2.24$ g.

Figure 4.45 Experimental amplitudes of the second and third harmonics.
Forcing amplitudes are $F_1=1.78$ g and $F_2=1.68$ g. F_2 is too weak to quench p_{2L}. p_{3L} (—O—) is seen to be larger than p_{2L} (—●—) at all values of ϕ_2.

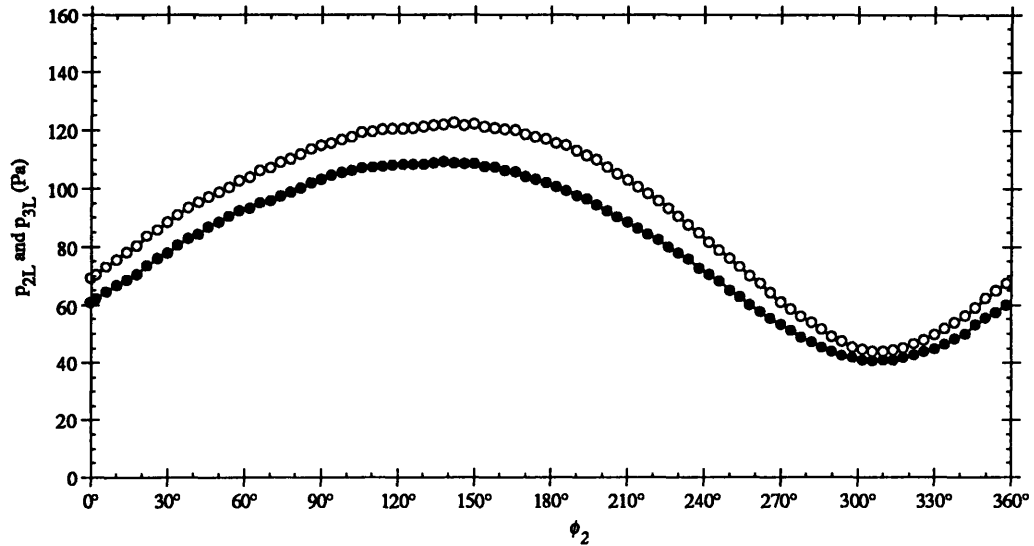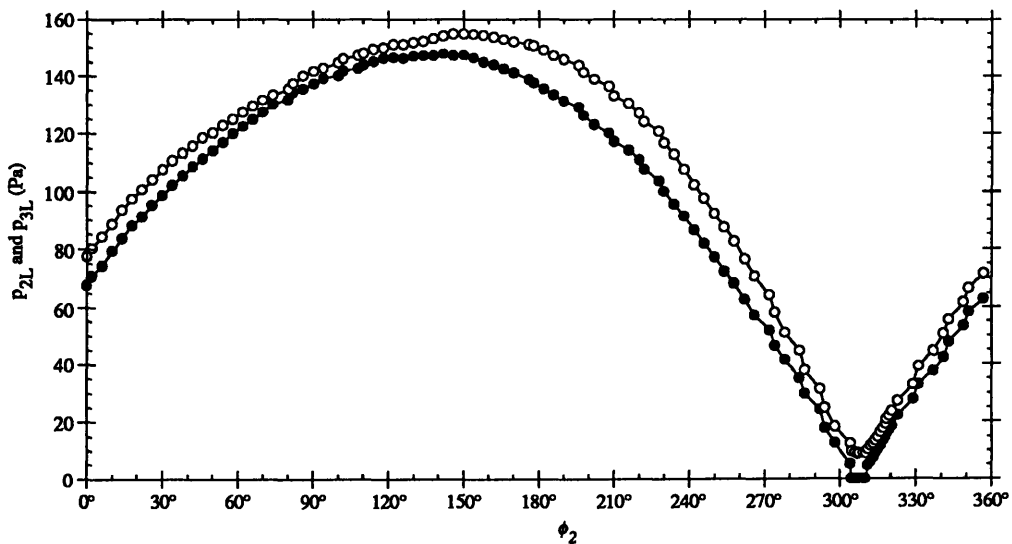*Figure 4.46 Experimental amplitudes of the second and third harmonics.*
Forcing amplitudes are $F_1=1.78$ g and $F_2=3.64$ g. Although p_{2L} (—●—) is quenched at $\phi_2 \approx 306°$, p_{3L} (—O—) is nonzero due to direct nonlinear coupling from the fundamental to the third harmonic- a cubic nonlinear coupling effect.

116

4.3.2 Cubic Nonlinear Coupling

The effective cubic nonlinear equation (ECNE) includes both quadratic and cubic nonlinear coupling effects:

$$\left(c_0^2 \nabla^2 - \frac{\partial^2}{\partial t^2} + \frac{\partial}{\partial t}\Im\right)\frac{p}{c_0^2} = -F_{dr} - \varepsilon_{quad}p^2 - \varepsilon_{cubic}p^3 . \tag{4.10}$$

When the forcing function F_{dr} consists of two forcing tones,

$$F_{dr} = \underbrace{F_1\sin(\omega_{dr}t)}_{F_{drI}} + \underbrace{F_2\sin(2\omega_{dr}t+\phi_2)}_{F_{drII}}, \tag{4.11}$$

where F_{drI} is the drive at the fundamental resonant frequency and F_{drII} is the drive at twice the fundamental resonant frequency, then with appropriate values of F_2 and ϕ_2, quadratic nonlinear effects ($\varepsilon_{quad}p^2$ in Eq. 4.10) are eliminated on average throughout the resonator. When quadratic nonlinear couplings effects are eliminated, Eq. 4.10 can effectively be rewritten as

$$\left(c_0^2 \nabla^2 - \frac{\partial^2}{\partial t^2} + \frac{\partial}{\partial t}\Im\right)\frac{p}{c_0^2} = -F_{dr}^* - \varepsilon_{cubic}p^3 , \tag{4.12}$$

where the forcing function F_{dr}^* is modified with a third tone at three times the fundamental resonant frequency, F_{drIII}, to quench cubic nonlinear coupling effects:

$$F_{dr}^* = \underbrace{F_1\sin(\omega_{dr}t)}_{F_{drI}} + \underbrace{F_3\sin(3\omega_{dr}t+\phi_3)}_{F_{drIII}} + \underbrace{\left[\underbrace{F_2\sin(2\omega_{dr}t+\phi_2)}_{F_{drII}} + \varepsilon_{quad}p^2\right]}_{Average\ cancellation},$$

$$F_{dr}^* = \underbrace{F_1\sin(\omega_{dr}t)}_{F_{drI}} + \underbrace{F_3\sin(3\omega_{dr}t+\phi_3)}_{F_{drIII}}. \tag{4.13}$$

The effective cubic nonlinear coupling coefficient, ε_{cubic}, was determined with the same procedure used to determine ε_{quad}. With the assumption that ε_{cubic} is a real-valued constant, the explicit form of ε_{cubic} is found to depend on the ratio of the empirical amplitudes of the third and fundamental harmonics, p_{3L}/p_{1L}^3:

$$\varepsilon_{cubic} = \left| \frac{4f_1^3(L)\left(\hat{k}_3^2 - k_3^2\right)}{f_3(L)\langle f_3(x)f_1^3(x)\rangle} \left(\frac{p_{3L}}{p_{1L}^3}\right)_{at\ f_1,\ p_{2L}\ quenched} \right|,$$ (4.14)

where p_{1L} and p_{3L} are the experimental amplitudes of the fundamental and third harmonic when the first forcing tone is fixed at the fundamental resonant frequency f_1 and the second harmonic p_{2L} has been quenched by an appropriate second driving tone, $f_1(x)$ and $f_3(x)$ are the first and third eigenfunctions, respectively, $\langle f_3(x)f_1^3(x)\rangle$ is the volume integral of $f_3(x)$ and $f_1^3(x)$, k_3 is the wave number of the third mode, and $\hat{k}_3$ is a function of the driving frequency $3\omega_d$ and dissipation.

Figs. 4.47 to 4.53 show the pressure profiles and the corresponding amplitude spectrums when the resonator is at the fundamental resonant frequency and the second harmonic has been quenched. Fourteen values of F_1, from 0.6 g to 2.16 g, were used to show how F_1 affected the amplitude and shapes of the responses. As these graphs show, as F_1 is increased, the increased response amplitude is accompanied by increasing nonlinearities, seen clearly in both the pressure profiles and the amplitude spectrums. When F_1=2.16 g, the amplitude of the second and third harmonic (Fig. 4.50) are seen to be about 10% of the fundamental harmonic, resulting in a very nonlinear pressure profile.

When an appropriate second forcing tone is applied to quench the second harmonic, Figs. 4.51 to 4.54 show the pressure profiles are once again sinusoidal. The corresponding amplitude spectrums show that for small values of F_1 ($\le$ 1.08 g), once the second harmonic is quenched, so are the higher harmonics. As F_1 increases, however, cubic nonlinear effects (e.g. the third harmonic) emerge and grow quickly. The amplitude spectrums also show that the third harmonic is interacting with the fundamental harmonic to generate a fourth harmonic, and the fourth harmonic interacting with the fundamental harmonic to generate a fifth harmonic. (The spike at 1500Hz is not a natural harmonic of the resonator system, it was generated by the computer analysis routine.) At F_1=2.16 g, the total acoustic pressure amplitude was about 155 dB (re 20 μPa) and although its pressure profile was very nonlinear initially, after the second harmonic was quenched, the profile is sinusoidal.

Figure 4.47 Pressure profile and amplitude spectrums, second harmonic not quenched. Forcing amplitudes are F_1=0.6 g to 0.96 g. The single driving tone's frequency is equal to the fundamental resonant frequency.

Figure 4.48 Pressure profile and amplitude spectrums, second harmonic not quenched. Forcing amplitudes are F_1=1.08 g to 1.44 g. The single driving tone's frequency is equal to the fundamental resonant frequency.

120

Figure 4.49 Pressure profile and amplitude spectrums, second harmonic not quenched.
Forcing amplitudes are $F_1=1.56$ g to 1.92 g. The single driving tone's frequency is equal to the
fundamental resonant frequency.

121

Chapter 4 Experimental and Computational Results

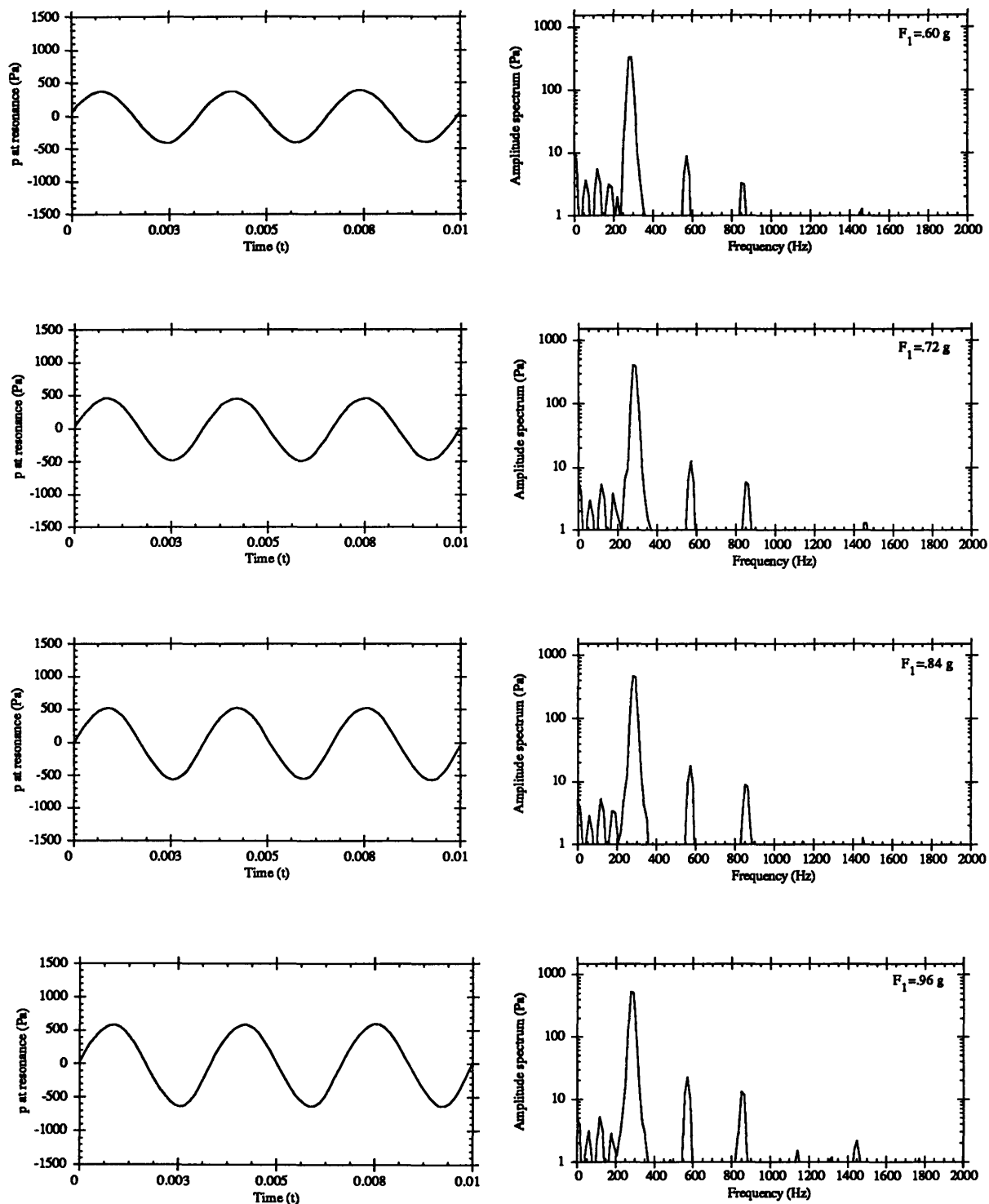

Figure 4.50 Pressure profile and amplitude spectrums, second harmonic not quenched.
Forcing amplitudes are F_1=2.04 g and 2.16 g. The single driving tone's frequency is equal to the fundamental resonant frequency.

Figure 4.51 Pressure profile and amplitude spectrums, second harmonic quenched.
Forcing amplitudes are F_1=0.6 g and 0.72 g, F_2=0.44 g and 0.59 g. A second tone of amplitude F_2, at twice the fundamental resonant frequency, is used to quench the second harmonic.

122

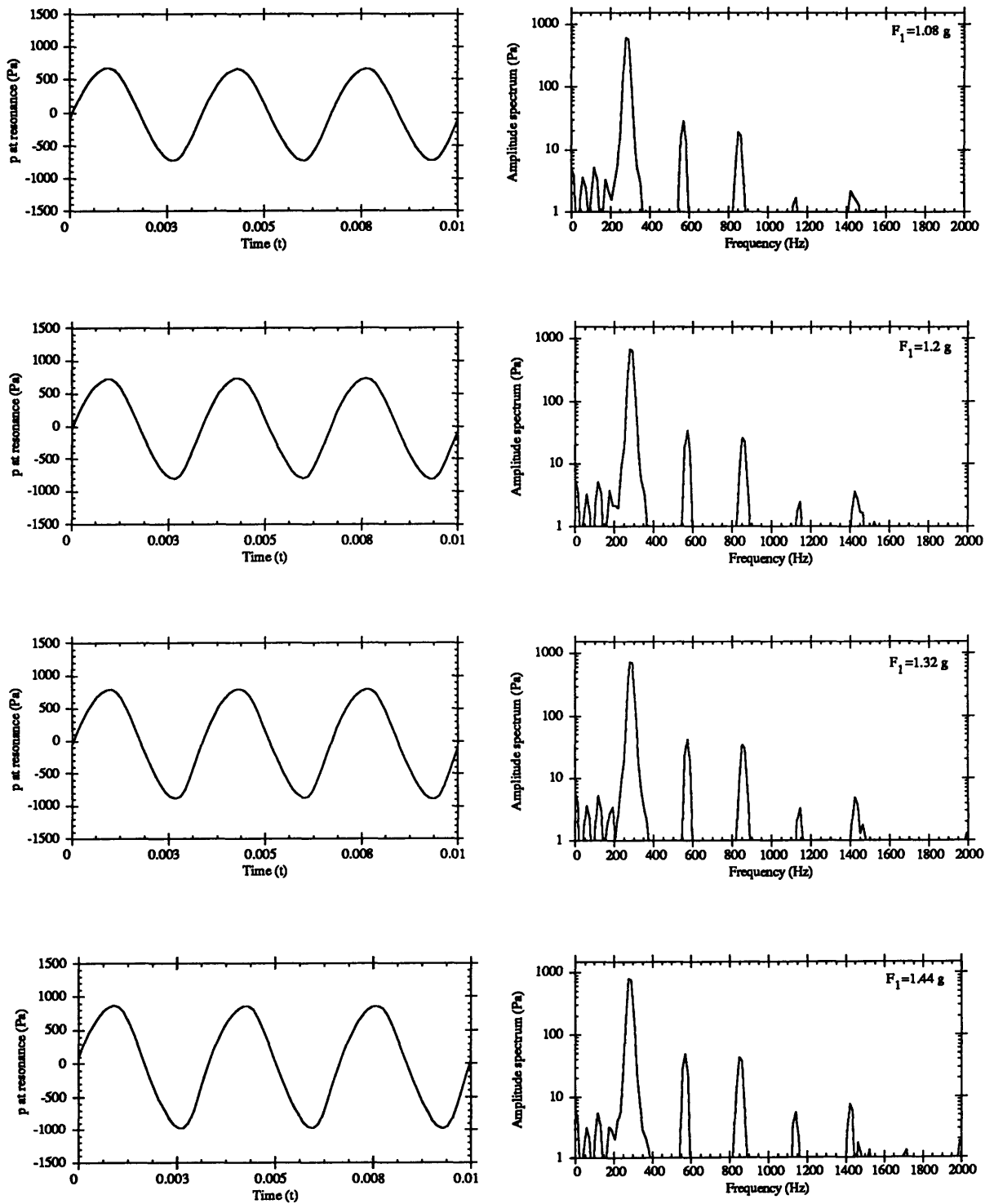*Figure 4.52 Pressure profile and amplitude spectrums, second harmonic quenched.*
Forcing amplitudes are $F_1=0.84$ g to 1.2 g, $F_2=0.80$ g to 1.66 g. A second tone of amplitude F_2,
at twice the fundamental resonant frequency, is used to quench the second harmonic.

123

Figure 4.53 Pressure profile and amplitude spectrums, second harmonic quenched.
Forcing amplitudes are $F_1=1.32$ g to 1.68 g, $F_2=1.99$ g to 3.18 g. A second tone of amplitude F_2,
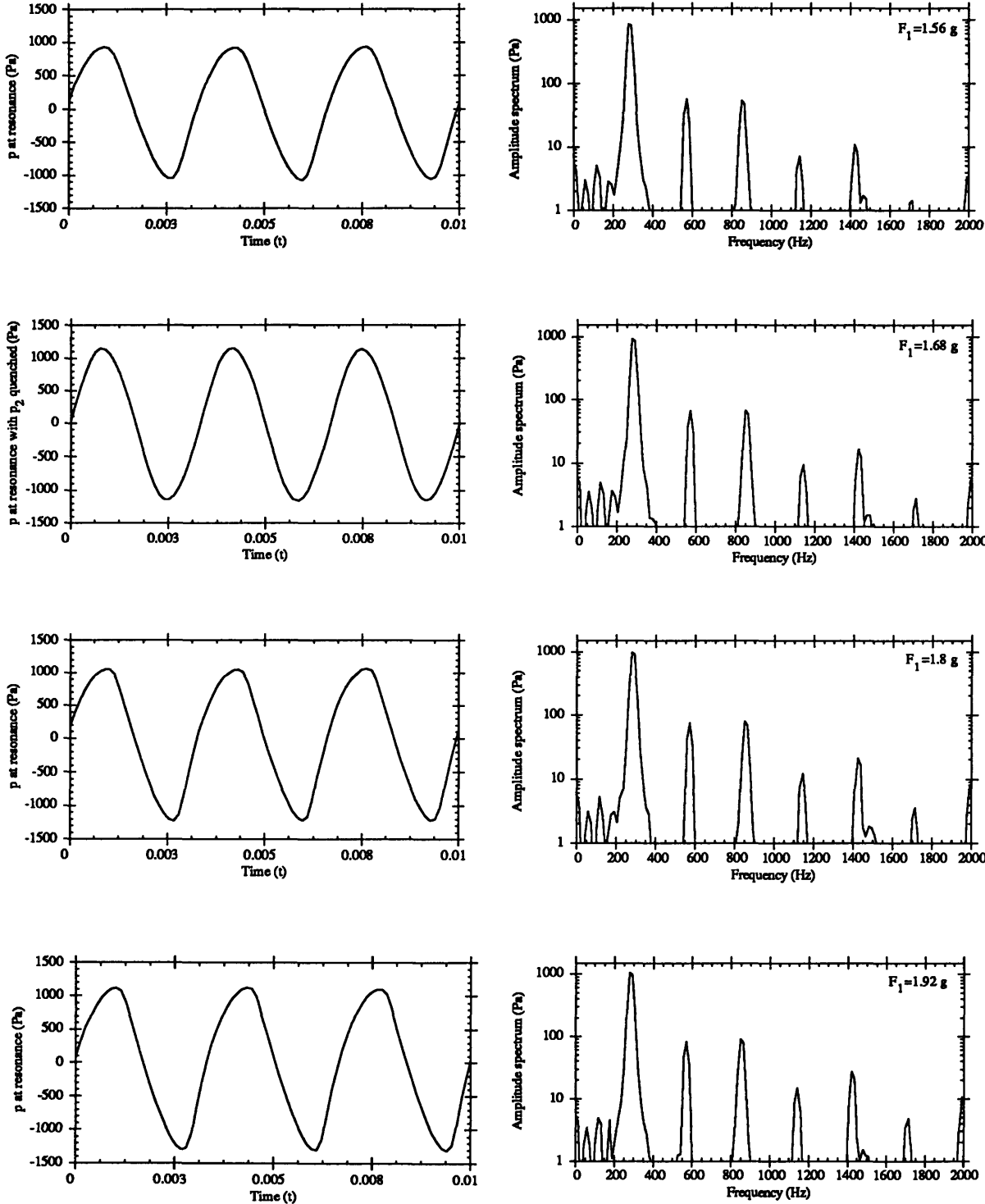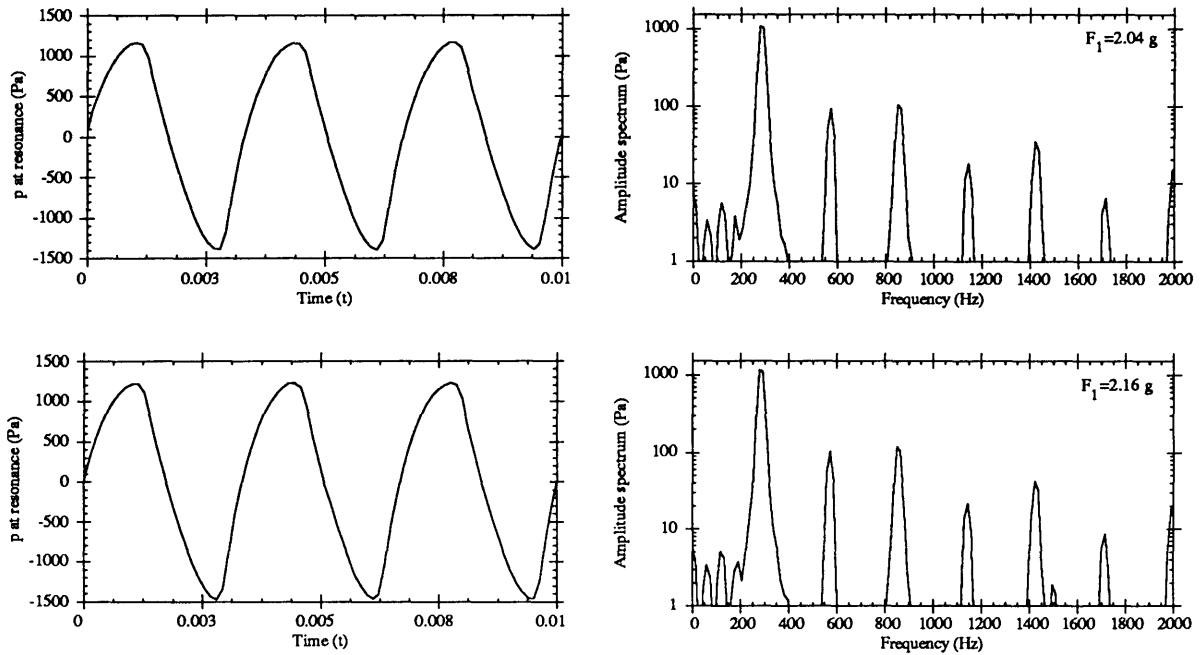*at twice the fundamental resonant frequency, is used to quench the second harmonic.*

124

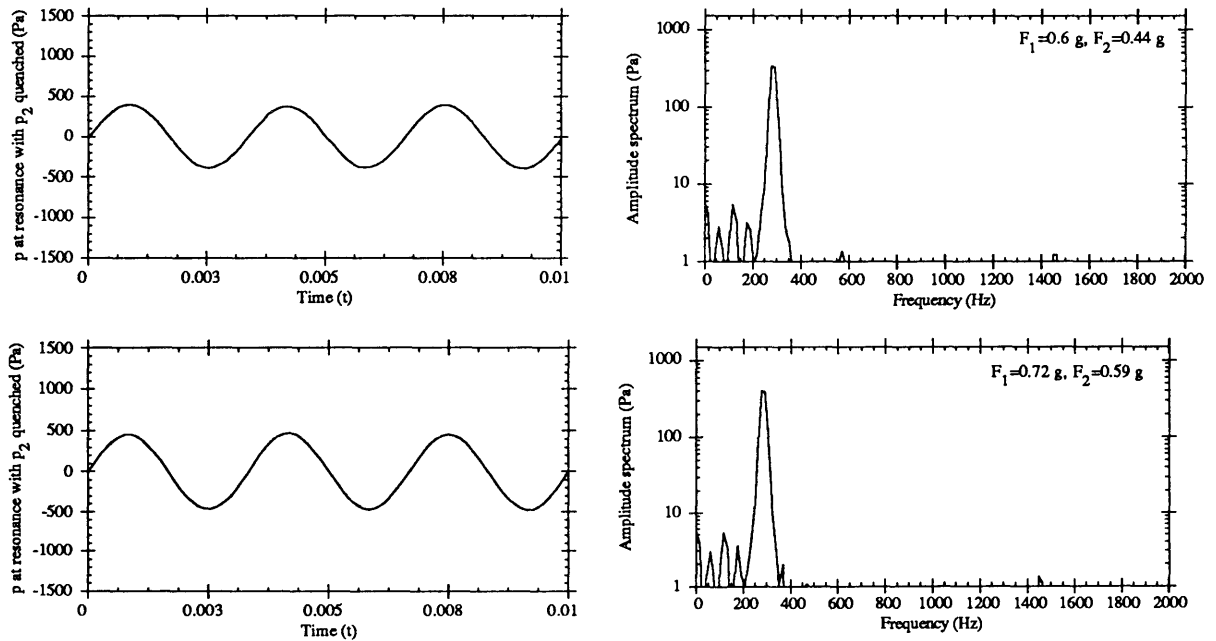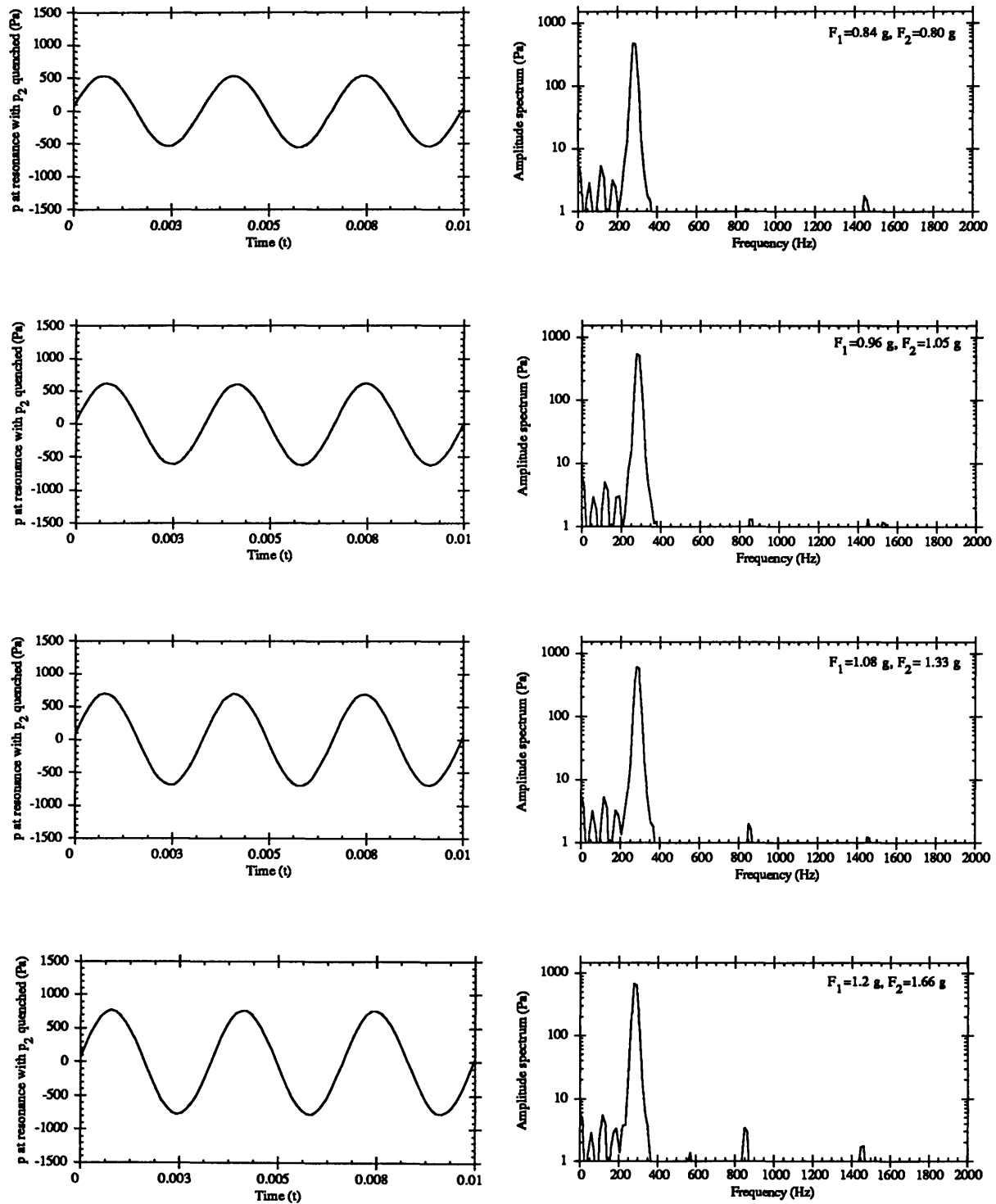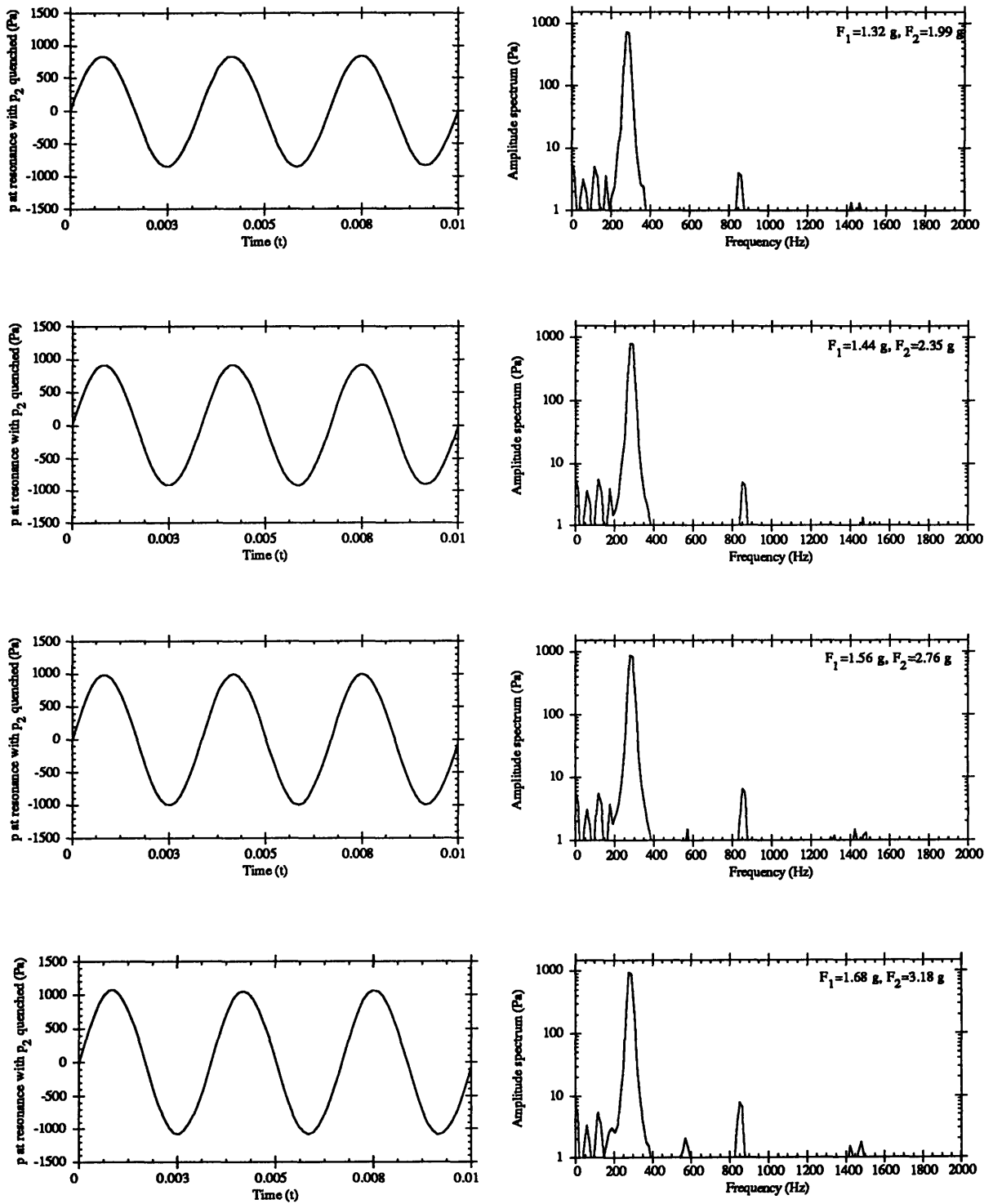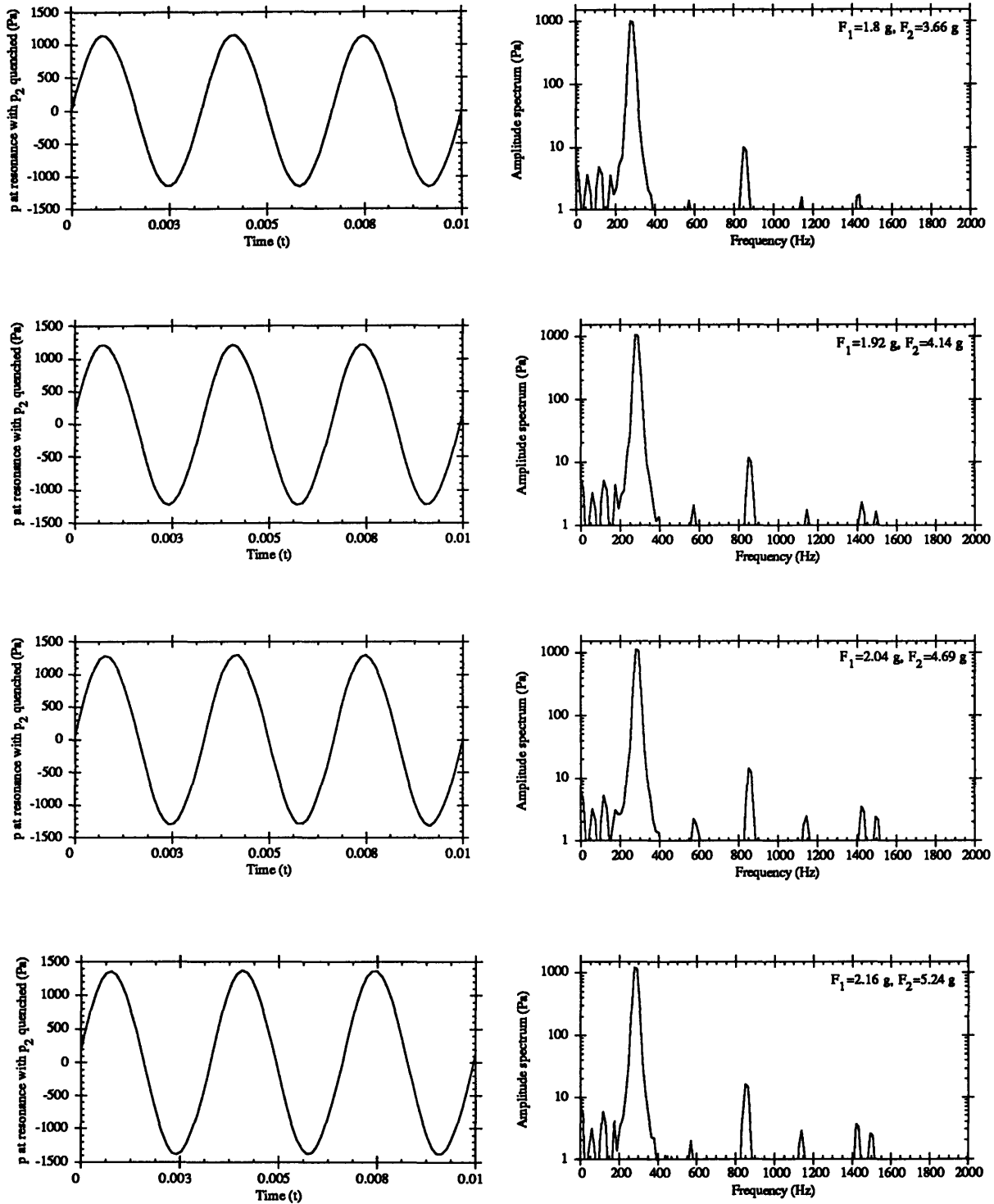*Figure 4.54 Pressure profile and amplitude spectrums, second harmonic quenched.
Forcing amplitudes are F_1=1.8 g to 2.16 g, F_2=3.66 g to 5.24 g. A second tone of amplitude F_2,
at twice the fundamental resonant frequency, is used to quench the second harmonic.*

125

In Fig. 4.55, the measured and modeled amplitudes of the second forcing tone required to quench the second harmonic are graphed as a function of the amplitude of the first forcing tone. Both measured and computed F_2's grow quadratically, but the measured values at a slower rate than the computed. One cause for this phenomena is that at large F_1's, the emergence of cubic nonlinear effects competes with quadratic nonlinear effects in extracting energy from the fundamental harmonic. Since less energy is extracted to the second harmonic, quenching it will not require as large of a F_2 as in the case when only quadratic nonlinear effects were present.

The amplitude of the cubically generated third harmonic and the ratio p_{3L} / p_{1L}^3 are shown in Fig. 4.56. The amplitude of the third harmonic is seen to grow approximately cubically with F_1, resulting in a relatively constant value for the ratio p_{3L} / p_{1L}^3. With the value of this ratio, the amplitude of the third forcing tone, F_3, can be calculated that would quench the third harmonic. The next section will show experimental results to when both the second and third harmonics have been quenched by the active control approach.
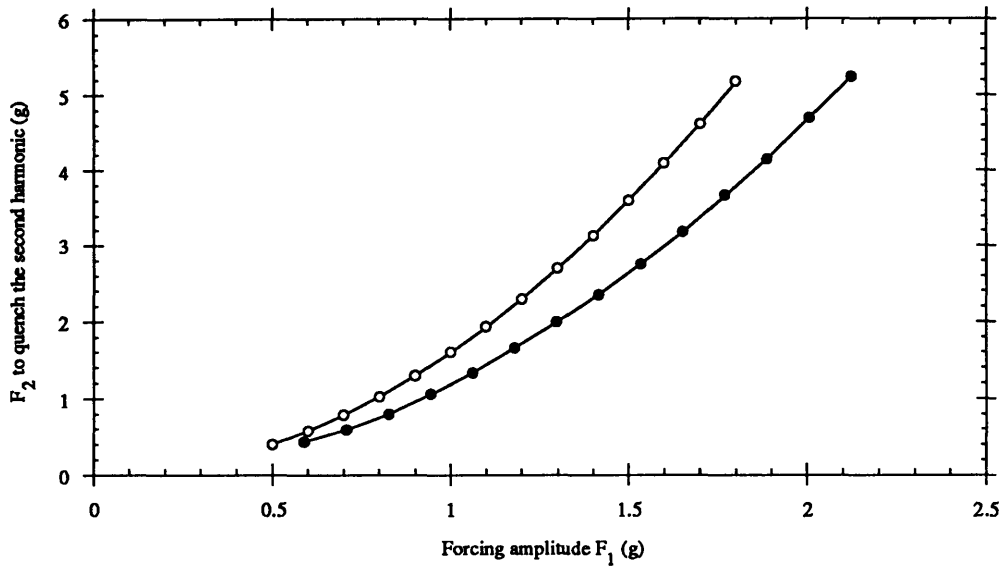
Figure 4.55 *Experimental and modeled second forcing tone amplitude to quench the second harmonic. Experimental values of F_2 (−●−) are smaller than modeled values of F_2 (−○−) because energy leakage from the first harmonic to the third harmonic is increasing faster than to the second harmonic as the first forcing tone amplitude F_1 increases.*
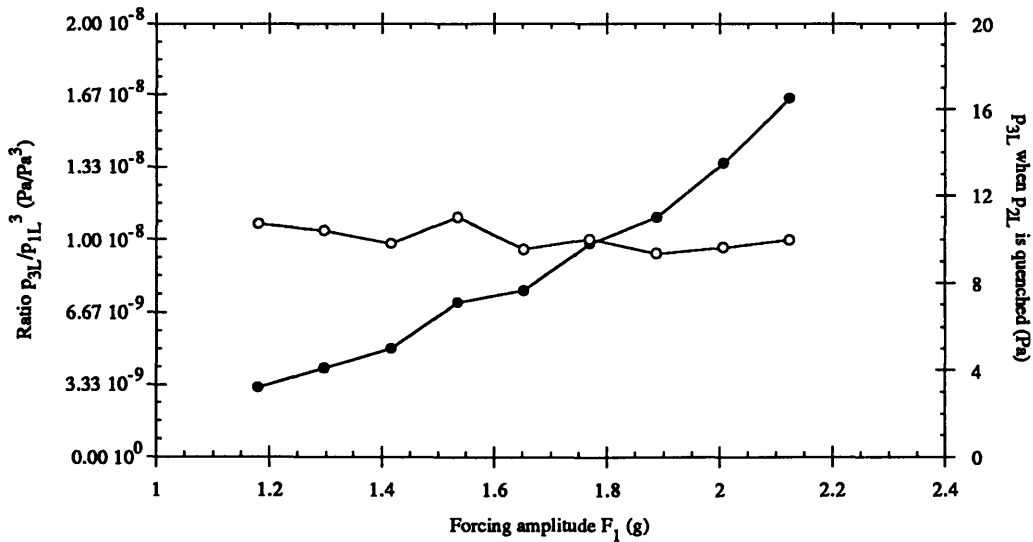
Figure 4.56 *Amplitude of the third harmonic generated by cubic effects, and the ratio p_{3L} / p_{1L}^3. When the second harmonic has been quenched, the remaining third harmonic p_{3L} (−●−, right scale) increases in amplitude as the cube of F_1. The ratio p_{3L} / p_{1L}^3 (−○−, left scale) remains approximately constant at 1×10^{-8} (Pa/Pa³).*

127

4.3.3 Quenching the Second and Third Harmonics

The value of F_3 was computed using the empirical data on p_{1L} and p_{3L}, when p_{2L} has been quenched by a second forcing tone of amplitude F_2. The ratio p_{3L}/p_{1L}^3 enabled the calculation of ε_{cubic}, whose value is computed to approximately $\varepsilon_{cubic} = 1.7 \times 10^{-7} \, s^4/kg$ Fig. 4.57 shows the behavior of F_3, which, like F_2, can be written as

$$F_3 = F_{3,const} F_1^3, \tag{4.15}$$

where $F_{3,const}$ is a constant of unit g^{-2} that depends directly on ε_{cubic}. $F_{3,const}$ is found to be about $0.022 \, g^{-2}$, compared to $1.6 \, g^{-1}$ for $F_{2,const}$. Although the units of $F_{2,const}$ and $F_{3,const}$ are not the same, with the values of F_1 investigated ($F_1 \le 2 \, g$), the small value of $F_{3,const}$ means that the direct cubic nonlinear coupling effects are weak. Thus, in an amplitude spectrum, the amplitude of the third harmonic, when only one forcing tone at f_1 is driving the resonator, is mainly the result of quadratic nonlinear coupling effects. For $F_1 = 2.16 \, g$, the value of the third harmonic (Fig. 4.54), when the second harmonic is quenched, is about 16 Pa. This is only about 13% of the full amplitude of the third harmonic (120 Pa) when the second harmonic is not quenched (Fig. 4.50).

In Fig. 4.57, the computed value of F_3 to quench cubic nonlinear effects, given $F_1 = 1.8 \, g$, is about $0.126 \, g$. The experimental amplitudes of the third harmonic as a function of the relative phase angle between the first and third forcing tones, ϕ_3, are shown in Fig. 4.58. Three values of F_3 were applied: $0.033 \, g$, $0.080 \, g$, and $0.164 \, g$. The behavior of the third harmonic with ϕ_3 and F_3 is similar to the behavior of the second harmonic with ϕ_2 and F_2 discussed in Section 4.3.1. The value of ϕ_3 at which the amplitude of the third harmonic is quenched is about 308° and $F_3 = 0.080 \, g$ is about 35% lower than the computed $0.126 \, g$.

Figs. 4.59 and 4.60 each show three sets of pressure profiles and amplitude spectrums corresponding to: a single forcing tone at f_1, two forcing tones at f_1 and $2f_1$ that quench the second harmonic, and, three forcing tones at f_1, $2f_1$ and $3f_1$ that quench both the second and third harmonics. The amplitudes of the first forcing tone are $1.8 \, g$ in Fig. 4.59, and $2.16 \, g$ in Fig. 4.60. For both values of F_1, the active control approach was used successfully in quenching both quadratic and cubic nonlinear coupling effects by first quenching the second harmonic and then the third harmonic.

F1 (g)	F3 (g)
1.0	0.02166
1.1	0.02883
1.2	0.03743
1.3	0.04759
1.4	0.05944
1.5	0.07310
1.6	0.08872
1.7	0.10642
1.8	0.12632
1.9	0.14857
2.0	0.17328

$$F_3 = (0.022 \text{ g}^{-2}) * F_1^3$$

$$(\varepsilon_{cubic} = 1.75 \times 10^{-7} \text{ s}^4/\text{kg})$$
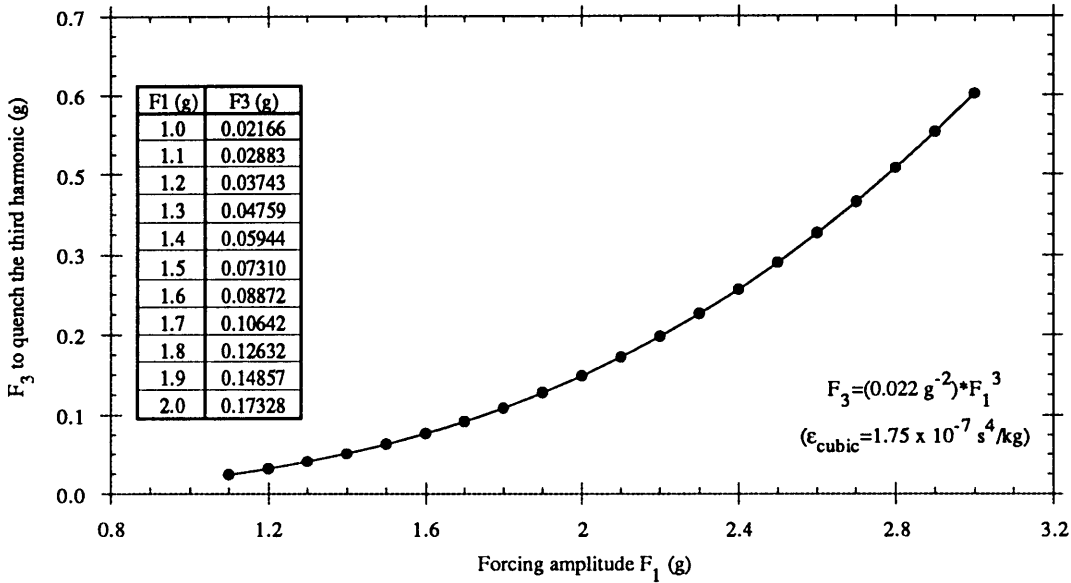
Figure 4.57 Computed third forcing tone amplitude to quench the third harmonic.
In this range of the first forcing tone amplitude, $1.0 \text{ g} \leq F_1 \leq 3$ g, cubic nonlinear effects are small, thus the third forcing tone amplitude F_3 (—●—) needed to quench the third harmonic are small (in the absence of quadratic coupling through the second harmonic).
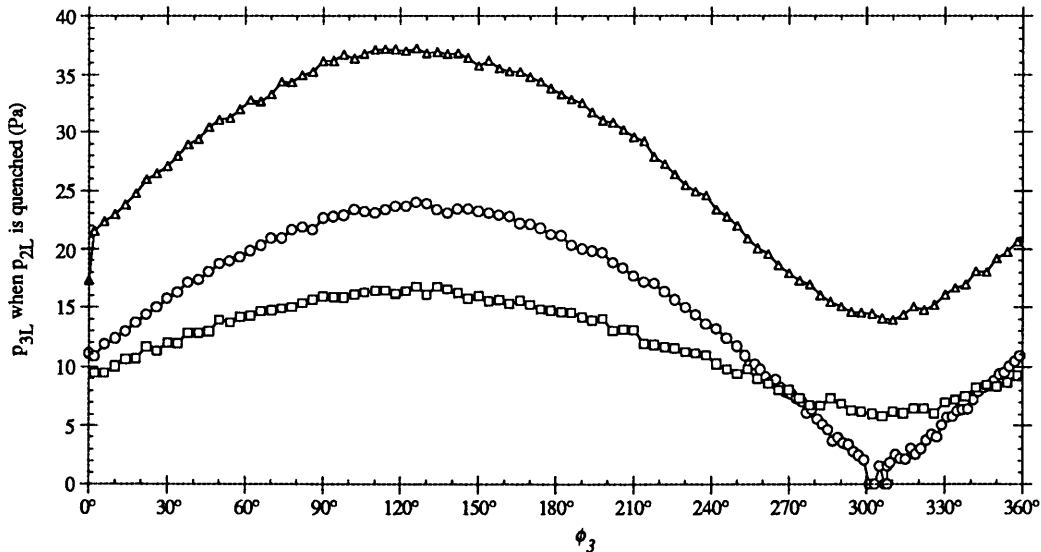
Figure 4.58 Experimental response amplitudes of the third harmonic, the second harmonic is quenched. Forcing amplitudes: $F_1 = 1.8$ g, $F_2 = 3.76$ g (to quench the second harmonic), and $F_3 = 0.033$ g, 0.080 g, and 0.164 g. The first forcing tone is fixed at f_1, the second forcing tone at $2f_1$, and the third forcing tone at $3f_1$. ϕ_3 is relative phase between the third and the first forcing tone. —□—: $F_3 = 0.033$ g, —○—: $F_3 = 0.080$ g, and —△—: $F_3 = 0.164$ g.

129
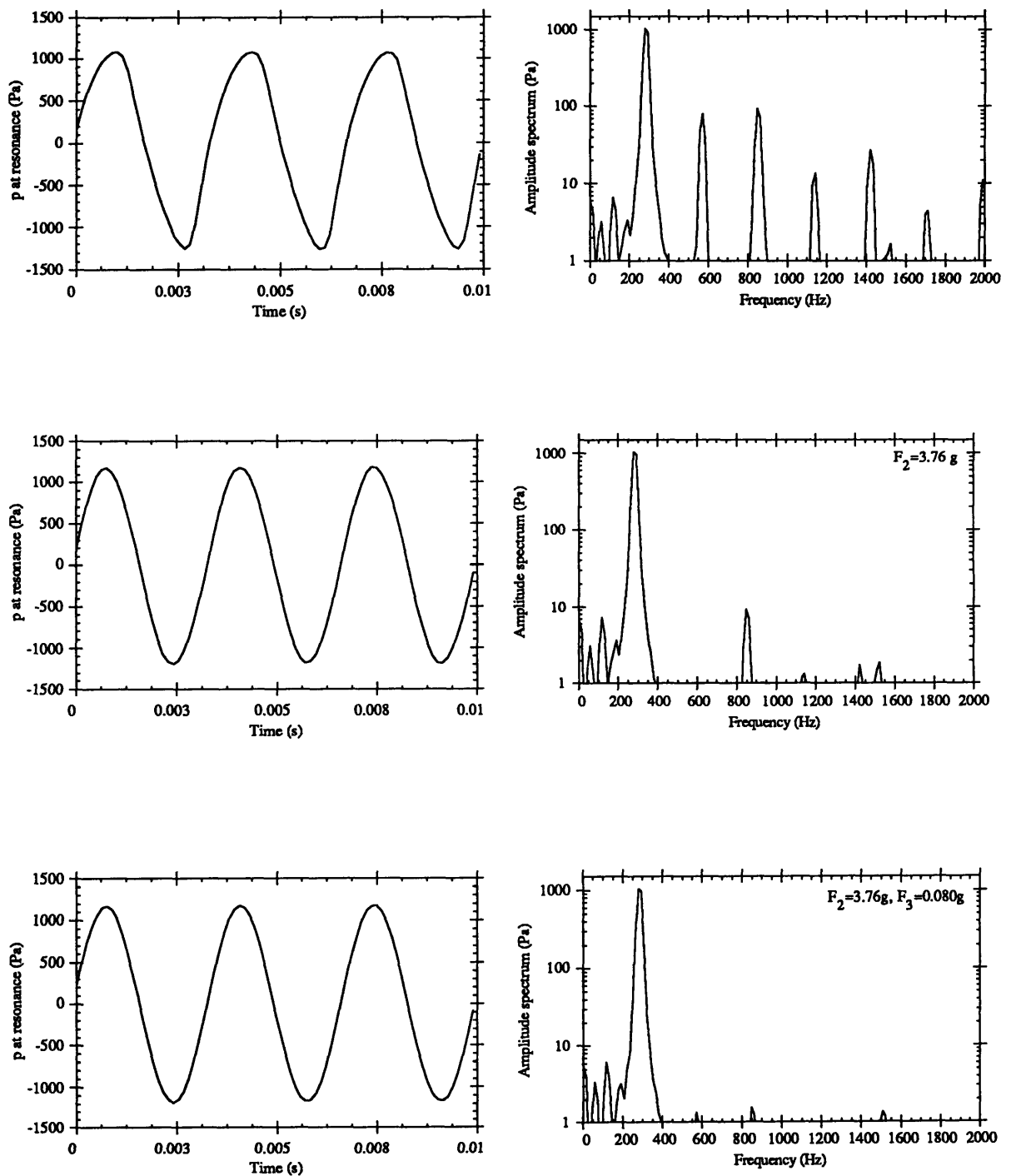
Figure 4.59 Pressure profile and amplitude spectrums, quenching the second and third harmonics. Forcing amplitude is $F_1=1.8$ g. Top: single tone at the fundamental resonant frequency, middle: the second harmonic is quenched by a second tone of amplitude F_2, and bottom: the third harmonic is quenched by a third tone of amplitude F_3.

130
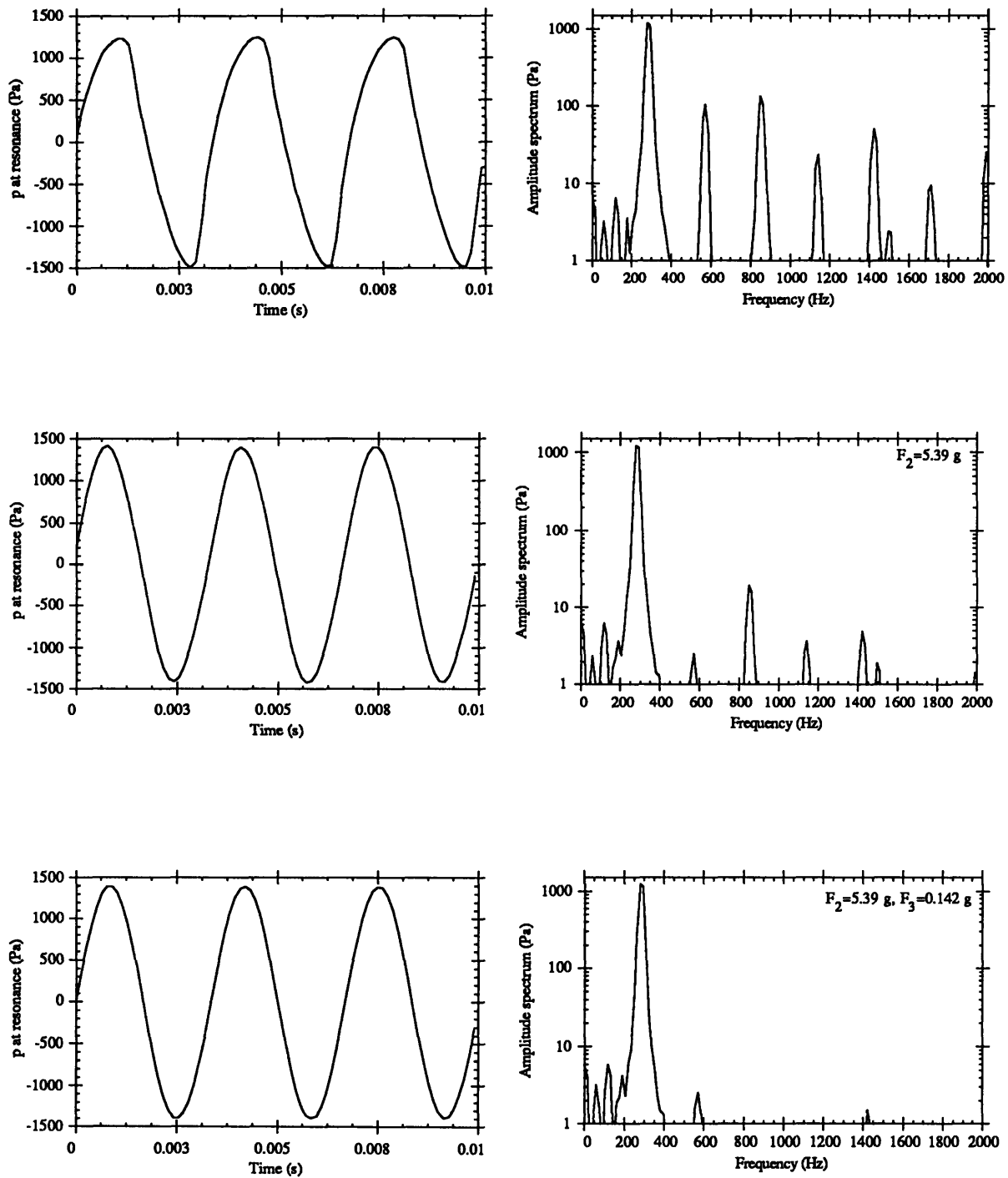
Figure 4.60 Pressure profile and amplitude spectrums, quenching the second and third harmonics. Forcing amplitude is $F_1=2.16$ g. Top: single tone at the fundamental resonant frequency, middle: the second harmonic is quenched by a second tone of amplitude F_2, and bottom: the third harmonic is quenched by a third tone of amplitude F_3.

131

4.3.4 Controlling Arbitrary Harmonics

In previous discussions, the active control approach had been used to first quench the second harmonic, and then to quench the third harmonic. In such a sequence, the effective nonlinear coupling coefficients, ε_{quad} and ε_{cubic}, were measured. The active control approach can also be applied to quench or amplify any individual harmonic. By noting the responses of the other harmonics around the harmonic being quenched or amplified, coupling effects among the harmonics can be directly observed. In Fig. 4.61, the third and fourth harmonics are each individually quenched.

When the third harmonic is quenched, the higher (fourth and up) harmonics are seen to decrease to small values. This observation confirms the quadratic nonlinear coupling model where, without the third harmonic, the fourth harmonic cannot be readily generated. The energy transfer path is blocked off at the third harmonic (the third order solution to EQNE, $p^{(3)}$, shown in Fig. 2.2) and higher harmonics are suppressed. The interaction of the second harmonic with itself is of higher order and does not produce an appreciable fourth harmonic because of the TRR design.

When the fourth harmonic is quenched, interaction between the second and third harmonic generate the fifth harmonic. The newly generated fifth harmonic then interacts with the first three harmonics to generate the sixth, seventh, and eighth harmonics. Depending on the strengths of the interactions, some harmonics may not be of significant amplitudes. In Fig. 4.61, the fifth harmonic is clearly present whereas higher harmonics are negligible in amplitude.
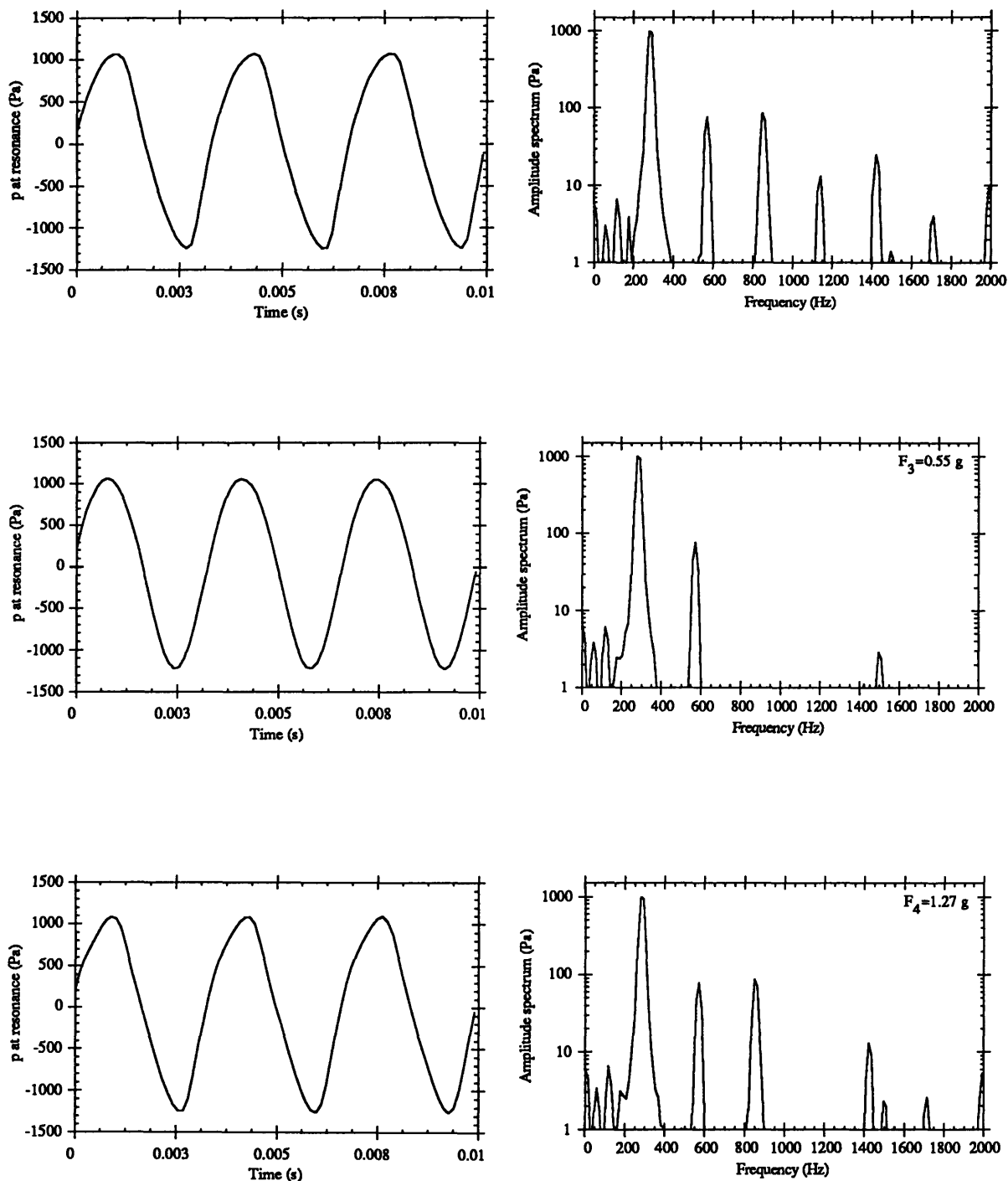
Figure 4.61 Pressure profile and amplitude spectrums, quenching arbitrary harmonics.
Forcing amplitude is $F_1=1.8$ g. Top: response to single forcing tone at f_1, middle: quenching the third harmonic blocks energy transfer to higher harmonics, bottom: quenching the fourth harmonic.

133

Figure 4.62 Pressure profile and amplitude spectrums, two-harmonics interaction.
Forcing amplitude is $F_1=1.2$ g. Top: response to single forcing tone at f_1, middle: quenching the second harmonic results in single response - fundamental harmonic, bottom: interaction between the first and third harmonics.
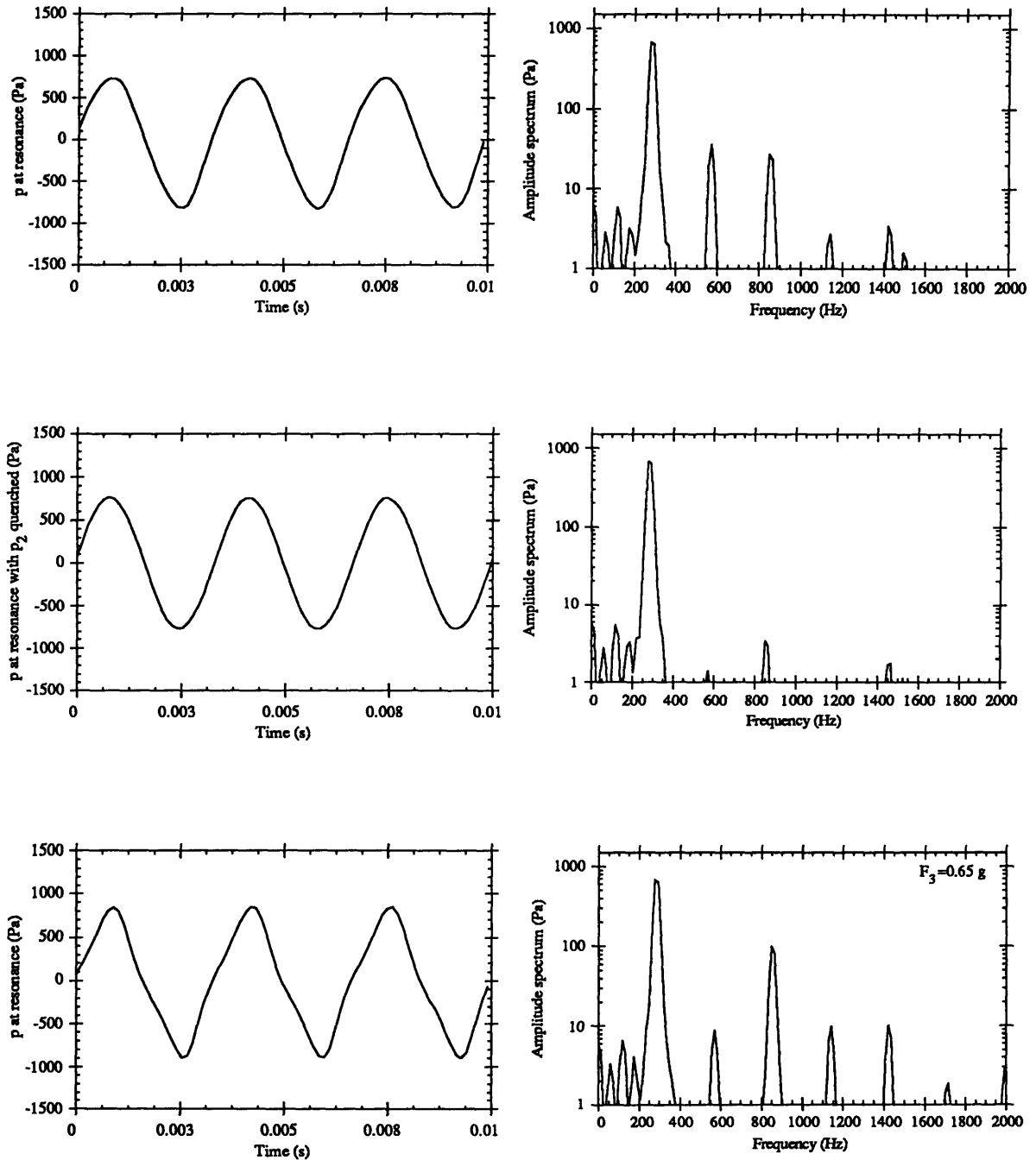
134
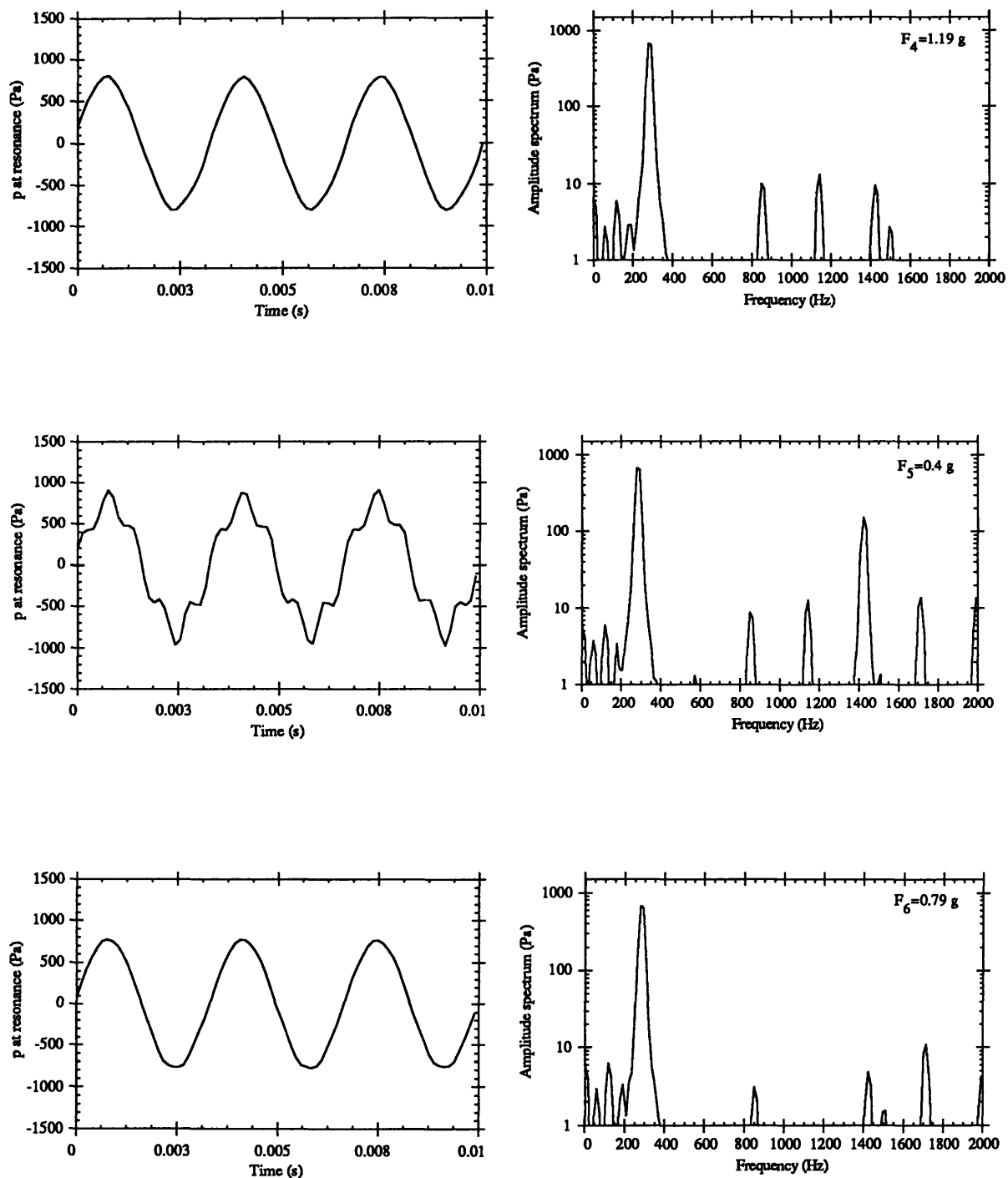
Figure 4.63 Pressure profile and amplitude spectrums, two-harmonics interaction.
Forcing amplitude is $F_1=1.2$ g. Top: interaction between the first and fourth harmonics, middle: interaction between the first and fifth harmonics, bottom: interaction between the first and sixth harmonics

Another method of observing interactions between two harmonics is shown in Figs. 4.62 and 4.63. First, the amplitude of the first forcing tone is kept low (F_1=1.2 g) so that cubic nonlinear coupling effects are small (Fig. 4.62, top two graphs). A second forcing tone is then applied to quench the second harmonic and the result is an essentially linear response - the fundamental harmonic (Fig. 4.62, middle two graphs). Interaction between the fundamental and another harmonic can be easily observed by introducing the second harmonic with a third forcing tone with frequency nf_1 ($n \geq 3$). In Fig. 4.62, the bottom two graphs show that the interaction between the fundamental and third harmonic generated the second and fourth harmonic - the difference and sum of the initial two harmonics, respectively. The fifth harmonic is also visible and is the result of the interaction between the second and third harmonics.

In Fig. 4.63, the interaction between the fundamental and the fourth harmonic is observed first, followed by the interaction between the fundamental and the fifth harmonic, and finally, the interaction between the fundamental and the sixth harmonic. The sum and difference harmonics have clearly been generated in each set of interactions. Subsequent interactions among the generated and existing harmonics help to generate even more harmonics, as seen in the middle two graphs of Fig. 4.63.

This section (4.3.3) consisted of all experimental results in graphical form, quantitative analysis of these results have not yet been performed. Proposed future work on the active control approach and conclusions will be discussed in the next chapter.

Chapter 5 Conclusions

R results presented in this thesis prove the feasibility of the active control approach in suppressing nonlinearly generated harmonics. The active control approach was also shown to be useful in measuring and understanding the interactions between modes. This chapter will summarize the findings of the current research efforts, discuss some of the problems encountered, and suggest areas of interest and importance for future work.

5.1 Summary

An empirical model was developed to model the nonlinear response of an acoustic resonator. The required empirical data included the actual resonant frequencies f_n's and quality factors Q_n's measured in a linear-amplitude response regime, and the amplitudes of the fundamental and second (nonlinearly generated) harmonic (p_1 and p_2) in a finite-amplitude response regime where the quadratic nonlinear coupling effects dominate.

The model was based on the effective quadratic nonlinear wave equation, EQNE, where the small-amplitude data were used to determine an effective quadratic nonlinear coupling coefficient, ε_{quad}. Although most of the results presented were based on this model, a more complete model which included cubic nonlinear coupling effects was also discussed. In this more extensive model using the ECNE (effective quadratic *and* cubic nonlinear wave equation), the amplitude of the third (nonlinearly generated) harmonic p_3, when the second harmonic has been quenched, was required in determining the effective cubic nonlinear coupling coefficient, ε_{cubic}.

137

Chapter 5 Conclusions

Resonator Design and the Forcing Function

A harmonic two-radii resonator (TRR) was chosen to demonstrate the quenching effects more clearly. Quenching nonlinearly generated harmonics in a harmonic resonator was found to be no more difficult than in an anharmonic resonator. The reason is that the amplitude of the nonlinearly generated second harmonic and the amplitude of the quenching harmonic driven by a second forcing tone are both dependent on the factor $\left(\hat{k}_2^2 - k_2^2\right)^{-1}$. When the value of this factor changes, say due to a temperature change that changes k_2, both harmonic amplitudes will change by the same amount, resulting in no net change if the sum of the two amplitudes was *zero* initially. The amplitudes of the harmonics generated by nonlinear effects in the TRR, however, are much larger than in an anharmonic resonator. Thus the TRR was chosen to demonstrate the quenching effects more clearly.

The area ratio between the two ends of the TRR, S_r, determined how much power can be coupled into the second mode of the resonator, in order to quench the nonlinearly generated second harmonic. The larger the ratio, the more power can be coupled to drive the second mode. The ratio used in this experiment was S_r=1.86 (11.04 in^2/5.94 in^2).

The forcing function was modeled computationally as a set of Dirac-delta functions at the three locations of the pistons. This model worked well since the actual displacement of the pistons was usually less than 5 μm. The actual forcing amplitudes were found using an accelerometer mounted on the resonator to be 9% to 20% higher than the specified forcing amplitudes defined in the LabVIEW virtual instruments (VI's). To avoid confusion, all results presented herein have been based on actual forcing amplitudes. There were also phase offsets between the measured and specified signals due to phase lags in the vibrator and the vibrator amplifier. At the fundamental resonance, the offset is about -10°, while at the second resonance, the offset is about 10°, and at the third resonance, about 20°. These phase offsets were included in the computational model as part of the forcing functions.

Response Through the First Three Resonant Frequencies

When working within the small-amplitude linear regime, the computed pressure response amplitudes to a single-tone forcing function F_1 was found to match well that of measured response amplitudes. However, the model underestimated the response amplitudes significantly at the second and third resonances, by about 17% and 35%,

138

respectively (Fig. 4.29). The cause of the deviations may be related to the boundary conditions and other assumptions used in the model, further studies on the deviations are needed.

The actual values of the resonant frequencies were found to be smaller than the computed values. The main reason for the differences is the simple boundary condition assumptions used in the model. Another reason is that the room temperature at any given day may be a few degrees more or less than any other day, resulting in overall resonant frequency shifts. Thus, instead of recalculating the resonant frequencies each time, the more important resonant frequency ratios n_r's, measured experimentally, were imposed into the model. Another cause for the actual resonant frequencies to be smaller than the computed values is the effective nonlinear "dissipation", which extracts energy from the first harmonic into the higher harmonics. Such an extraction of energy is more evident when the forcing amplitude is larger and affects the quality factor of the fundamental resonance, Q_1, by making it and therefore the resonant frequency f_1 smaller. Experiments showed that Q_1 decreased from about 180 to 140 as the forcing amplitude F_1 was increased from 0.36 g to 3.6 g. The decrease in Q_1 then prompted a decrease in the fundamental resonant frequency f_1. Other forms of effective dissipation must also be present because the calculated differences of the measured to computed resonant frequencies due to decreases in Q_1 were found to be smaller than the measured differences. A more thorough investigation of the types and strengths of effective dissipation present in the resonator system is desirable.

Harmonics Generation by Nonlinear Effects

Measurements of the amplitudes of the harmonics generated by nonlinear effects were performed by an amplitude spectrum analysis on the pressure response signal. The modeled response amplitudes of each of the first three harmonics as a function of a single forcing tone (driving the resonator at the fundamental resonant frequency f_1 and variable forcing amplitude F_1), were found to match well with measured response amplitudes when the forcing amplitude F_1 was small (Fig. 4.32). The modeled response amplitude of the first harmonic was about 10% higher than measured values at F_1=0.5 g, but the over-estimation increased to about 20% at F_1=2.0 g. Similarly, the modeled response amplitude of the second harmonic is about 20% higher than measured values at F_1=0.75 g, and almost 60% at F_1=2.0 g. For the third harmonic, the modeled response amplitude matched very well with experimental values up to about F_1=1.75 g, the differences between the two

being less than 5%. Overestimation by the model is over 30% when F_1=2.3 g and continues to grow at an increasing rate. The growth of the modeled response amplitudes is faster because the effective dissipation (transfer of energy) to higher harmonics was not included in the model. Thus, with large values of F_1 ($\geq$1.5 g), some assumptions made for the computational model are no longer applicable and correction factors must be introduced.

The value of ε_{quad} was determined from the ratio between the measured amplitudes of the first and second harmonics: $\varepsilon_{quad} \propto p_{2L}/p_{1L}^2$, where p_{1L} and p_{2L} are the amplitudes of the first and second harmonics, respectively, measured at the right-end of the resonator ($x=L$). The forcing frequency is equal to the fundamental resonant frequency. The ratio p_{2L}/p_{1L}^2 decreased slightly with the forcing amplitude F_1 because as F_1 increases, the third harmonic p_{3L} extracts more and more energy from the lower two harmonics, especially the second. The value of ε_{quad} used in the experiments corresponded to F_1=1.2 g, where $p_{3L} \ll p_{2L}$, and was calculated as about ε_{quad}=0.0013 $s^2/kg \cdot m$.

Quenching the Second and Third Harmonics

In theory, quenching the second harmonic stops the generation of all higher harmonics in the case when only quadratic nonlinear coupling effects exist. If cubic nonlinear coupling effects also exist, then the third harmonic will also need to be quenched in order to eliminate all nonlinearly generated harmonics. The research presented in this thesis has clearly shown the validity of the theory by use of the active control approach. Given the responses to a single-tone forcing function, the computational model successfully calculated the forcing amplitude of the second forcing tone F_2 necessary to quench the second harmonic. For the given resonator design, the relationship between F_2 and F_1 was determined to be $F_2 = (1.6g^{-1})F_1^2$, where the constant 1.6 g^{-1} was directly dependent on ε_{quad}. The computed F_2's were larger than the measured values, especially for large F_1's because ε_{quad} was assumed constant when it actually decreases slightly with F_1 (about a 7.5% decrease in ε_{quad} from F_1 =0.5 g to F_1 =1.5 g).

As the value of F_1 was increased while actively quenching the second harmonic, the third harmonic mode began to be excited due to cubic nonlinear coupling effects. Cubic nonlinear coupling directly couples energy from the fundamental to the third harmonic. To quench cubic nonlinear coupling effects, a third forcing tone is introduced to quench the third harmonic after the second has already been quenched. The amplitude of the third forcing tone F_3 can be determined once ε_{cubic} is known. ε_{cubic} was determined to depend on

p_{3L}/p_{1L}^3, where p_{1L} and p_{3L} are the empirical amplitudes of the first and third harmonics. The value of ε_{cubic} computed was about $1.7 \times 10^{-7} \ s^4/kg$, and the relationship between F_3 and F_1 was determined to be $F_3 = (0.022g^{-2})F_1^3$. The small value of the constant 0.022 g^{-2} suggested that cubic nonlinear effects ($\varepsilon_{cubic}p^3$) were indeed much smaller than quadratic nonlinear effects ($\varepsilon_{quad}p^2$) in the range of F_1 investigated. Experimental results have shown that quenching both the second and third harmonics virtually eliminated all higher harmonics, resulting in very clean, sinusoidal pressure profiles. The actual values of F_3 to quench the third harmonic were found to be lower than the calculated values by about 35%. The phase between the third and first forcing tones, ϕ_3, was not calculated beforehand but was experimentally found to be about the same as ϕ_2, at 300°.

Controlling Specific Harmonics

The last sections of Chapter 4 demonstrated that the active control approach could be used to measure coupling coefficients among the harmonics. The first of two methods to measure coupling coefficients is to quench a particular harmonic and to see what effect that has on the other harmonics. The second method is to first quench most of the harmonics so that only the fundamental harmonic remains. The user then introduces another tone of interest and observes how this harmonic interacts with the fundamental harmonic. For example, the interaction between the third harmonic and the first harmonic was shown to generate the sum and difference harmonics - the second and fourth harmonics. In turn, the second and third harmonics interact to generate the fifth harmonic. Similar observations were made on interactions between other combinations of harmonics.

5.2 Conclusions and Future Work

The active control approach has been shown to be effective in quenching nonlinearly generated harmonics as well as in investigating the coupling effects among the various harmonics. Much work remain to extend this research to practical applications. The basic concepts, however, have been shown to work as theorized, in both the computational model and experimental setups. The following briefly state the conclusions and suggestions for future work.

5.2.1 Conclusions

- Amplitudes of nonlinearly generated harmonics can be determined using the effective quadratic nonlinear wave equation, EQNE. This is a semi-empirical equation that models quadratic nonlinear effects by an effective forcing term: $\varepsilon_{quad}p^2$, where ε_{quad} is the effective quadratic nonlinear coupling coefficient and p is the total acoustic pressure. The model is currently limited to computing the first three harmonics.

- The effective quadratic nonlinear coupling coefficient in the EQNE was determined with empirical data on the amplitudes of the fundamental and second harmonics when the resonator is driven at its fundamental resonant frequency. The value of ε_{quad}, assumed real and positive, was determined as a constant, $\varepsilon_{quad}=0.0013 \ s^2/kg \cdot m$.

- The amplitudes of the first three harmonics were computed and compared to experimental values. In each case, the computed values grow faster than the actual values because effective nonlinear dissipation (energy leaked) from each of the harmonics to higher harmonics had been neglected.

- Using the model, the forcing amplitude F_2 needed to quench the second harmonic was computed to be related to the first forcing tone amplitude by: $F_2=(1.6 \ g^{-1})F_1^2$. Applying the active control approach to the experiment setup, actual values of F_2 were found to be slightly lower than computed values.

- Cubic nonlinear coupling effects could be observed and measured after the second harmonic was quenched. Cubic nonlinear effects were clearly visible when $F_1>1.44 \ g$.

- Introducing another effective forcing term to the EQNE results in a quadratic and cubic nonlinear wave equation, ECNE. The additional forcing term is $\varepsilon_{cubic}p^3$, where ε_{cubic} is the effective cubic nonlinear coupling coefficient.

- Harmonics generated by the ECNE were not modeled but ε_{cubic} was experimentally determined to be about $1.75 \ x \ 10^{-7} \ s^4/kg$.

- The forcing amplitude F_3 to quench the third harmonic was computed and compared with experimental values. The computed values were higher than experimental values by about 35% and can be expressed as: $F_3 = (0.0022g^{-2})F_1^3$. Cubic nonlinear effects were found to be much smaller than quadratic nonlinear effects in the range of F_1 probed (0.36 g to 2.4 g).

- The active control approach were used to observe interactions among different harmonics.

5.2.2 Suggestions for Future Work

Theory/ modeling

- Append computational model to account for current discrepancies found between computed and measured values of the amplitudes of the harmonics, especially the higher harmonics. The sources of dissipation need to be investigated more thoroughly.

- Develop *theoretical* expressions for the effective nonlinear coupling coefficients, $\varepsilon_{quad}, \varepsilon_{cubic}$, etc. Current expressions of these coefficients depend on empirical data on amplitudes of the harmonic responses.

- Develop expressions for coupling coefficients among the harmonics.

Experimental

- Compute the actual amount of energy extracted from the fundamental harmonic to higher harmonics.

- Improve and further develop the current feedback system.

- Design and test an anharmonic resonator.

Bibliography

Atchley, A. A., et al. "Development of Nonlinear Waves in a Thermoacoustic Prime Mover." *Frontiers of Nonlinear Acoustics: Proceedings of 12th ISNA.* Elsevier Science Publishers Ltd., London, 1990. Edited by M. F. Hamilton and D. T. Blackstock. p603 - 608.

Beyer, R. T. *Nonlinear Acoustics.* Department of the Navy: 1974.

Beyer, R. T., ed. *Nonlinear Acoustics in Fluids.* Van Nostrand Reinhold Company Inc.: New York, 1984.

Blackstock, D.T. and M. F. Hamilton. *Frontiers Of Nonlinear Acoustics 12th ISNA.* Elsevier Applied Science: New York, 1990.

Coppens, A. B. "Theoretical Study of Finite-Amplitude Traveling Waves in Rigid-Walled Ducts: Behavior for Strengths Precluding Shock Formation." *J. Acoust. Soc. Am.* **49**(1), 1971. p306-318.

Coppens, A. B. and C. Lane. "A Semi-Empirical, Nonlinear Wave Equation for Standing Waves in Cavities." *J. Acoust. Soc. Am.* **54**(1), 1973. p336.

Coppens, A. B. and J. V. Sanders. "Finite-Amplitude Standing Waves in Rigid-Walled Tubes." *J. Acoust. Soc. Am.* **43**(3), 1968. p516 - 529.

Coppens, A. B. and J. V. Sanders. "Finite-Amplitude Standing Waves Within Real Cavities." *J. Acoust. Soc. Am.* **58**(6), 1975. p1133-1140.

Coppens, A. B., et al. "Infinitesimal and Finite-Amplitude Effects in a Real Duct." *J. Acoust. Soc. Am.* **51**(1), 1972. p154.

Denardo, B., et al. "Nonlinear Theory of Localized Standing Waves." *Physical Review Letters.* **69**(4), 1992. p597-599.

Fay, R. D. "Plane Sound Waves of Finite Amplitude." *J. Acoust. Soc. Am.* **3**, 1931. p222-241.

Gaitan, D. F. and A. A. Atchley. "Finite amplitude standing waves in harmonic and anharmonic tubes." *J. Acoust. Soc. Am.* **93**(5), 1993. p2489-2495.

Garfinkel, S. "The Coolest sound." *Technology Review.* October 18, 1994. p17-19.

Husse, M. *Fundamentals of Mechanical Vibrations.* MacMillan Publishing Company: New York, 1983.

144

Kantzios, Y. D. *Nonlinear Forced Standing Waves in a Shallow Channel Near Cut-off Conditions*. M. S. thesis, Mechanical Engineering, Massachusetts Institute of Technology, February 1987.

Kinsler, L. E. *Fundamentals of Acoustics*. John Wiley & Sons: New York, 1982.

Marion, J. B. *Classical Dynamics of Particles and Systems*. Academic Press, Inc.: New York, 1970. p121.

Muir, T. G. *Nonlinear Acoustics*. U. S. Department of Commerce: 1969.

Pierce, A. D. *Acoustics. An Introduction to Its Physical Principles and Applications*. The Acoustical Society of America: New York, 1989.

Rolt, K. D. *A Dissipative Wave Packet Approach For Unified Nonlinear Acoustics*. Ph.D. thesis, Ocean Engineering, Massachusetts Institute of Technology, May 1994.

Seto, W. W. *Theory and Problems of Acoustics*. McGraw-Hill, Inc.: New York, 1971.

Swift, G. "Thermoacoustic Engines and Refrigerators." *Physics Today*. **48**(7), 1995. p22-28.

Temkin, S. *Elements of Acoustics*. John Wiley & Sons: New York, 1981.

Thuras, A. L., et al. "Extraneous Frequencies Generated in Air Carrying Intense Sound Waves." *J. Acoust. Soc. Am.* **6**, 1935. p173-180.

Yam, P. "Cool Sounds." *Scientific American*. November 1992. p120-121.

4538·17

4538·17